Material Science and Technology Division

Heavy Vehicle Propulsion Materials Program
Quarterly Progress Report for
April through June 2006

D. R. Johnson
Technical Project Manager

Prepared for
U.S. Department of Energy
Assistant Secretary for Energy Efficiency and Renewable Energy
Office of FreedomCAR and Vehicle Technologies Program
VT 05 01 020

Prepared by the
OAK RIDGE NATIONAL LABORATORY
Oak Ridge, Tennessee 37831-6066
Managed by
UT-Battelle, LLC
for the Department of Energy
Under contract DE-AC05-00OR22725

CONTENTS

Materials for Advanced Fuel Systems

Mechanical Reliability of Piezo Stack Actuators for Fuel Injectors (ORNL)

Materials for Exhaust Aftertreatment

Advanced Diesel Aftertreatment Program (Caterpillar Inc.)

Ultra-High Resolution Electron Microscopy for Characterization of Catalyst Microstructures and De-activation Mechanisms (ORNL)

Development of NO_x Sensors for Heavy Vehicle Applications (ORNL and Ford Motor Company)

Development of Materials Analysis Tools for Studying NO_x Adsorber Catalysts (ORNL and Cummins Engine Company)

Catalysis by First Principles (ORNL)

Durability And Reliability of Ceramic Substrates for Diesel Particulate Filters (ORNL)

Materials for Air Handling and Thermal Management

Advanced Cast Austenitic Stainless Steels for High Temperature Components (ORNL and Caterpillar Inc.)

Friction and Wear Reduction in Diesel Engine Valve Trains (ORNL)

Materials for Structural Components

Advanced Machining and Sensor Concepts (University of Michigan)

Synergistic Process-Enhanced Grinding of Advanced Engine Materials (ORNL)

Materials for Hot Section Components

NDE Development for Ceramic Valves for Diesel Engines (Argonne National Laboratory)

Life Prediction of Diesel Engine Components (ORNL and Caterpillar)

Lightweight Valve Train Materials (Caterpillar Inc.)

An Integrated Surface Modification of Engineering Materials for Heavy Vehicle Applications (NIST)

Characterization of Physical and Mechanical Properties

Coating Evaluation and Performance (ORNL)

Mechanical Reliability of Thermoelectrics (ORNL)

Emerging Technologies

Processing and Characterization of Structural and Functional Materials for Heavy Vehicle Applications (North Carolina A&T State University)

Powder Processing of Nanostructured Alloys Produced by Machining (Purdue University)

Next Generation Ceramics for Heavy Vehicle Propulsion Applications (ORNL)

Mechanical Reliability of PZT Piezo-Stack Actuators for Fuel Injectors

A. A. Wereszczak and H. Wang
Ceramic Science and Technology (CerSAT)
Oak Ridge National Laboratory

Objective/Scope

The use of piezoelectric stack actuators as diesel fuel injectors has the potential to reduce injector response time, provide greater precision and control of the fuel injection event, and lessen energy consumption (e.g., for use in homogeneous charge compression ignition, HCCI, engines). Though piezoelectric function is the obvious primary function of lead zirconate titanate (PZT) ceramic stacks for fuel injectors, their mechanical reliability can be a performance and life limiter because PZT is both brittle, lacks high strength, and may exhibit fatigue (i.e., slow crack growth) susceptibility. That brittleness and relatively low strength can be overcome with proper design though. This project combines in-situ micromechanical testing, microstructural-scale finite element analysis, probabilistic design sensitivity, and structural ceramic probabilistic life prediction methods to systematically characterize and optimally design PZT piezoelectric stack actuators that will enable maximized performance and operational lifetime.

Technical Highlights

To initiate the study of the translation of piezoceramic strength and probabilistic life prediction and design of piezoactuators, industry type 5A4E and 5H4E piezoceramic sheets were sectioned into square specimens and flexure tested in ball-on-ring testing. The manufacturer's reported d33 for the 5A4E and 5H4E dielectrics were 390 x 10^{-12} m/V and 650 x 10^{-12} m/V, respectively while their reported Curie temperatures were 350 and 230°C, respectively.

The strength test setup (see Fig. 1) consists of a micromechanical test frame that has integrated load and acoustic emission measuring capabilities. Load and acoustic histories for a test are shown in Fig. 2. Interestingly, the specimens do not always fracture catastrophically and Fig. 2 can illustrate that. The first acoustic event (occurring at the ~ 90s mark) is associated with crack initiation and that corresponding load was used to calculate strength after Shetty, *et al.* [1]. That fracture does immediately run through the whole specimen causing the specimen to withstand additional loading. The second event is undergoing further interpretation and the third event is associated with complete specimen fracture.

The 5A4E PZT dielectric had a higher strength than the 5H4E as illustrated in Figs. 3-4. The Weibull moduli of both materials were statistically equivalent. Preliminary optical fractography showed failure initiation was at the surface indicating that a surface-type flaw or volume-type flaw located at the surface was its cause.

The calculated strength is undergoing scrutiny through comparisons of stresses predicted from finite element analysis (Fig. 5). Based on the former, it appears that Ref. [1] may be overestimating the stresses. Efforts are underway to determine effective areas and volumes for the test configurations studied here - they will enable strength-size-scaling.

Hardware (amplifier, loading platens, capacitance gages, data acquisition system, etc.) was acquired in preparation for piezostack testing that will enable concurrent mechanical loading and piezoactuation.

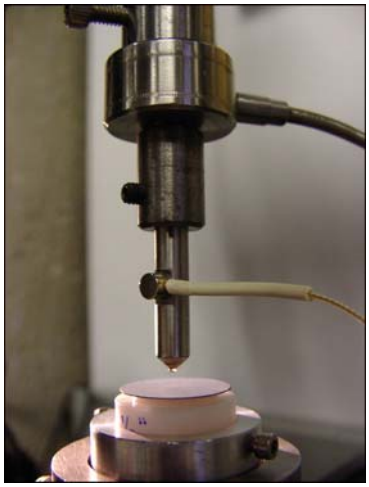

Figure 1. Micromechanical ball-on-ring biaxial flexure strength test setup. Load and acoustic activity are continuously measured during each test. A thin disk specimen is shown.

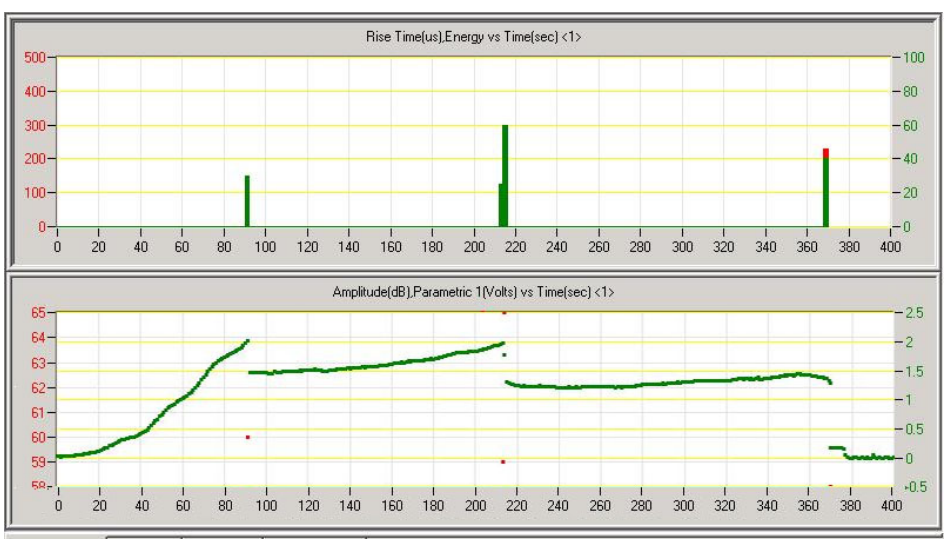

Figure 2. The upper graph shows acoustic signal rise time as a function of time and the lower is a double-Y graph that shows acoustic events (red dots) and load in Newtons as a function of time. The first event is associated with crack initiation and the corresponding load is used to calculate strength.

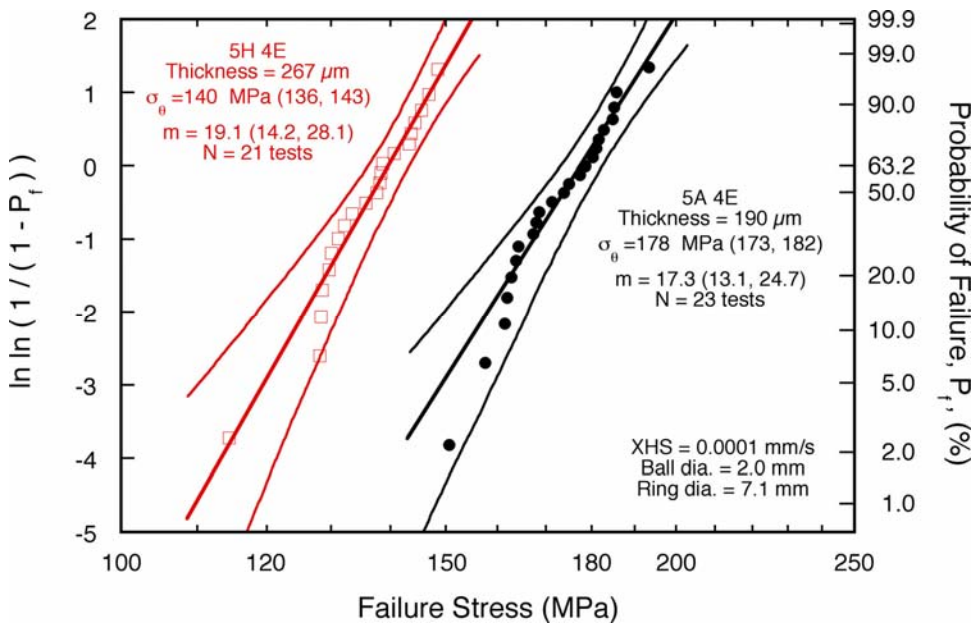

Figure 3. Weibull strength distributions for the 5H4E and 5A4E piezoceramics. The same loading fixture was used to test both materials. The 5H4E specimens were approximately 50% thicker than the 5A4E.

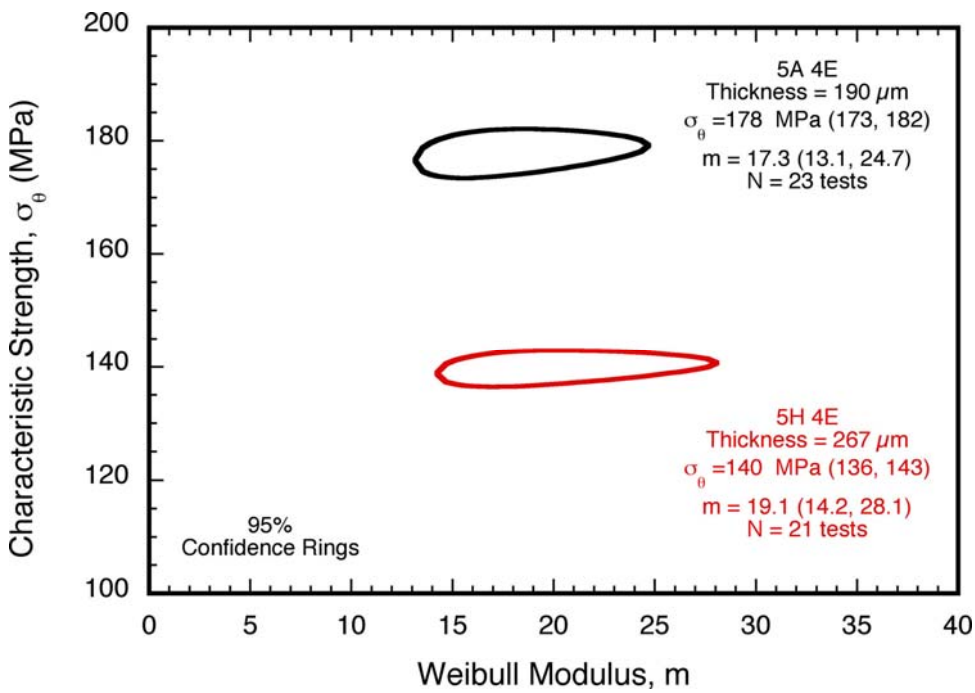

Figure 4. 95% confidence ratio rings for characteristic strength and Weibull modulus

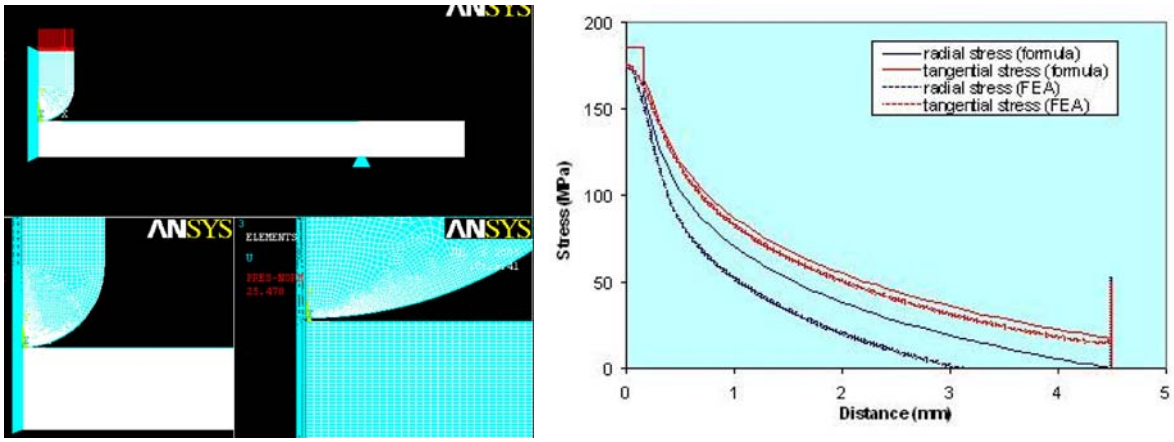

Figure 5. Axisymmetric finite element model (left) ball-on-ring configuration and comparison (right) of the predicted radial and tangential stresses as a function of radial position from FEA with those from [1]. The FEA predicted stresses are lower.

Status of FY 2006 Milestones

Create and develop a general finite element model that predicts operational stresses in a PZT piezostack actuator and that enables probabilistic life prediction estimation. [09/06]
Completed.

Communications/Visits/Travel

Discussions occurred with E Baker of Connecticut Reserve Technologies that involved the potential enhancement of CARES/Life to accommodate piezo-type elements in ANSYS.

Publications

[1] D. K. Shetty, A. R. Rosenfield, P. McGuire, G. K. Bansal, and W. H. Duckworth, "Biaxial Flexure Tests for Ceramics," *Ceramic Bulletin*, 59:1193-97 (1980).

References

None.

Advanced Diesel Aftertreatment Program

Corey Shannon, Herbert DaCosta, Matt Stefanick, Ron Silver and Craig Habeger
Advanced Materials Technology, Caterpillar Inc.

Objective/Scope

The objective of the effort is to develop and evaluate materials that will be utilized in aftertreatment systems for diesel engine applications. These materials include catalysts for CO and hydrocarbon oxidation, NO_x reduction, and filtration media to improve particulate abatement capabilities in the exhaust system. The project is a part of Caterpillar strategy to meet EPA requirements for regulated diesel emissions in 2007 and beyond.

This year's focus is to assess durability of various catalyst technologies in terms of phosphorous, sulfur and thermal degradation, and to identify diesel particulate trapping materials that have high durability and filtration efficiency to comply with future emission regulations for heavy-duty diesel engines.

Technical Highlights

Diesel Particulate Filter (DPF)

Many projects have been executed to improve the performance and efficiency of the diesel fuel burner on which the 1-inch diameter DPF cores are tested. One such project was the 6-sigma "lean" event. A team composed of primary users and customers of the test bench examined the entire process of loading particulate matter onto a DPF. This team was able to suggest changes to the procedure as well as physical changes on the bench itself. Many safety issues were also resolved. Another 6 sigma-like project was carried out and determined the reproducibility of the measurements acquired from the fuel burner bench. This project ascertained that the filtration efficiency of a DPF can be measured with less than 2% error.

A phosphorus deactivation study on catalyzed cordierite and the catalyzed alternative DPF is in progress. The catalyzed alternative DPFs were loaded with phosphates for 200 minutes. Thus far, the study has shown that when the DPF is loaded with phosphate, the time it takes for 50% of the soot to lightoff increases (Figure 1). As the study continues, we will look at how even more phosphorus aging affects the lightoff curve on the alternative DPF. We will also compare this to catalyzed cordierite.

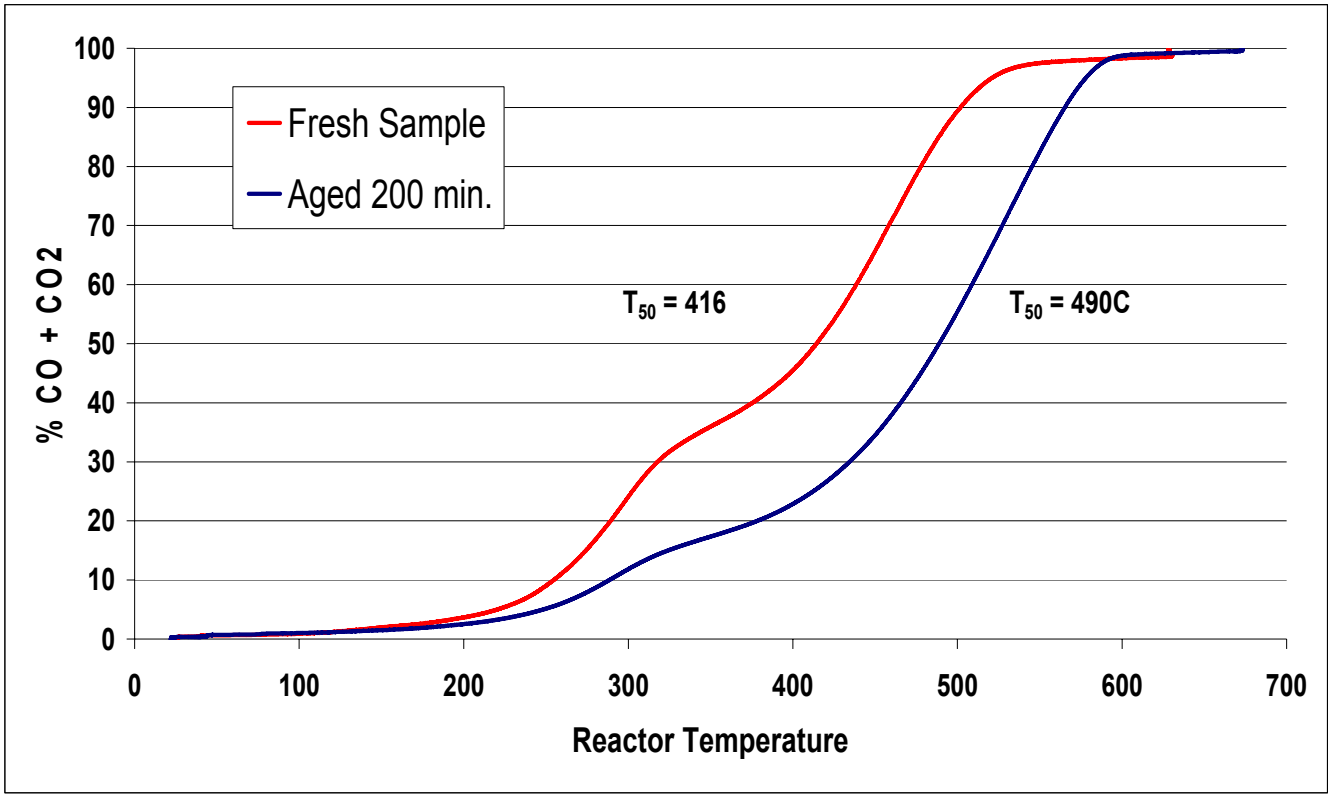

Figure 1. Percent carbon monoxide and carbon dioxide produced by lightoff versus reactor temperature before and after phosphorus aging.

Catalyst Durability

Urea- SCR:

Figure 2 shows the relative activity (aged conversion/ degreened conversion) of zeolite based urea SCR NO_x reduction catalyst after exposure to phosphorus (P) and sulfur (S). Catalysts that were exposed to 5 g /liter P and S at 210°C showed a slight degradation in NO_x conversion relative to the degreened activity. Increasing the exposure level at that temperature to a total of 10 g /liter P and S resulted in an initial apparent loss of 70% of the degreened activity at 300°C. A repeat of the activity test showed a significant recovery in NO_x conversion, such that the activity loss at 300°C was just 20%. For comparison, this amount of activity was lost from exposure to 10 g/liter P only. Activity testing was performed in the absence of S and P, so it appears that exposing the catalyst to sulfur-free gas removes most of the sulfur that was responsible for the initial activity loss. The resulting "cleaned" catalyst performs similar to a sample that was just exposed to 10 g/liter P. The cleaning effect can even be observed during the first activity test, where there is significant recovery in activity as the sample is ramped up in temperature. The aging is being repeated by exposing the catalyst to P and S at a higher temperature in order to see if the effect of the sulfur free gas is a result of the relatively low exposure temperature.

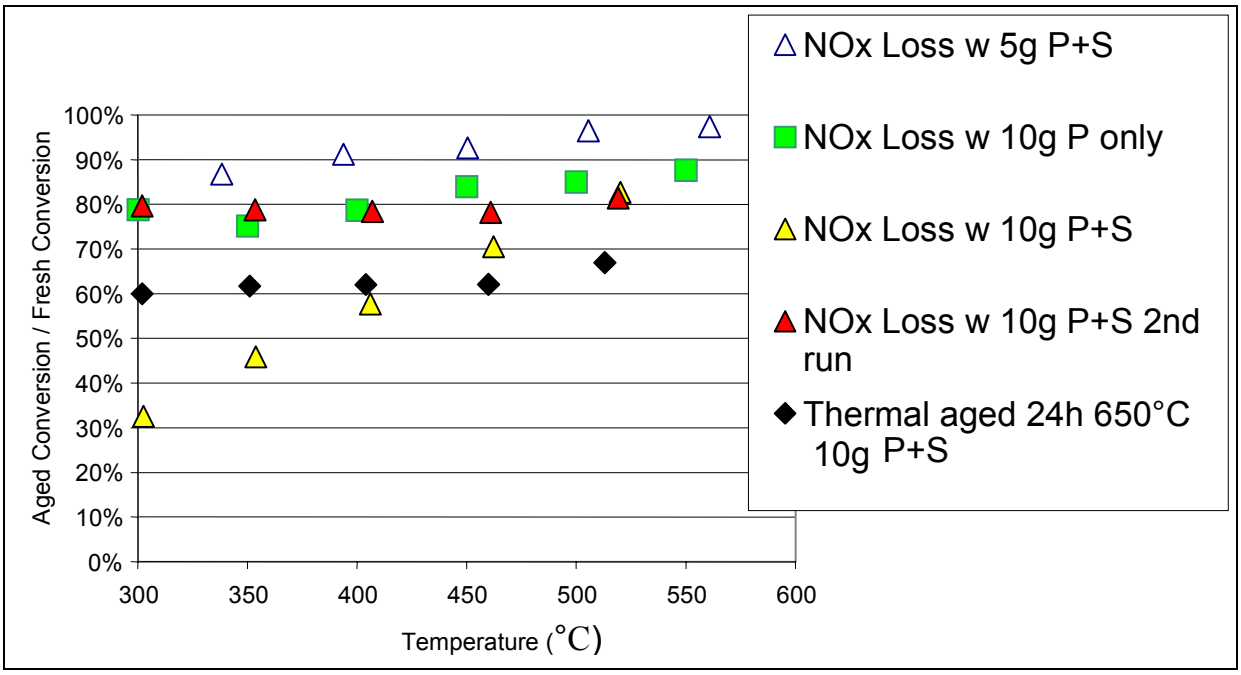

Figure 2. Relative NO_x performance of SCR catalysts after exposure to phosphorus plus sulfur and after exposure to phosphorus only.

Figure 3 shows similar relative performance results for ammonia conversion. Typically NH_3 is converted either by reacting with NO_x or with O_2 under SCR reaction conditions. Just as with NO_x in Figure 2, the initial NH_3 conversion drops significantly when the P and S exposure level is increased from 5 g/liter to 10 g/liter. In this case, sweeping the catalyst with sulfur free gas recovers 90% of the initial activity, or results in a loss of just 10% of degreened NH_3 conversion. The recovered activity also corresponds to the effect of a P-only exposure of 10 g/liter.

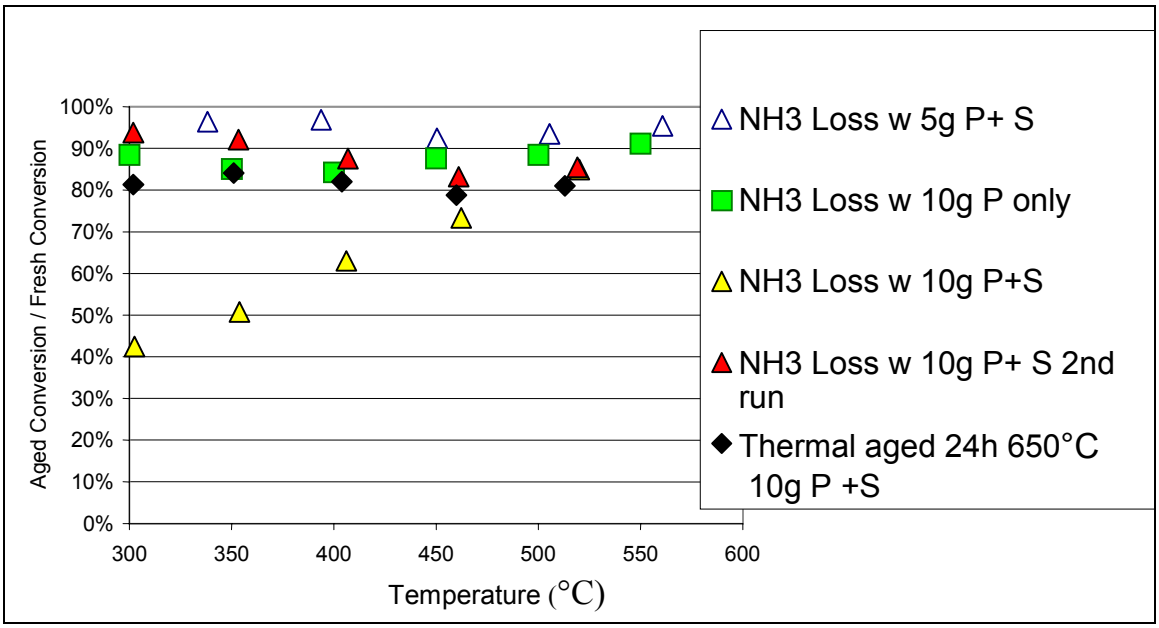

Figure 3. Relative NO_x performance of SCR catalysts after exposure to phosphorus plus sulfur and after exposure to phosphorus only.

The 10 g/ liter P and S exposed catalyst was then thermally aged at 650°C for 24 hours in a mixture of 10% steam and air. The resulting loss of NO_x conversion, shown in Figure 2, was about 40% of the degreened performance or about the same effect as that of the P and S exposure. This loss of activity did not appear to be recoverable by exposing the sample to sulfur free gas. The effect of the thermal aging on NH_3 conversion (shown in Figure 3) is less dramatic, resulting in a total decline of just 20% of degreened activity. This level is not much different than the effect of P and S exposure alone. The difference in temperature effect may be due to sintering of the active metal (e.g. iron or copper) due to the hydrothermal aging. The active metal seems to play an important role in activating the NO_x, but may not be as critical in converting NH_3. A test where the zeolite SCR is only thermally aged will be run to identify the impact of having P and S on the catalyst during thermal aging.

The relative NOx performance loss appears to be slightly higher than the NH_3 conversion loss for a given P and S exposure. This may indicate that the catalyst oxidation of NO to NO_2 is more susceptible to activity loss due to thermal aging, P and S exposure, than is the main SCR reaction which converts equal moles of both NH_3 and NOx.

Future Plans

1. Exposure of zeolite SCR catalyst to the P plus S combination at higher temperature to determine the importance of exposure temperature in overall activity loss, followed by thermal aging of uncontaminated zeolite samples to determine the effect of interaction between temperature and contaminant.
2. Continue searching for and testing new substrate materials for DPF filters.
3. Load samples of catalyzed DPFs with varying levels of P to see how lightoff temperature is affected on both catalyzed and uncatalyzed samples.
4. Modify the aging pulsator to allow direct introduction of oil in order to simulate catalyst exposure to uncombusted phosphorus.

Travel

Ron Silver traveled to Detroit in April to attend the SAE Congress and discuss catalyst durability issues with other experts in the field.

Presentations/Publications

Paper submitted for presentation to the 2006 DEER conference. Abstract submitted to SAE for 2007 Congress.

Status of FY 2006 Milestones

1. Tested thermally aged 1-in. x 3-in. core samples un-catalyzed and catalyzed DPF for soot regeneration. Follow up will include P exposure.
2. Urea-SCR catalyst have been aged with P and S, additional testing is scheduled to explore issues raised with current results.

Ultra-High Resolution Electron Microscopy for Characterization of Catalyst Microstructures and De-activation Mechanisms

L.F. Allard, D.A. Blom, C.K. Narula, M. A. O'Keefe, M. J. Yacaman and S. A. Bradley

Objective/Scope

The objective of the research is to characterize the microstructures of catalyst materials of interest for the treatment of NO_x emissions in diesel and lean-burn gasoline engine exhaust systems. The research heavily utilizes new capabilities and techniques for ultra-high resolution transmission electron microscopy with the HTML's aberration-corrected electron microscope. The research is focused on understanding the effects of reaction conditions on the changes in morphology of heavy metal species on "real" catalyst support materials (typically oxides), and the understanding of the structures of model mono-, bi- and multi-metallic catalyst systems of known particle composition. With the former systems, these changes are being studied utilizing samples treated in both steady-state bench reactors and a special *ex-situ* catalyst reactor system especially constructed to allow appropriate control of the reaction. Model samples of nanoparticulates of controlled composition on carbon or oxide supports are also being studied in collaboration with the catalysis group at the University of Texas-Austin (Prof. M. Jose-Yacaman and students). Studies of the behavior of Pt species on oxide substrates are also being conducted with colleague S. A. Bradley of UOP Co.

Technical Progress

Although the preparation and properties of heterogeneous catalysts have been studied for decades, it is not well understood how fine dispersions of heavy metal species in "as-prepared" catalysts are arranged on common supports such as γ-alumina, amorphous silica, or titania (anatase or rutile). Aging or calcining treatments typically cause atomic level dispersions to coalesce into discrete particles of sizes >2 nm, which have crystal lattices that can be imaged using conventional high-resolution bright field imaging techniques. However, the most useful technique for studying catalysts that have heavy metal species dispersed at the individual atom or fine metal cluster level is with high-angle annular dark field (HA-ADF), or "Z-contrast", imaging in an aberration-corrected scanning transmission electron microscope (STEM). Modern STEM or STEM/TEM instruments, such as ORNL's ACEM, that permit ADF images to be recorded with sub-Ångström resolution allow single atoms, clusters of a few atoms, and "rafts" of atoms which are pre-cursors to discrete crystalline particles to be accurately characterized. The present study involves sub-Ångström imaging to characterize catalysts comprising Pt on oxide substrates which have different metal-support interactions. To study the effect of the supports on metal cluster behavior, catalysts were prepared by impregnating the support materials with 0.35 wt % Pt, and oxidizing the material at 525ºC. The Pt on γ-Al2O3 was then reduced at 500ºC in H2. Goals of the investigation were to determine the number of atoms in a cluster and the structure of the cluster (or raft), investigate metal-support interactions, and by using ORNL's *ex-situ* catalyst reactor, to understand the formation of metal clusters as a result of reduction of the oxidized catalyst.

For the oxidized Pt on γ-Al2O3 catalyst, individual Pt atoms were observed randomly decorating the catalyst support. Detailed examination revealed that these were either individual Pt atoms or

"dimers" of Pt atoms (Fig. 1). Occasionally a small cluster of Pt atoms was observed. A Fourier-filtered and transformed image suggested that the Pt atoms are between the Al atom rows. This is consistent with observations by Nellist and Pennycook [2], who showed for ultradispersed Pt on alumina that Pt atoms were constrained to match the surface structure. The H2-reduced and air-exposed Pt on γ-Al2O3 catalyst consisted of both 1 to 1.5nm clusters and individual Pt atoms (Fig. 2). It is probable that the individual Pt atoms will join a metal cluster with longer time or higher temperature of reduction. The left half of Fig. 2 is the initial image in a time series of the same area, while the right half is the fifth image in the series. The individual atoms have moved on the catalyst support and the specific cause of this disordering is not known [3]. The cluster had a flat or layer-like appearance, but it is not clear whether this is a result of any interaction with the electron beam. In addition the location of the cluster relative to the support is unchanged, but the atomic arrangement in the cluster has changed from the first to fifth image. More work is required to resolve this issue. About 12 to 20 Pt atoms are present in these clusters.

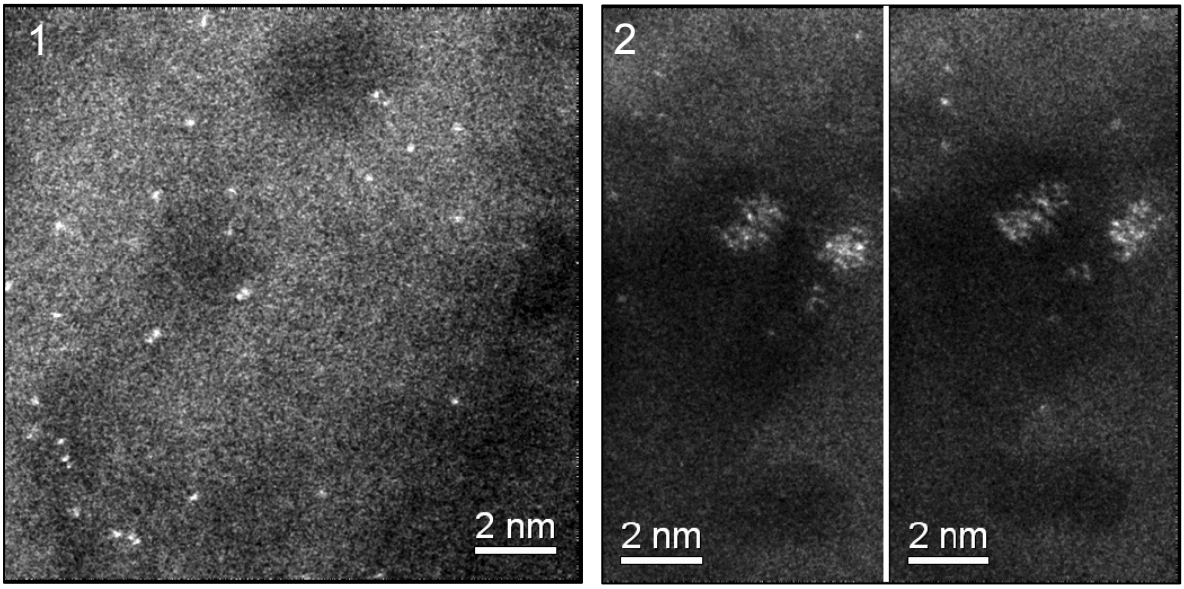

Fig. 1 Oxidized Pt species shows ultra-fine dispersion on g-alumina, with single atom and "dimers" as primary features.
Fig. 2 After reduction, clusters or "rafts" of Pt atoms formed. Time sequence ADF images showed no particular tendencies for the rafts to agglomerated under the beam into larger entities.

Since Pt on SiO_2 has a tendency to readily agglomerate, the catalyst was examined only in the oxidized condition. Figure 3 shows typical clusters, which were found to range in size from less than 1 nm (10 atoms) to a little more than 2 nm (25 atoms), and had a raft morphology with some areas comprising layers of 2 or 3 atoms. These rafts were considerably more mobile on the catalyst support. In many instances some clusters would merge between fields of view, as seen in the image time sequence in Fig. 3. A background-subtracted perspective view, Fig. 4, suggests the rafts in Fig. 3 are no more than 2 atoms high.

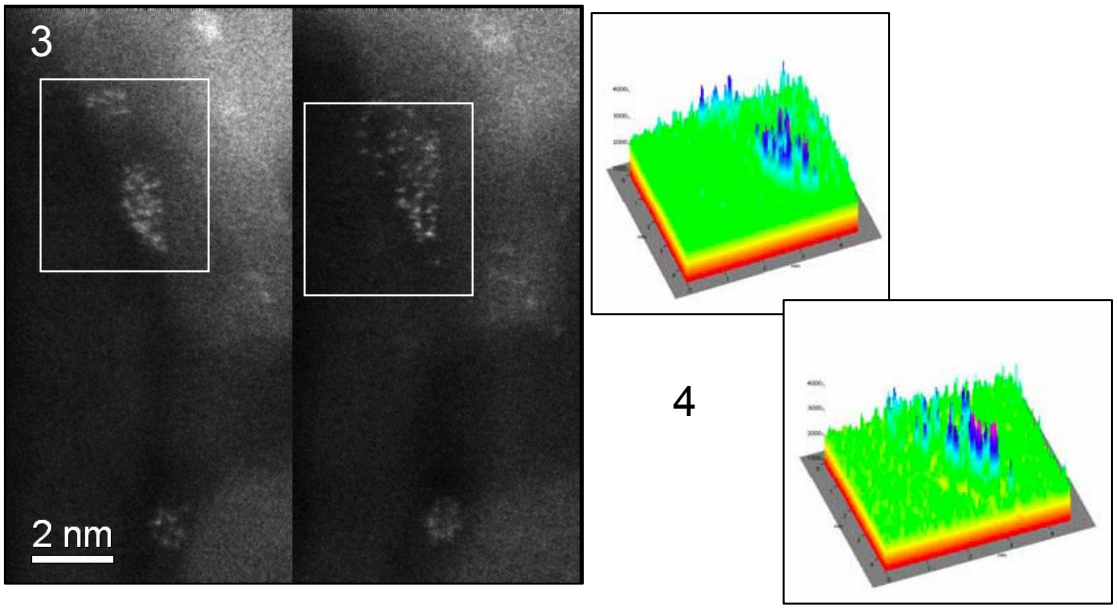

Fig. 3 Pt on SiO2 in the oxidized condition tended to form distinct rafts of atoms primarily comprising single to two-atom thick layers, as shown in the perspective views of Fig. 4. Rafts showed significant mobility under the electron beam in time sequence ADF images, and adjacent rafts would commonly agglomerate into larger entities.

The tendency for atoms, clusters and rafts to be more mobile on amorphous silica versus crystalline g-alumina under the electron beam suggests the probability of similar behavior during reaction treatments at elevated temperatures. Experiments comparing the same sample area before and after reduction treatments in the ex-situ reactor are being conducted, and results will be detailed in the annual report. This will provide confirming evidence for the conclusions regarding the relative atom species mobility on the various substrates.

Pt on TiO_2 should have the highest specimen-support interaction, and therefore the lowest tendency for mobility of Pt species. Figure 5 shows reduced Pt species on TiO_2 (rutile), with rafts on the order of 1nm observed, but still a significant population of single atoms and dimers. This image fortuitously was oriented to allow imaging of the underlying rutile lattice, showing the tendency for the Pt rafts to orient with the lattice. Figure 5b shows the area of 5a after additional beam exposure. Some rearrangement of the individual rafts is seen, as with the Pt on alumina, but in general the rafts are not particularly mobile on the surface. One raft is noted by the square in Fig. 5b, shown at higher magnification in Fig. 5c. This shows strong bright contrast of a trimer of atoms, consistent with the structure (for part of the raft) suggested in the cartoon of Fig. 5c. The ability to characterize such structures at the atomic level with the sub-Ångström imaging capability of the ACEM is of critical importance for full understanding of the behavior of catalyst materials.

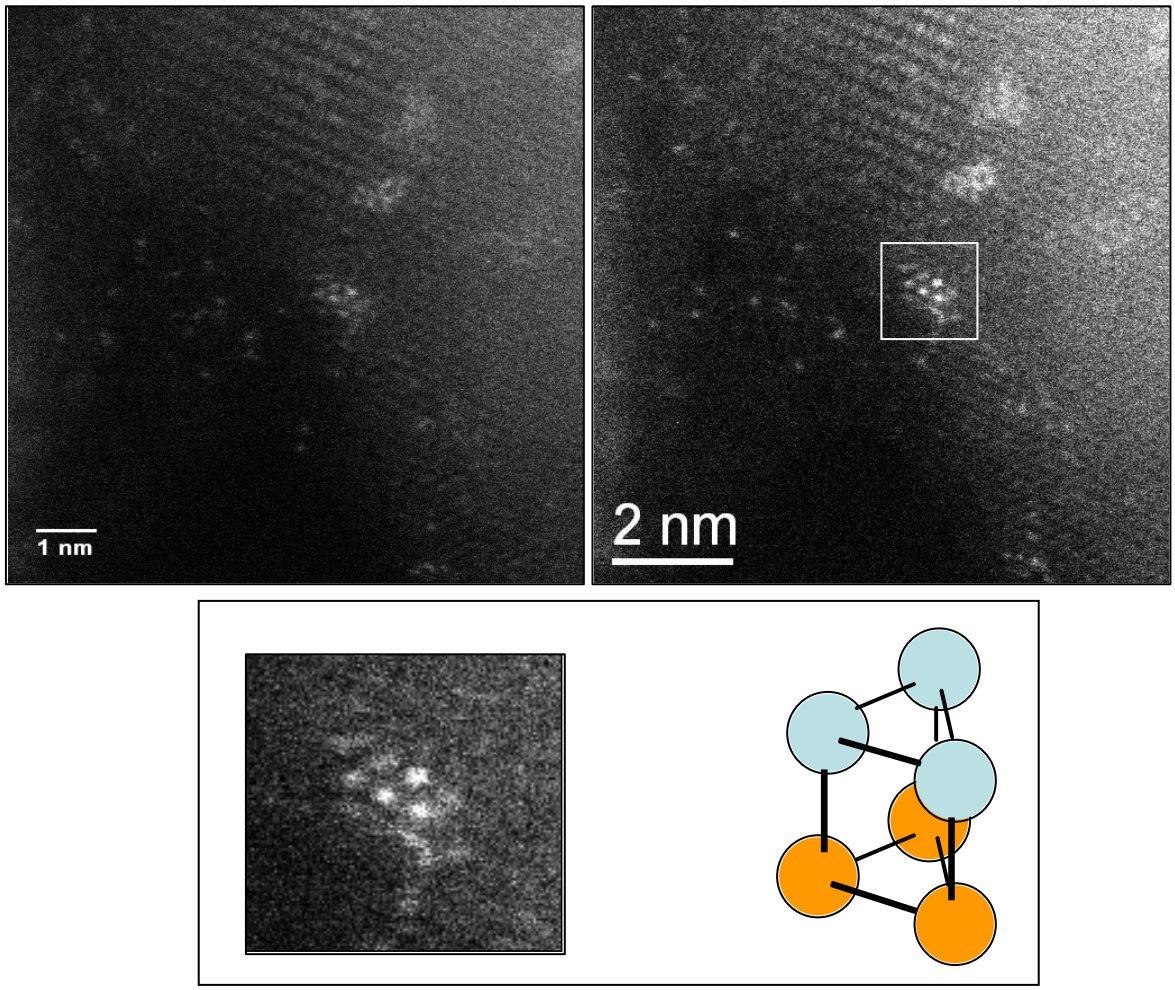

Fig. 5 a) Pt on rutile (TiO2), in reduced state. Rafts 1 nm in size, and some individual Pt atoms are present. b) same area, after additional exposure to electron beam. The cluster highlighted is shown at higher magnification in c). The cartoon suggests a structure of atoms in part of the raft.

Status of Milestones

On schedule

Communications/Visits/Travel

None this period

Publications

1. "Observation of Pt Atoms, Clusters and Rafts on Oxide Supports, by Sub-Ångström Z-Contrast Imaging in an Aberration-Corrected STEM/TEM,"
D. A. Blom, S. A. Bradley, W. Sinkler and L. F. Allard, *Microscopy and Microanalysis (Supp 2) 2006*, Cambridge University Press, p. 50.

2. "Early Results from an Aberration-Corrected JEOL 2200FS STEM/TEM at Oak Ridge National Laboratory," D. A. Blom, L. F. Allard, S. Mishina, and M. A. O'Keefe, Microsc. and Microanal. in press, 2006.

Development of NO_x Sensors for Heavy Vehicle Applications

David L. West, Fred C. Montgomery and Timothy R. Armstrong,
Oak Ridge National Laboratory

CRADA No. ORNL 01-0627
with Ford Motor Company

Objective

This project seeks to develop technologies and materials that will facilitate the development of a NO_x sensor. The development of low-cost, simple NO_x sensors is key to the development of ultra-low NO_x emission engines, directly supporting the OHVT goals.

Technical Highlights

The technical direction of most work in the 3rd quarter was dictated by the CRADA partner's (Ford) request to increase electrode electrical impedance and adhesion. In order to achieve these composite (multi-phase) electrodes were formulated, blended, and tested. Two different formulations were examined: Conductive oxide (chromite) + electrolyte (zirconia) and conductive oxide + electrolyte + insulator (alumina).

The 2-phase formulation was ineffective with regard to increasing the electrode impedance but the 3-phase formulation did lead to an increase in impedance as shown in Fig. 1. It can be seen there that the composite formulation yielded an approximately 3-fold increase in electrical resistance while maintaining the response time and magnitude observed with the single-phase electrode formulation.

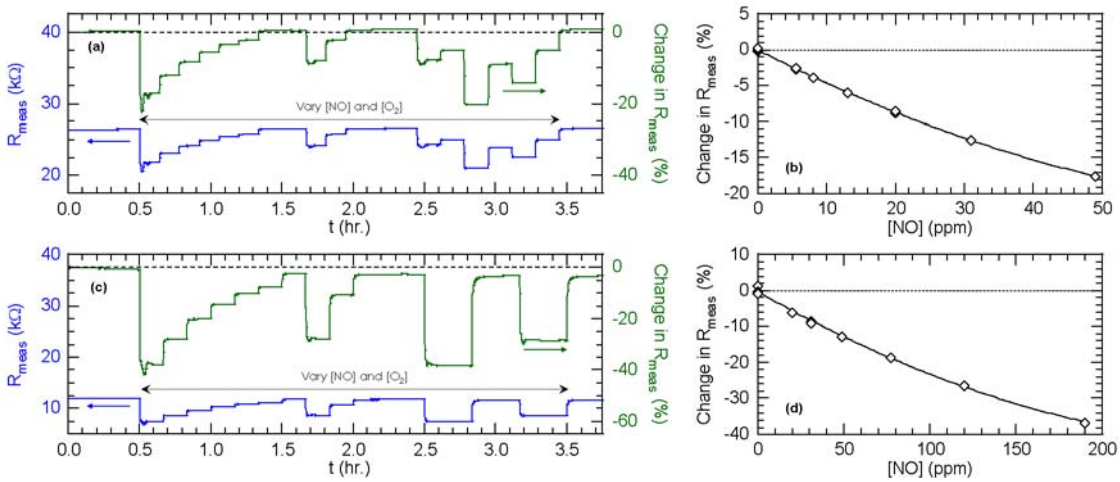

Figure 1: Response of elements with composite (a, b) and single-phase (c, d) electrodes to varying [NO] and $[O_2]$. The maximum [NO] concentrations employed were 49 and 190 ppm for (a) and (b), respectively. Operating temperature = 600°C, $[O_2]$ varied between 7 and 20 vol %.

The impact of the composite formulation on cross-sensitivity is shown in Fig. 2. Use of the composite formulation has led to increased sensitivity to hydrocarbons and appeared to have little effect on the cross-sensitivities to varying [O_2] and [H_2O]. Since in the final sensor design it is envisioned to employ an oxidation catalyst operating at ~700°C the increased cross-sensitivity to hydrocarbons is not considered a major concern.

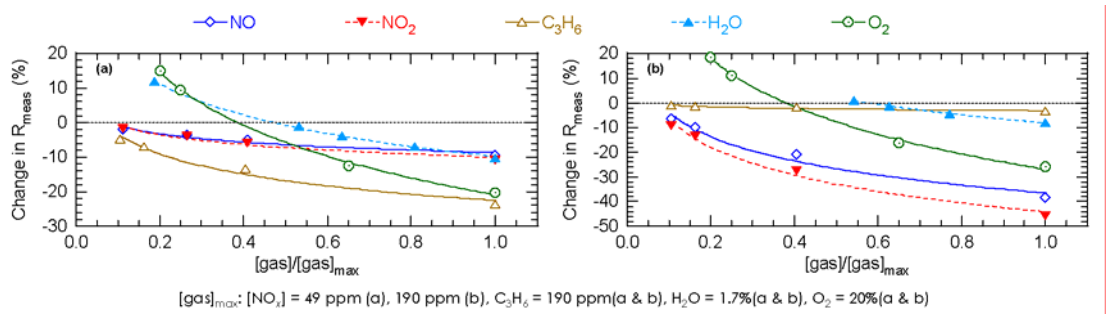

Figure 2: Cross-sensitivity of elements with composite (a) and single-phase (b) electrodes. Data for gases other than O_2 collected with 7 vol % O_2 and for gases other than H_2O collected with 1 vol % H_2O.

Future Plans

- Furnish sensing elements with composite electrodes to Ford for dyno testing.
- Work with Ford to develop a means of characterizing electrode adhesion.
- Investigate new electrical biasing scheme with electronics designed and built in-house at Ford.

Status of FY2006 milestones

(1) Detailed understanding of sensing mechanism. **(09/06)**
This is a collaborative effort with Northwestern University. During the 3rd quarter electrode geometries suitable for theoretical studies were developed at ORNL and furnished to Ford for manufacture and shipment to Northwestern.

On track.

(2) Evaluate cross-sensitivities, including H_2O from 1 to 10 vol %. **(06/06)**
Relevant cross-sensitivities have been evaluated, save that for the higher H_2O concentrations. Testing at higher [H_2O] will require capital outlays that are inconsistent with current budgetary levels, and higher [H_2O] can be obtained in testing at Ford.

Partially completed / on hold.

(3) Evaluate stability in real exhausts. **(06/06)**
ORNL is ready to supply prototype elements to Ford for dyno testing.

On track.

(4) Investigate use of time-varying electrical stimulus (e.g., square wave variation). **(09/06)**
Interest in this has been re-expressed by Ford and we are currently awaiting shipment of electronics for studies to be done at ORNL.

On track w/ delayed delivery date.

Communications/Visits/Travel

- Biweekly teleconferences were held with LLNL and Ford during the quarter.

Problems Encountered

- None

Publications

- None

Intellectual Property Filed

- None

Development of Materials Analysis Tools for Studying NO_x Adsorber Catalysts

Thomas Watkins, Larry Allard, Doug Blom, Michael Lance, Harry Meyer, Larry Walker and Chaitanya Narula
Oak Ridge National Laboratory

Cheryl Klepser, Tom Yonushonis, Howard Fang and Roger England
Cummins Inc.

Objective

The objective of this effort is to produce a quantitative understanding of the processing and in-service effects on NOx adsorber catalyst technology leading to an exhaust aftertreatment system with improved catalyst performance capable of meeting the 2007 Environmental Protection Agency (EPA) emission requirements in the United States.

Samples and Approach

A Cummins catalyst supplier provided new catalyst materials, which are being examined with diagnostic tools developed under the CRADA. Investigations of these candidate-production materials are being implemented on both the bench and engine research scale. These investigations include the examination of unused, reactor and engine-aged catalyst samples. Investigative tools included transmission electron microscopy (TEM), X-ray diffraction (XRD), X-ray photoelectron spectroscopy (XPS), Raman Spectroscopy and infrared spectroscopy (IR).

Technical Highlight

The last report described the characterization of a new/never-been-used diesel oxidation catalyst (DOC). Here, the same DOC has been aged in a retort oven at 700°C for 24 hours, with 10% water added, and new cores were extracted. The samples were examined with XPS, XRD and TEM.

New and aged samples were examined for compositional variations along the length of a single trough using XPS. The average surface compositions are shown in Table I. Single-trough samples were prepared by sectioning an 8-10 trough layer from the interior of the received honeycomb core. Equidistant positions along 2 separate troughs were defined; two sets of data were taken within each trough (15 points/trough), analyzed and averaged. For the new sample, a third trough was examined 5 months after the first two, confirming the reproducibility of the data (i.e., no significant change with time). The compositional variation along the troughs is demonstrated in Figures 1 and 2 for the new and aged DOC's, respectively. Each shows two graphs, one for the major elements (O, Al, Si, and C) and one for the minor elements (N, Pt, and F) identified. Presently, the origin of F is unknown. The figures show a small decrease in the amount of O within in the probe depth and a slight increase in the amounts of Pt, Al and C in the aged relative to the new DOC. The amount of Si seems unchanged, and the variability of N and F is inconclusive. Examination of the individual runs (not shown), made prior to adding/averaging, show the O, C, and Al data were more scattered, which could be due to the atmospheric contamination for O and C. The origin of the changes in Al is unclear, as absence of magnesium indicates that the signal originates from the washcoat only. The washcoat likely contains some sort of alumino-silicate, based on the majority elements. In contrast, the Pt scans

were more consistent, trough-to-trough and run-to-run. Based on this, two major conclusions can be drawn from these data. First, the aging process does not influence the nominal composition of the *major* elements or change the uniform distribution along the trough. Second, the Pt signal is nearly doubled for the aged sample and implies that Pt atoms have migrated/redistributed to the near surface region (~5-10 nm, i.e., the probe depth for XPS).

In Figure 3, XRD indicates that the sample contains orthorhombic cordierite ($2MgO•5SiO_2•2Al_2O_3$) and platinum. The broad peak at low angle at ~20° 2Θ is due to an amorphous phase, possibly part of the washcoat. Previously, γ-alumina was tentatively identified within the washcoat of the new DOC. Figure 4 compares the XRD patterns of the new/unused and aged DOC samples showing the marked crystallite size growth of the Pt (<1, i.e., not observable, to ~30 nm).

TEM was performed on both the new and aged samples. In the new sample, a majority of the washcoat/support is found to be amorphous (see above), and energy dispersive spectroscopy indicates the presence of Si, Al and O (perhaps alumina and silica). The washcoat contains Pt metal crystals, which are 1 - 4 nm in size (see Figure 5). Many of the Pt is atomically dispersed as seen with Aberration-corrected STEM. This is the first time such a non-ideal sample has been examined in this fashion. Small clusters of Pt (1-3 atoms thick) are also observed. For thicker areas, the more limited depth of field in aberration-corrected STEM provides richer, 3D data to be extracted by using a focusing/defocusing technique over ~5nm. Again, this is the first time that this has been applied to large cluster. The *aged* sample demonstrated evidence of massive Pt sintering (see Figure 6), which is consistent with the XRD results above. Small nanocrystals, atomic clusters, and single atoms are also still present (see Figure 7). In Figure 8, the moderately sized nanocrystals are surrounded by "cloud" of Pt clusters, which suggests a redispersion of Pt. The mechanism is presently unknown but the electron beam has been eliminated as a potential cause due to lack of change with time under the electron beam. The Pt atoms are observed to preferentially attach to alumina planes in the support.

Table I- Surface composition (atom %) of new and aged DOC samples averaged from data taken along the length of a single trough using XPS.

Average Composition per Trough

New

	O	Al	Si	C	N	F	Pt
T-1+2	58.5	25.1	11.0	4.6	0.33	0.34	**0.13**
T-3	61.4	24.6	10.4	2.6	0.60	0.25	**0.12**

Aged

	O	Al	Si	C	N	F	Pt
T-1	56.4	28.4	11.2	3.2	0.40	0.22	**0.20**
T-2	56.8	26.2	10.3	5.5	0.62	0.43	**0.23**

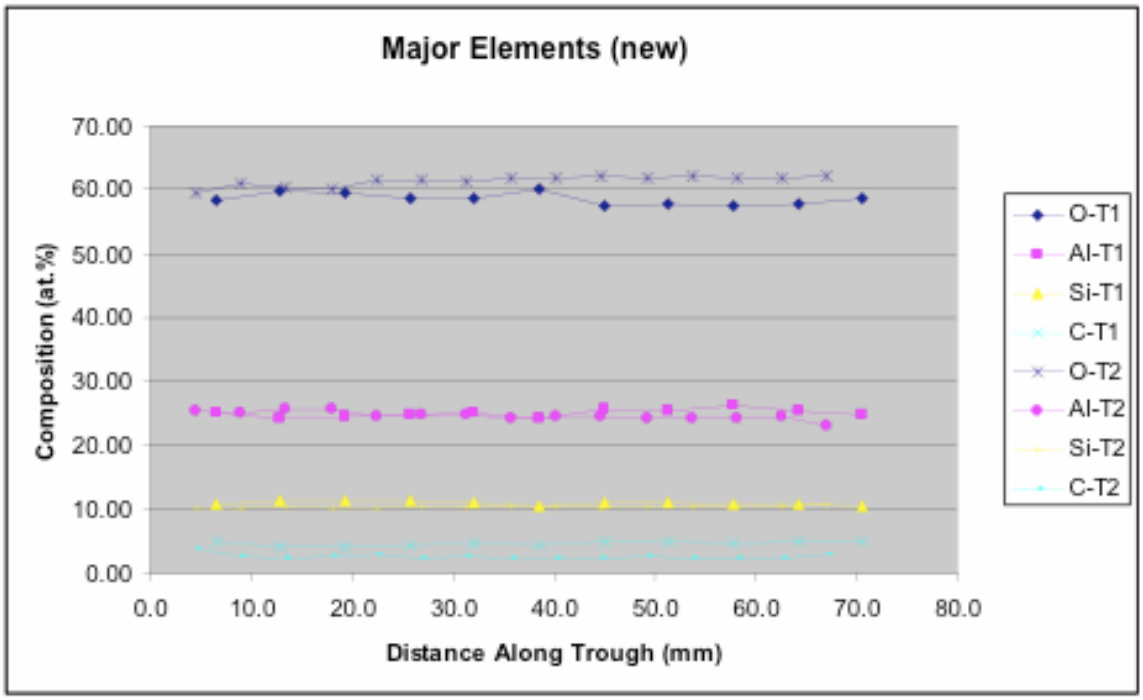

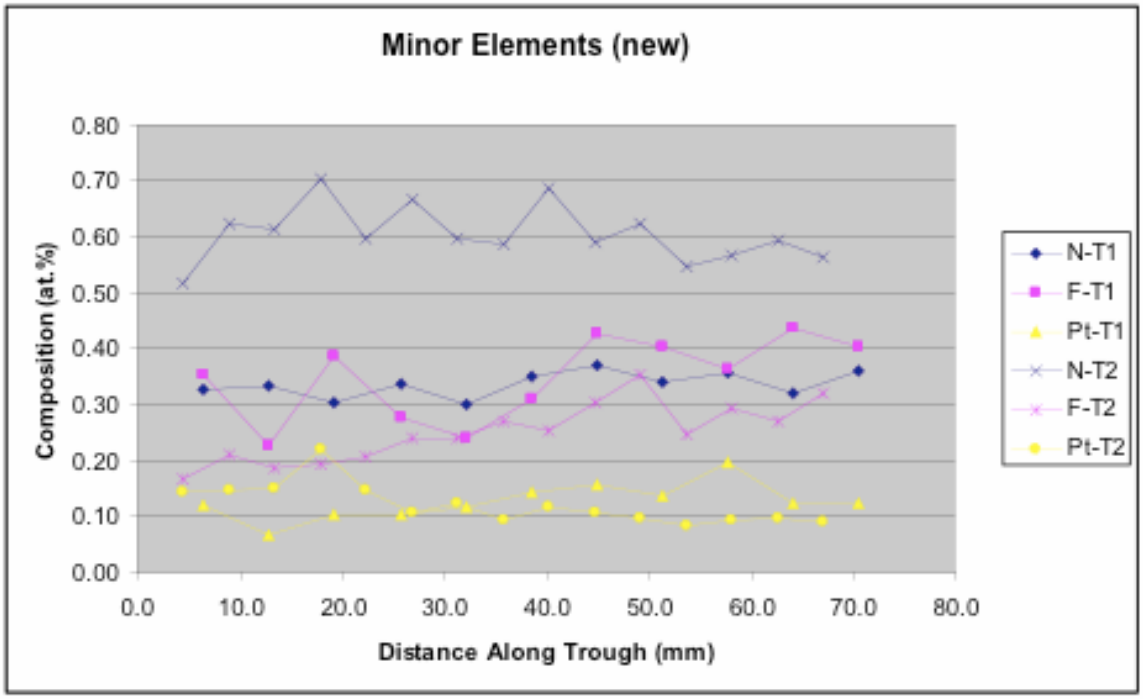

Figure 1- Typical XPS results showing the major and minor elements in the new/unused DOC sample along two troughs (1&2) of the cordierite honeycomb.

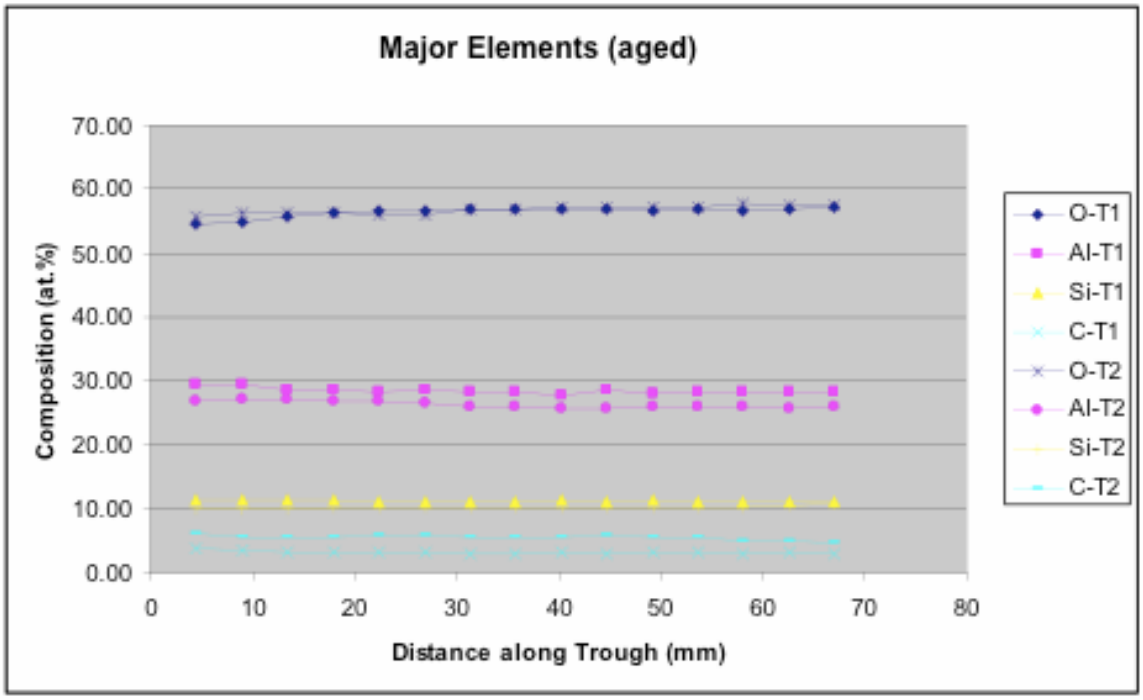

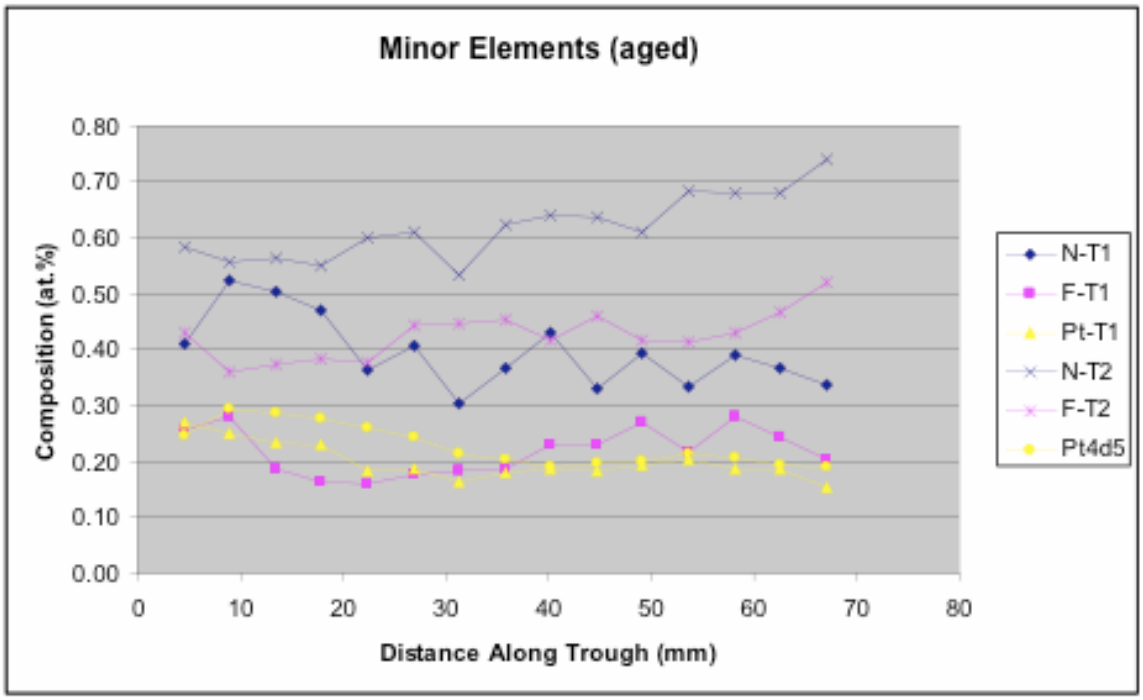

Figure 2- Typical XPS results showing the major and minor elements in the aged DOC sample along two troughs (1&2) of the cordierite honeycomb.

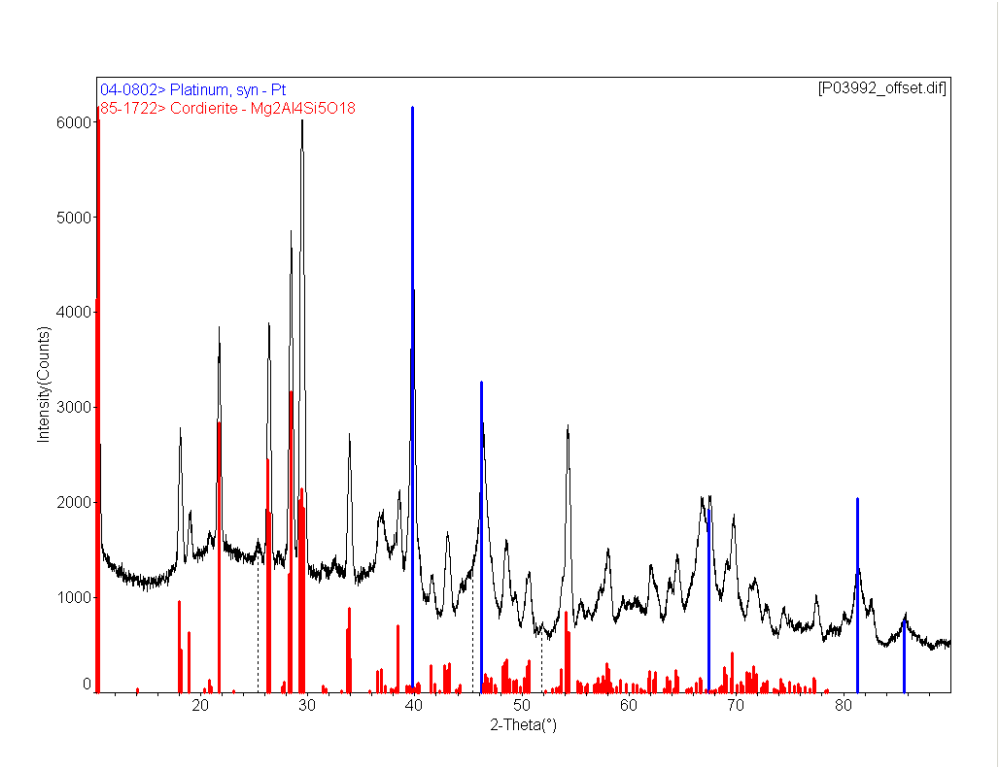

Figure 3- XRD pattern of the aged DOC sample.

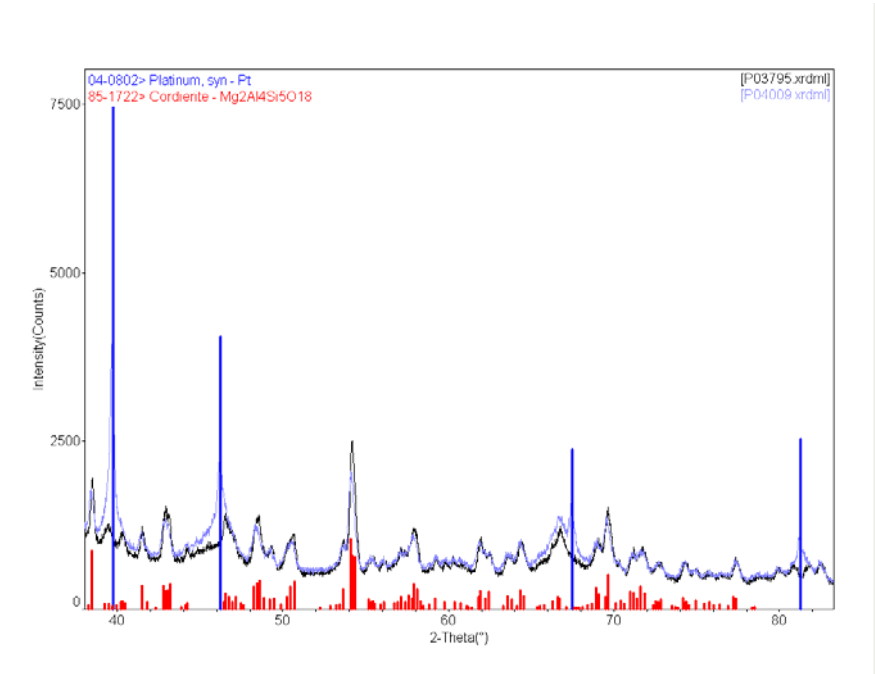

Figure 4- XRD patterns of the new (black curve) and aged (blue curve) DOC samples and highlights the large Pt peaks present in the aged relative to the new DOC.

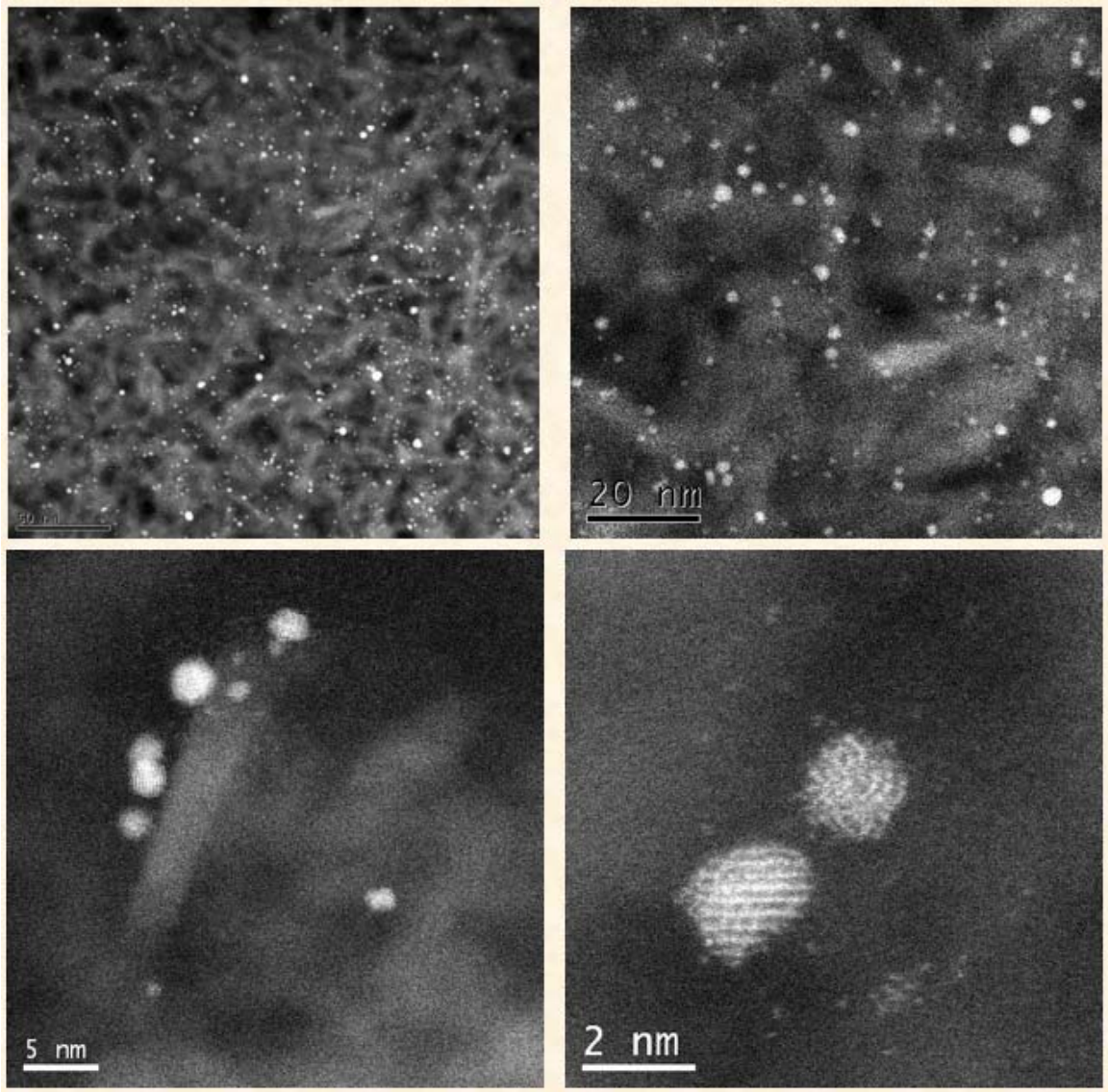

Figure 5 – TEM images showing the near atomically dispersed Pt particles and clusters in the new DOC taken with Aberration-corrected STEM.

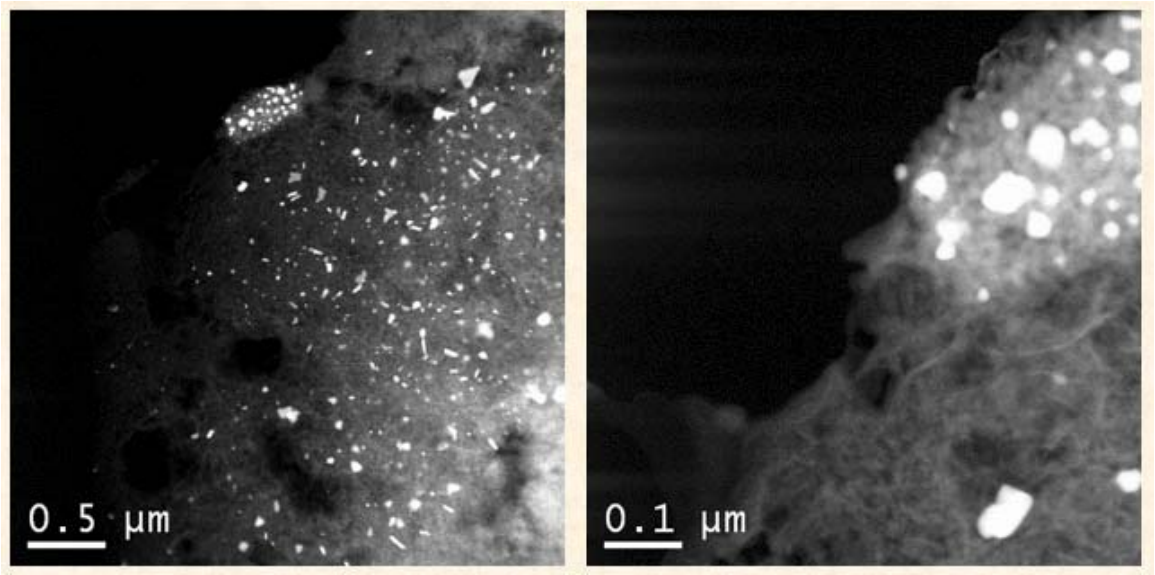

Figure 6 – TEM images showing the large Pt crystals in the aged DOC.

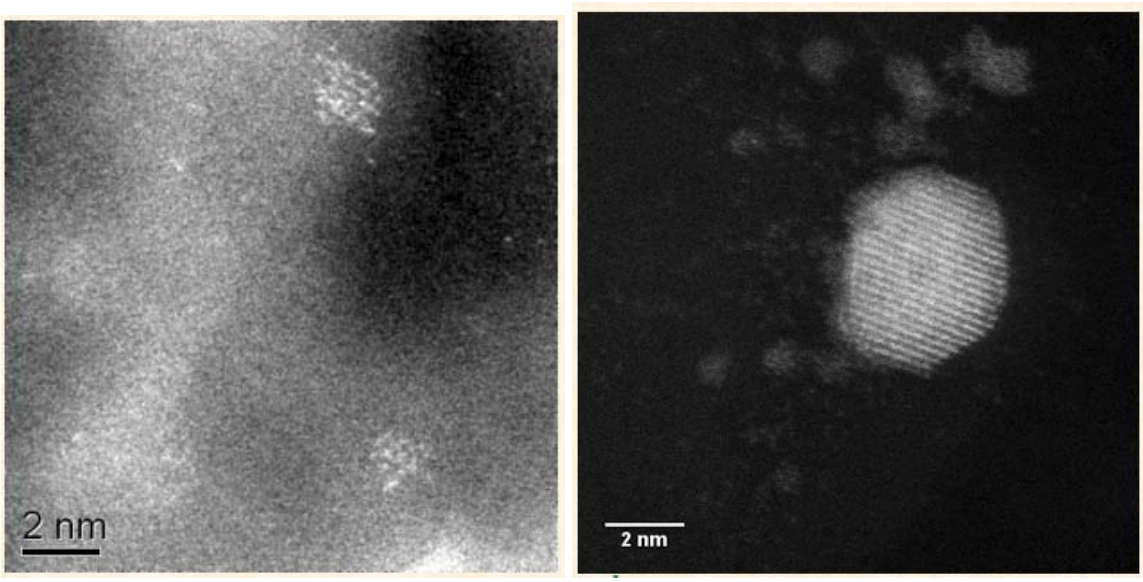

Figure 7 – TEM images showing the near atomically dispersed Pt cluster and particles still present within the aged DOC.

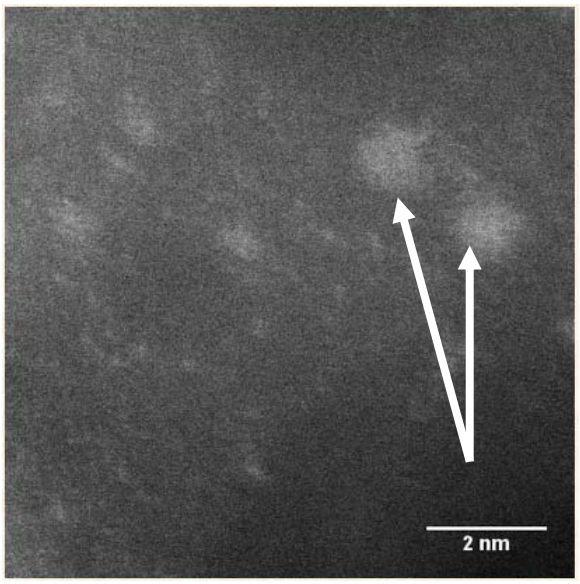

Figure 8 – TEM images showing nanocrystals (white arrows) surrounded by “cloud” (hazy “milky-way”) of Pt clusters within the aged DOC.

Catalysis by First Principles - Can Theoretical Modeling and Experiments Play a Complimentary Role in Catalysis?

C. Narula, W. Shelton, Y. Xu, M. Moses, and L. Allard
Oak Ridge National Laboratory

Objective/Scope

This research focuses on an integrated approach between computational modeling and experimental development, design and testing of new catalyst materials, that we believe will rapidly identify the key physiochemical parameters necessary for improving the catalytic efficiency of these materials. The results will have direct impact on the optimal design, performance, and durability of supported catalysts employed in emission treatment (e.g., lean NO_x catalyst, three-way catalysts, oxidation catalysts, and lean NO_x traps, etc.)

The typical solid catalyst consists of nano-particles on porous supports. The development of new catalytic materials is still dominated by trial and error methods, even though the experimental and theoretical bases for their characterization have improved dramatically in recent years. Although it has been successful, the empirical development of catalytic materials is time consuming and expensive and brings no guarantees of success. Part of the difficulty is that most catalytic materials are highly non-uniform and complex, and most characterization methods provide only average structural data. Now, with improved capabilities for synthesis of nearly uniform catalysts, which offer the prospects of high selectivity as well as susceptibility to incisive characterization combined with state-of-the science characterization methods, including those that allow imaging of individual catalytic sites, we have compelling opportunity to markedly accelerate the advancement of the science and technology of catalysis.

Computational approaches, on the other hand, have been limited to examining processes and phenomena using models that had been much simplified in comparison to real materials. This limitation was mainly a consequence of limitations in computer hardware and in the development of sophisticated algorithms that are computationally efficient. In particular, experimental catalysis has not benefited from the recent advances in high performance computing that enables more realistic simulations (empirical and first-principles) of large ensemble atoms including the local environment of a catalyst site in heterogeneous catalysis. These types of simulations, when combined with incisive microscopic and spectroscopic characterization of catalysts, can lead to a much deeper understanding of the reaction chemistry that is difficult to decipher from experimental work alone.

Thus, a protocol to systematically find the optimum catalyst can be developed that combines the power of theory and experiment for atomistic design of catalytically active sites and can translate the fundamental insights gained directly to a complete catalyst system that can be technically deployed.

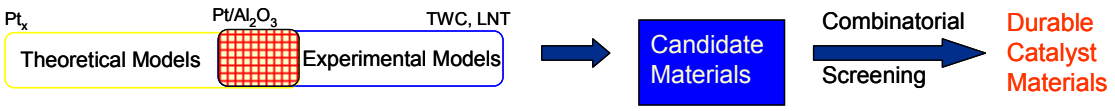

Although it is beyond doubt computationally challenging, the study of surface, nanometer-sized, metal clusters may be accomplished by merging state-of-the-art, density-functional-based, electronic-structure techniques and molecular-dynamic techniques. These techniques provide accurate energetics, force, and electronic information. Theoretical work must be based electronic-structure methods, as opposed to more empirical-based techniques, so as to provide realistic energetics and direct electronic information.

A computationally complex system, in principle, will be a model of a simple catalyst that can be synthesized and evaluated in the laboratory. It is important to point out that such a system for experimentalist will be an idealized simple model catalyst system that will probably model a "real-world" catalyst. Thus it is conceivable that "computationally complex but experimentally simple" system can be examined by both theoretical models and experimental work to forecast improvements in catalyst systems.

Our Goals are as follows:

- Our theoretical goal is to carry out the calculation and simulation of realistic Pt nanoparticle systems (i.e., those equivalent to experiment), in particular by addressing the issues of complex cluster geometries on local bonding effects that determine reactivity. As such, we expect in combination with experiment to identify relevant clusters, and to determine the electronic properties of these clusters.
- Our experimental goal is to prepare and characterize metal carbonyl clusters, decarbonylated metal clusters, sub-nanometer metal particles, and metallic particles (~5 nm) on alumina (commercial high surface area, sol-gel processed, and mesoporous molecular sieve). The characterization of such catalyst is now possible with the availability of ACEM at ORNL. We will then evaluate these systems for CO conversion efficiencies to determine the species that participates in CO oxidation catalysis.
- This approach will allow us to identify the catalyst sites that are responsible for CO, NO_x, and HC oxidation. We will then address support-cluster interaction and design of new durable catalysts systems that can withstand the prolonged operations.

Technical Highlights

Our results on theoretical and experimental work on Platinum-Alumina Systems are summarized in following paragraphs.

Experimental Studies:

2% Pt/γ-Al_2O_3 Catalyst:

As reported previously, we synthesized 2% Pt/γ–alumina by impregnation of γ–alumina with $H_2PtCl_6 \bullet 6H_2O$ followed by calcinations in air at 450ºC. Images of the platinum particles obtained by scanning transmission electron microscope indicate 1.1 nm diameters (avg.) and typically range from 0.6-1.4 nm. The absence of the high angle diffraction peaks for Pt in the X-ray diffraction patterns support the presence of only the small platinum diameters seen by electron microscopy. This catalyst was then annealed at 650°C/5 h in air to obtain larger platinum particles. Peak profile fitting of the high angle platinum reflection in the X-ray

diffraction pattern which had no overlap with alumina reflections indicated we had particles on the order of 25 nm in diameter.

The oxidation catalyst that has ca. 25 nm platinum particles was evaluated in a 5 mL reactor employing a gas flow of 100 cc/min comprised of 5% CO, 5% O_2, and 90% N_2. Temperature readings were record for the reactor inlet gas (T_{Ri}) before it comes in contact with the catalyst. Multiple tests were run under these conditions to evaluate the effect that the CO oxidation reaction has on the platinum particle size:

a. The first test was designed to study the initial effect of CO oxidation. The temperature of the reactor was heated to 150°C then gradually increased in 30°C increments till the CO oxidation became noticeable (light-off condition). The reaction was immediately stopped and catalyst sample was collected. The CO conversion as a function of temperature at 0 and 15 minutes is shown in Figure 1, results of the same test on a catalyst sample with 1 nm Pt particles is also included. CO oxidation initiates between 150-175ºC and is about 3% at 215°C for the 25 nm Pt samples which is about 15°C higher than the 1 nm sample. The X-ray diffraction pattern of the 25 nm tested material after 8.1% CO conversion at 240°C, Figure 2b, indicates about a 2.8 nm increase in the Pt particles size to 27.8 nm in diameter.

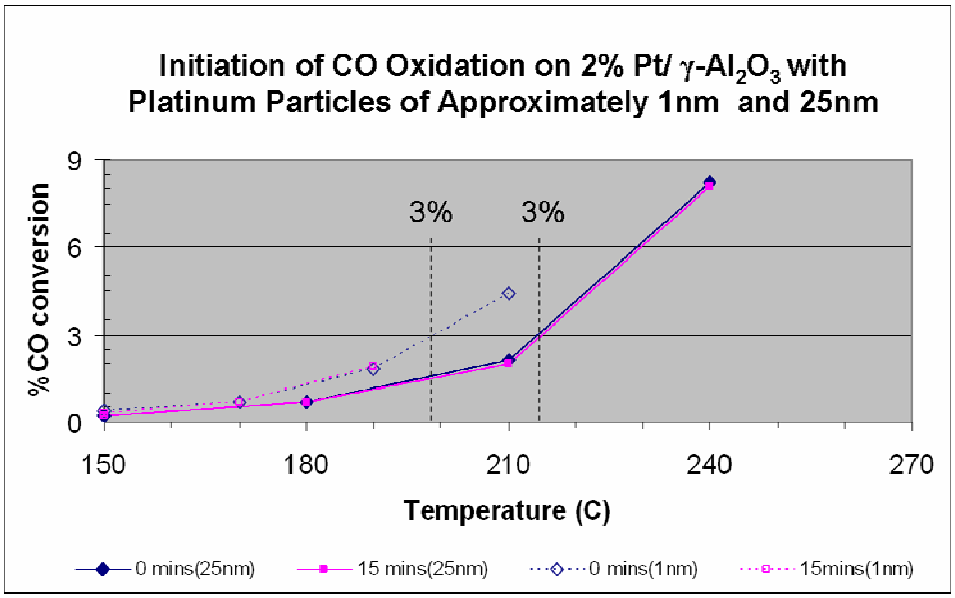

Figure 1: Initiation of catalyst conversion as a function of temperature with sampling at 0 (blue) and 15 (pink) minutes at the indicated temperatures. The solid lines are results for the 2% Pt/ γ-Al_2O_3 annealed at 650°C (ca. 25 nm Pt) and the dotted lines are results for 2% Pt/ γ-Al_2O_3 (ca. 1 nm Pt).

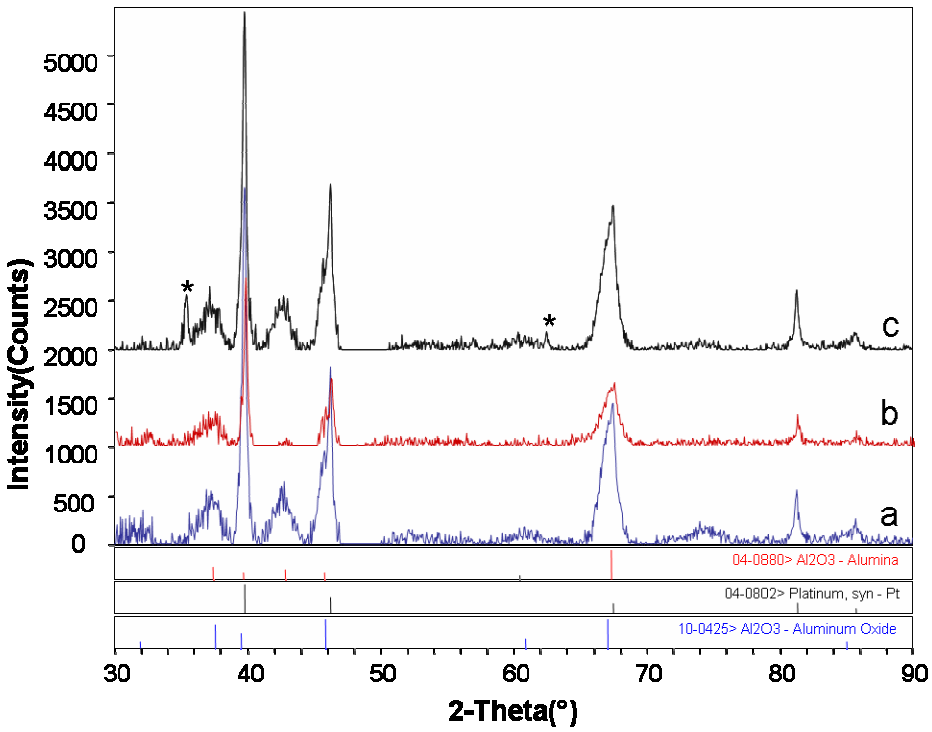

Figure 2: X-ray diffraction pattern of fresh 2% Pt/γ-A_2O_3 annealed at 650°C (a) fresh and after CO oxidation tests: CO conversion (b) initiation (8.1%) (c) full range (3 cycles at 100%).* denotes a sample holder impurity.

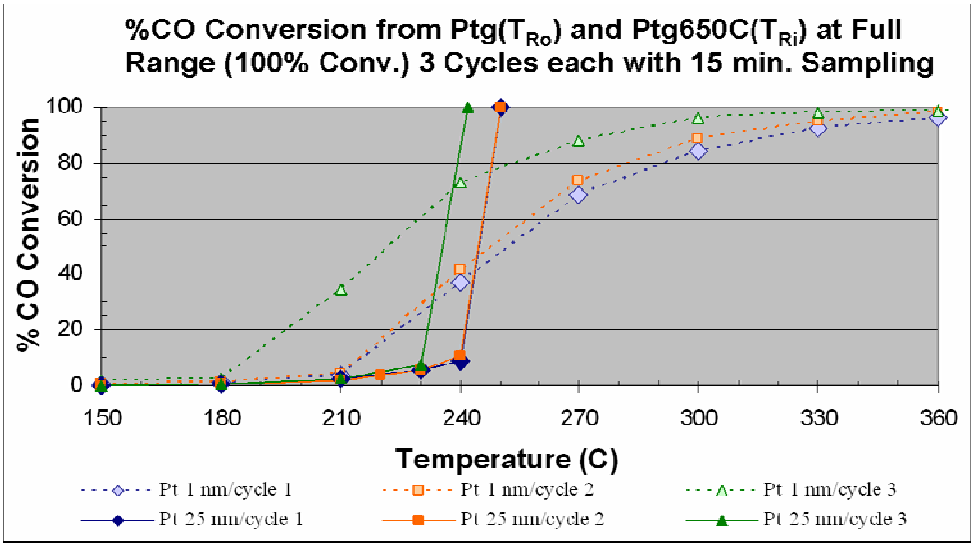

Figure 3: Complete catalyst conversion of CO to CO_2 as a function of temperature with sampling after 15 min. at the given temperature. The solid lines are results for the 2% Pt/ γ-Al_2O_3 annealed at 650°C (ca. 25 nm Pt) and the dotted lines are results for 2% Pt/ γ-Al_2O_3 (ca. 1 nm Pt) catalysts.

b. Another test was done on the 2% Pt/γ-Al_2O_3 catalyst annealed at 650°C to test for complete CO oxidation under similar conditions used for the light-off tests. The same sample was cycled through these conditions 3 times to obtain a "degreened" catalyst. The conversion jumped from approximately 10% conversion at 240°C to 100% at 250°C in the first two cycles; therefore, during the third cycle testing the temperature 242°C was tested, but within 15 minutes at this temperature 100% conversion was reached. The results of all three cycles of this 25 nm Pt sample are presented in Figure 3 along with those for the 1 nm Pt sample presented in the last report. An X-ray diffraction pattern of the tested 25 nm Pt catalyst show a 9.2 nm growth of the Pt particles to a 34.2 nm average diameter, see Figure 2c. A second sample prepared identically but has 30 nm Pt particles according to X-ray diffraction data was also tested for 3 cycles of 100% CO conversion. Identical temperature vs. % CO conversion results were obtained for both the 25 and 30 nm Pt particle samples.

These results suggest the following:

- Cycling of complete conversion testing 3x clearly shows that a "degreening" process is occurring. Comparison of the 100% CO conversion results between the catalysts with 1 nm and 25/30 nm platinum particles see Figure 4, clearly indicates that particles size affects the temperature at which CO oxidation to CO_2 occurs, but after a certain size particle growth has less of an effect.
- The Pt particle size growth in the 25 nm Pt catalyst is apparent from the X-ray powder diffraction data. Further examination of samples by TEM will provide information on changes in particles as a result of CO oxidation.
- The residence time did not effect the conversion of CO to CO_2 over the 2% Pt/γ-Al_2O_3 catalyst with 25 or 30 nm Pt particles which is in contrast to that seen for the 2% Pt/γ-Al_2O_3 catalyst with 1 nm Pt particles.

We have been using Density Functional Theory (DFT) based methods to investigate the oxidation of CO and NO on Pt clusters (Pt_x, x = 1-5 and 10). The results obtained so far indicate that the reaction energetics is strongly dependent on the size of the clusters as well as the extent of oxidation of the clusters.

We first look at the adsorption of the relevant atomic and molecular species on Pt nanoclusters, including O, O_2, CO, CO_2, NO, and NO_2. Figure 4 shows the lowest adsorption energies (i.e., strongest adsorption) for the six species on Pt_x. The adsorption energies of O, O_2, CO_2 and NO_2 all display a maximum at Pt_2 followed by a minimum at around $Pt_{4\text{-}5}$, after which they gradually rise toward the level on the bulk Pt surface, here represented by Pt(111). The adsorption energies of CO and NO, on the other hand, show different behaviors. The adsorption energy of CO rises monotonically with cluster size, so cluster size may serve as a fairly reliable predictor of CO adsorption strength on Pt clusters. That of NO percolates on the smallest Pt_x before rising toward the bulk surface level. Overall, the adsorption of all six species is highly size-dependent in the nano-size regime and substantially stronger than on the bulk Pt surface.

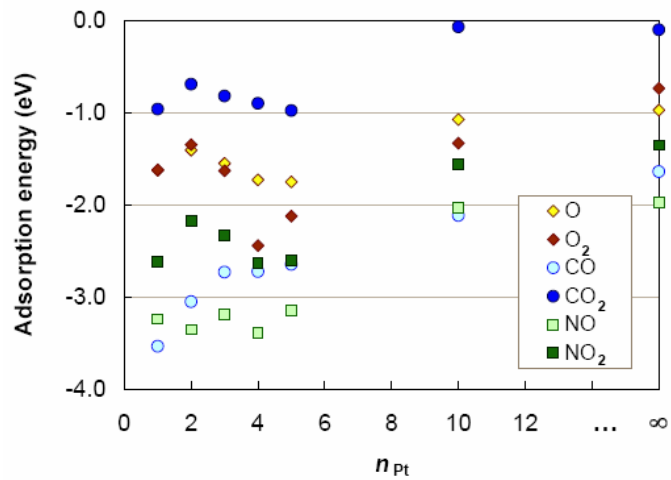

Figure 4: The adsorption energies of O, O_2, CO, CO_2, NO, and NO_2 on Pt_x nanoclusters plotted against the number of Pt atoms in the Pt_x clusters.

That the adsorption of these species is enhanced compared to the bulk Pt surface means that the energy profiles of CO and NO oxidation on Pt_x also differ from their bulk-surface counterparts (Figure 5). CO oxidation on the bulk Pt surface is exothermic every step along the reaction path, but because of the enhanced adsorption of CO, there is a minimum in energy when CO adsorbs on the clusters. The same phenomenon can be seen in NO oxidation. This indicates that the ability of the Pt nanoclusters to catalyze CO and NO oxidation may be inhibited by the strongly adsorbed CO and NO. Furthermore, because of the smaller enthalpy of the overall reaction $NO_{(g)} + ½O_{2(g)} \rightarrow NO_{2(g)}$, the somewhat more strongly adsorbed O atom diminishes the energetic driving force for Pt_x–O + $NO_{(g)} \rightarrow NO_{2(g)}$ and makes the Pt_x clusters insufficient oxidizers for NO oxidation.

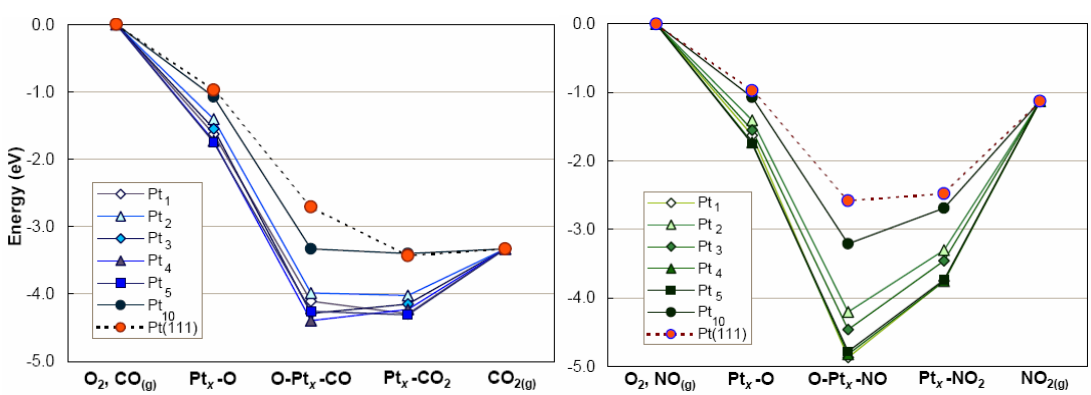

Figure 5: The reaction energy profiles for CO + ½O_2 → CO_2 and NO + ½O_2 → NO_2 on Pt_x (x = 1-5 and 10). The profiles on the bulk Pt surface (represented by the Pt(111) facet) are included for comparison.

2% Pt/MgO Catalyst:

MgO smoke crystals were prepared by burning MgO wire. The smoke crystals were collected in an inverted funnel and used as a catalyst support without further treatment. The MgO support was impregnated with 2% Pt particles by $Pt(acac)_2$ in an acetone solution. The catalyst was slowly calcined at 450°C/15mins before use.

We have also begun to study oxidized Pt nanoclusters on the thermodynamically most stable (100) facet of magnesia (MgO), a model basic oxide surface that is relatively inert toward many adsorbates by DFT. Figure 6 summarizes the latest results. So far, the oxides of the Pt dimmer and trimer exhibit very similar formation energies on MgO(100) compared to those of the free Pt_2 and Pt_3 clusters, while Pt_1O_y have markedly lower formation energies. Nonetheless, it appears that at least the supported Pt_1 and Pt_2 clusters should be oxidized to the same extent ($Pt_1 \rightarrow Pt_1O_3$, $Pt_2 \rightarrow Pt_2O_5$ or Pt_2O_6) on MgO(100) as in the gas phase. Furthermore, the morphologies of the various Pt oxide clusters on MgO(100) also closely resemble their gas-phase counterparts. These results confirm our hypothesis that the oxidation energetics and morphologies of the free Pt nanoclusters should by and large be preserved on a relatively inert surface and lend support to our approach of investigating the free Pt nanoclusters first.

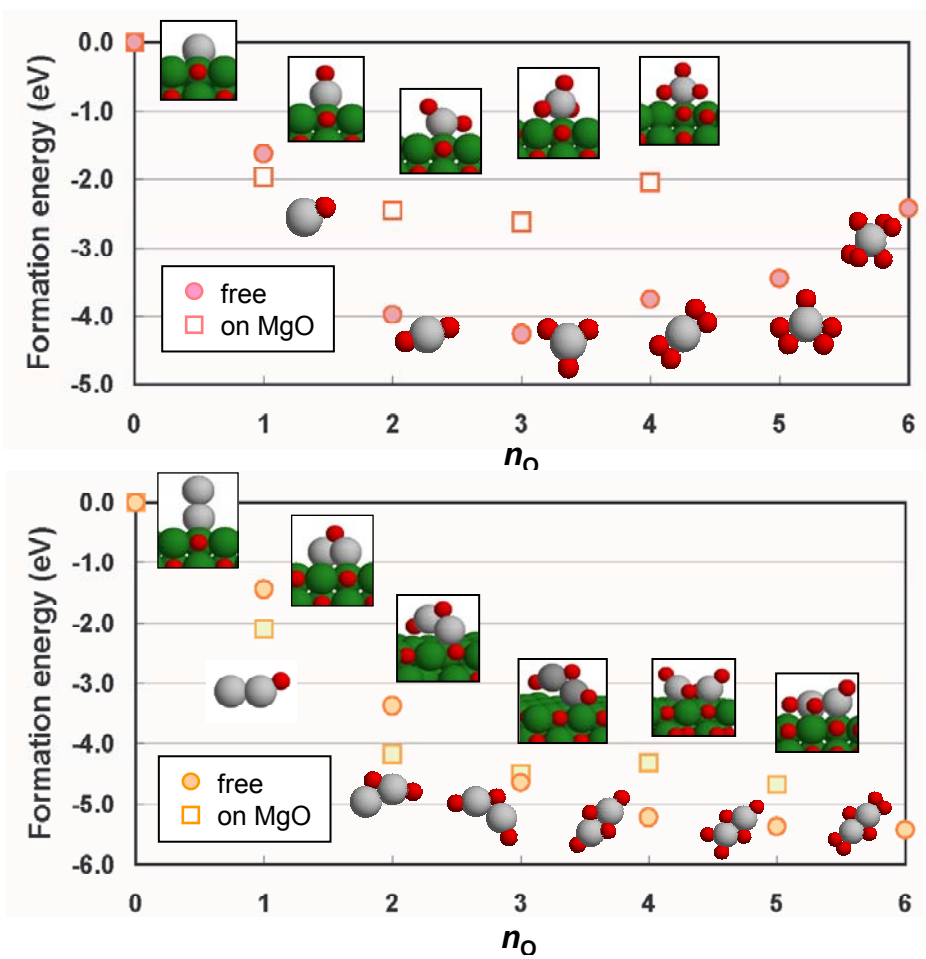

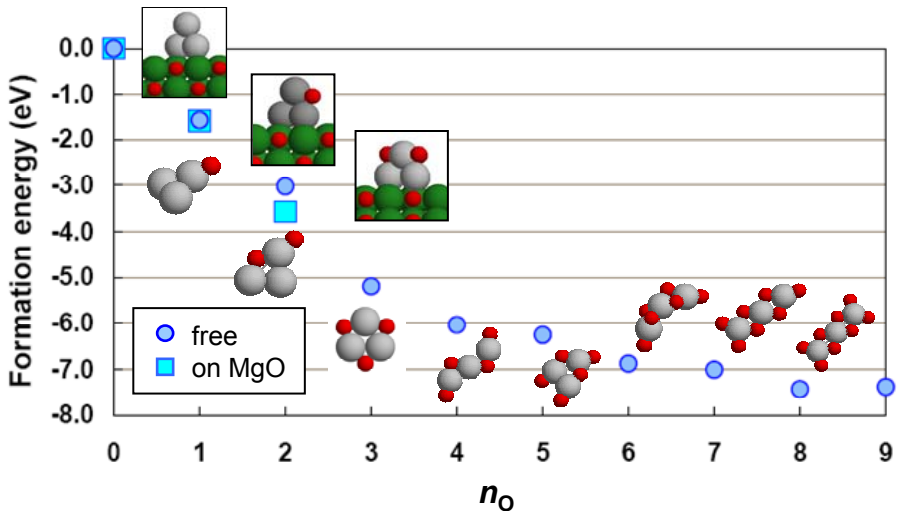

Figure 6: The formation energies of $Pt_{1-3}O_y$ on MgO(100).

These results are interesting since the experimental results show that 10-20 atom Pt clusters rapidly increase in size in the presence of CO at relatively low temperatures. We are carrying out experiments to understand this result.

Next Steps: We plan to carry out the following tasks:

- We plan to complete CO oxidation studies of already synthesized Pt clusters on alumina and MgO to determine the metal species involved in CO oxidation. The results will be compared with the results from theoretical calculation. If consistent, we will proceed with the evaluation of the catalysts for NO_x and hydrocarbon oxidation.

- We will synthesize Pt clusters on sol-gel and molecular sieve alumina. This will create a matrix of samples with varying Pt particles size and oxidation on alumina substrates with increasing surface area and pore structure. We will carry out CO, NO_x and HC oxidation on these samples to study the effect of morphological changes in substrates leading to changes in metal substrate interactions.

- We will continue to investigate the thermochemistry of CO and NO oxidation on free Pt and Pt oxide clusters as well as the properties of Pt and Pt oxide clusters supported on metal oxides (include magnesia and alumina). These investigations will help us gain a better understanding of the structural and catalytic properties of the supported Pt clusters and identify the effect of the support on these important properties.

Barriers: The transfer of HD-2000 electron microscope to CNMS has delayed microstructural analysis of samples. We have submitted a proposal and we expect to be able to use this instrument again beginning August/September 2006.

Publications/Presentations

1. C. K. Narula, M. Moses, L. F. Allard, K. Lester, "Analysis of Microstructural Changes in Lean NO_x Trap Material Isolates Parameters Responsible for Activity Deterioration" Powertrain & Fluid Systems Conference, Society of Automotive Engineers Meeting, Oct 16-19, 2006, Sheraton, Toronto, Canada (Abstract Accepted).

2. C. K. Narula, D. A. Blom, L. F. Allard, M. J. Moses, Y. Xu, W. A. Shelton, W. F. Schneider, "Catalysts by Design - Theoretical and Experimental Studies of Model Catalysts for Lean NOx Treatment", DEER 2006, Detroit, Michigan, (Abstract Accepted).

3. Y. Xu (speaker), W. A. Shelton, and W. F. Schneider, "Nano-scale effects in the oxidation and the reactivity of platinum clusters," AIChE Annual Meeting, San Francisco, CA, 11/2006, abstract accepted.

4. Y. Xu (speaker), W. A. Shelton, and W. F. Schneider, "Platinum clusters for oxidation catalysis: Nano-scale effects in thermodynamics and reactivity," 232nd ACS National Meeting, San Francisco, CA, 9/2006, abstract accepted.

5. Y. Xu, W.A. Shelton, and W. F. Schneider, "The thermodynamic equilibrium compositions, structures, and reaction energies of Pt_xO_y (x = 1-3) clusters predicted from first principles," in press, *Journal of Physical Chemistry B*.

6. Y. Xu, W. A. Shelton, and W. F. Schneider, "Effect of particle size on the oxidizability of platinum clusters," *Journal of Physical Chemistry A*, 110 (2006) 5839.

Durability and Reliability of Ceramic Substrates for Diesel Particulate Filters

Edgar Lara-Curzio and Amit Shyam
Materials Science & Technology Division, Oak Ridge National Laboratory

Objectives/Scope

To develop/implement test methods to characterize the physical and mechanical properties of ceramic Diesel particulate filters (DPFs), and to implement a probabilistic-based analysis to quantify their durability and reliability.

Highlights

The variation of porosity and mechanical properties in cordierite DPFs was investigated.

Technical Progress

Recent measurements on cordierite test specimens revealed a dependence of the fracture toughness, as determined by the double-torsion test method, with the location from where the test specimens were obtained in a Diesel particulate filter. This prompted a study to determine how the microstructure of the filter and its mechanical properties change with location. Figure 1 summarizes the effects of temperature and the stiffness of the test specimen on its fracture toughness. In this plot the modulus values were obtained from the slope of the load versus displacement curves obtained during fracture toughness testing and have not bee corrected for the compliance of the test set-up. It can be observed that fracture toughness increases with the stiffness of the test specimen and that it exhibits an anomalous temperature dependence as discussed in previous reports. Figure 2 presents a series of micrographs that were used to characterize the microstructure of a DPF and to quantify its porosity as a function of location. Work continues to establish correlations between the microstructure of the material and its mechanical properties.

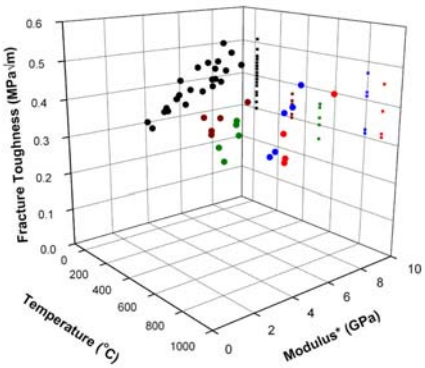

Figure 1. Effect of temperature and stiffness on the fracture toughness of porous cordierite.

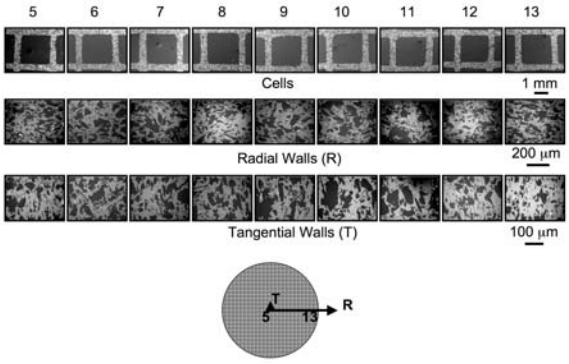

Figure 2. Microstructural analysis of cordierite DPF to assess changes of porosity with location.

Milestones

Report the effect of water vapor on the rate of slow-crack growth, static and dynamic fatigue of cellular cordierite filters at elevated temperatures (March 2006). (Completed)

Meetings

Monthly teleconferences with Cummins and Corning personnel were held during the reporting period.

Advanced Cast Austenitic Stainless Steels for High Temperature Components

P. J. Maziasz, John P. Shingledecker, and N. D. Evans
Oak Ridge National Laboratory

and
M.J Pollard
Caterpillar, Inc.

Objective/Scope

This is the 2nd ORNL CRADA project with Caterpillar. This CRADA project is focused on commercialization of the new CF8C-Plus cast austenitic stainless steel, which was developed during the first ORNL/CAT CRADA. CF8C-Plus stainless steel is a cost-effective material upgrade for much more performance, durability and temperature capability relative to current heavy-duty diesel engine exhaust components made from SiMo ductile cast iron. In FY2005, this project completed the initial properties data base needed for alternate materials selection, and component design or redesign, including fatigue, thermal fatigue, and creep, and studies of aged materials. Longer term creep-testing and fatigue studies at much lower frequencies are underway, together with new tests directly related to specific new component applications, like turbocharger housings. This CRADA (Cooperative Research and Development Agreement) project (ORNL02-0658) was extended beyond the initial 3-year term last year, and will be completed in July, 2007. Requests for more detailed information on this project should be made directly to Caterpillar, Inc.

Highlights

Caterpillar, Inc.
Caterpillar recently announced that the new cast CF8C-Plus stainless steel will be used for the body casting for the Caterpillar Regeneration System (CRS) for on-highway truck engines, beginning in 2007.

ORNL
Creep-testing of new commercial heats of CF8C-Plus Cu/W steel, which show a significant strength advantage at 750°C and above, continued this quarter.

There has been significant commercial interest in CF8C-Plus and CF8C-Plus Cu/W from several commercial turbocharger manufacturers, and ORNL is working with a trial-licensee foundry to produce and test appropriate material.

Technical Progress, 3rd Quarter, FY2006

Background
Current cast iron heavy diesel engine exhaust manifolds and turbocharger housings are being pushed beyond their temperature capabilities as normal duty cycles approach or exceed 750°C; the rapid and severe thermal cycling contributes to increased failures. The new cast CF8C-Plus austenitic stainless steel is now being commercialized and evaluated for this and many other

high-temperature applications. Caterpillar, Inc. and ORNL are completing the systematic and thorough properties data base required by designers to optimize component design, and are characterizing the properties of trial or prototype commercially cast stainless steel components.

Approach

Multiple commercial heats of CF8C-Plus have been cast by several commercial foundries, including static sand and centrifugal casting methods. Now, both large and small prototype CF8C-Plus components have been cast. In July, 2004, a large turbine housing for an industrial gas-turbine was cast by MetalTek, International, Inc. from an 8000 lb heat of the new CF8C-Plus stainless steel. In 2005, three foundries obtained trial-licenses for CF8C-Plus steel, including MetalTek and Stainless Foundry & Engineering. By the end of 2005, over 31,000 lb of CF8C-Plus components have been cast, including exhaust manifolds, and some new, thin-walled piping. In 2005, new commercial heats of CF8C-Plus Cu/W were made, and in 2006 found to have more tensile strength and more creep resistance than CF8C-Plus at 750°C and above. The outstanding castability and freedom from the need for post-cast heat-treatments are distinct advantages for CF8C-Plus and CF8C-Plus Cu/W steels for advanced diesel components, and many other applications.

Technical Progress – Caterpillar, Inc.

Caterpillar announced that after completing prototyping and testing, it will use the new cast CF8C-Plus stainless steel as the body casting for the Caterpillar Regeneration System (CRS) for on-highway truck diesel engines, beginning in 2007. The CRS device burns diesel fuel in the exhaust stream to heat the diesel particulate filter, in order to oxidize soot and regenerate the filter. This component is subject to extreme temperatures and thermal cycling, which makes the CF8C-Plus stainless steel a durable and relatively low-cost choice for this application.

The large industrial gas-turbine housing cast of CF8C-Plus stainless steel by MetalTek (6,700 lb) for Solar Turbines has been sectioned and inspected previously, and was found to be free of defects. Mechanical properties testing to evaluate this component continues. CF8C-Plus offers superior creep strength and castability compared to the standard CF8C steel, and may reduce or eliminate the need for costly weld repairs on the combustor housing.

Technical Progress – ORNL

In 2005, a new commercial heat of modified CF8C-Plus steel with further additions of Cu and W, was made for ORNL by MetalTek. The initial tensile testing of as-cast material found that the Cu and W additions significantly boosted the YS relative to CF8C and CF8C-Plus at 600-850°C, particularly above 750°C. Tensile testing and preliminary fatigue testing (very high cycling frequency) of as-cast material are complete. Aging continued at ORNL this quarter on these steels, and creep, and slower cycle-rate fatigue and creep-fatigue studies were completed this quarter. Longer-term creep-rupture testing at 750°C at lower stresses, which are more relevant to the low-stress exhaust component applications of CF8C-Plus steel, continue this quarter.

New casting and testing initiatives began this quarter to address casting and properties of thin-walled castings of CF8C-Plus Cu/W most appropriate to exhaust manifold and turbocharger

casing components. Input from component manufacturers has been factored into the current testing and evaluation.

Communications/Visits/Travel

Detailed team communications between ORNL and Caterpillar occur regularly. The new 3 year CRADA began on July 21, 2002, when the previous CRADA ended and is scheduled to end on July 21, 2005. The two-year ORNL/Caterpillar CRADA extension was done last year until July 21, 2007.

Status of Milestones (ORNL for DOE)

FY2006 (1) Complete properties measurements of new CF8C-Plus Cu/W heats, including static and centrifugally cast materials, at 700-850°C (02/06). Completed. (2) Expand commercialization opportunities and complete licensing of CF8C-Plus to commercial foundries and other end-users (08/06). Generally on-track, and some efforts continue, but reductions in FY2006 funding have seriously curtailed this effort. Commercial end-user interest in CF8C-Plus Cu/W is also now a factor in this milestone.

Publications/Presentations/Awards

Publications:

J. P. Shingledecker, P. J. Maziasz, N. D. Evans, and M. J. Pollard, "Creep Behavior of a New Cast Austenitic Alloy," was accepted for publication in the *International Journal of Pressure Vessels and Piping*, a special issue on New Steels, to be published May 2006.

Presentations:

None.

Friction and Wear Reduction in Diesel Engine Valve Trains

Peter Blau and Jun Qu
Oak Ridge National Laboratory

Objective/Scope

The objective of this effort is to enable the selection and use of improved materials, surface treatments, and lubricating strategies for value train components in energy-efficient diesel engines. Depending on engine design and operating conditions, between 5 and 20% of the friction losses in an internal combustion engine are attributable to the rubbing between valve train components. Wear and consequent leaks around valve seats can reduce cylinder pressure and engine efficiency. Contacting surfaces in the valve train include the valve heads, seats, tappets, guides, and stems. This effort is designed to address key rubbing interfaces within the valve train where there are opportunities to employ advanced materials and surface treatments to reduce friction and save energy.

A two-pronged, interdisciplinary approach is planned to address both materials and lubrication-related aspects. The first task concerns the design and construction of a laboratory testing apparatus to simulate the thermal, chemical, and mechanical contact environment characteristic of valves and valve seats. A second task involves improving the performance of the valve stems as they oscillate within the valve guides. The latter takes into consideration not only the selection of stem and guide materials, but also the characteristics of thin lubricant films and the micromechanics of the moving surfaces. Therefore, this project embodies surface science and tribology to solve practical engineering challenges.

Technical Highlights

Design of a High-Temperature, Controlled Environment, Valve Material Testing System. Work continues on the design and construction of a controlled-environment, repetitive-impact system. It is intended as a tool for studying the durability of candidate value materials, identifying their primary modes of surface damage, and providing guidance for the selection of new bulk materials, coatings, and surface treatments for valves in engines that burn a variety of fuels.

Construction has been completed on the oscillating drive assembly that actuates the simulated valve-seat contact and on the test stand on which it is mounted. The drive system is based on a fractional-horsepower, variable-speed motor with an off-set roller/lifter assembly that will be used to drive the repetitively impacting valve or valve material specimen within an environmental chamber.

The next subassembly to be built includes the fixtures for holding test specimens inside the heating chamber. Design of a novel specimen fixture that enables either diesel engine valves or simple coupons to be tested has been completed. Heat-resistant alloys have been ordered to fabricate the fixture, and machining of the parts will begin when those materials are received.

Design of the surrounding chamber, its heating system, and the controlled gas supply continues. It will be modeled along the lines of a high temperature, controlled atmosphere testing system that is used to conduct studies of the fatigue of high-temperature alloys at ORNL.

Due to an unexpected reduction and a temporary interruption in funding, completion of the apparatus is expected to be delayed until December 2006.

In the mean time, current and candidate valve materials will be characterized in preparation for baseline testing in the completed apparatus.

Future Plans

1) Continue to design and build an elevated temperature, repetitive-impact testing system for exhaust and intake valve materials.

2) Working with ORNL researchers H.-T. Lin, H. Wang, and A. Wereszczak, conduct a comparison of the dynamic and slow-speed scratch hardness characteristics of Ti-Al engine valve materials.

Travel

P. Blau traveled to Waterville, Maine, to attend the Gordon Research Conference on Tribology (19-23 June) and to present an invited lecture entitled: "Is laboratory tribotesting relevant? - Scaling results from the bench-top to the highway." The focus was on how materials researchers can improve the quality and relevance of laboratory test data so that it relates better to the performance of the materials in full-scale components. Since the GRC series encourages free exchange of emerging ideas and the use of unpublished information, there is to be no proceedings.

Status of Milestones

1) Complete low-speed friction experiments that will serve as the basis for modeling the boundary-lubrication characteristics of valve stems and guides. Completed. **(03/06)**

2) Construct a valve seat simulator and establish baseline material performance data under high-temperature, engine-like conditions. **(09/06** – delayed until **12/06)**

Publications and Presentations

(see Travel)

Advanced Machining and Sensor Concepts

Albert Shih
University of Michigan

Objective/Scope

The objective of this research is to investigate new technologies for cost-effective machining of Ti alloys and the manufacturing of HCCI diesel fuel systems. The three dimensional (3D) finite element modeling and experimental validation of drilling Ti-6Al-4V were conducted. Effects of process parameters on the stress and temperature distributions of the drill and workpiece are investigated in detail.

Technical Highlights

Daniel Johnson, a new student who will work on the manufacturing of HCCI fuel systems, starts the research at Caterpillar Technical Center at Moorsillve, IL in May. He is using the summer to learn the basics of diesel fuel systems manufacturing and identifying materials and manufacturing needs in advanced HCCI fuel systems.

The research in 3D FEM modeling of Ti drilling continues. The model includes fully adaptive unstructured mesh generation, tight thermo-mechanically coupling, deformable tool-chip-workpiece contact, interfacial heat transfer across the tool-chip boundary, momentum effects at high speeds and constitutive models appropriate for high strain rate, large deformation analyses. To validate the efficacy of numerical and constitutive formulations used, actual drilling tests are performed on Ti-6Al-4V. The thrust force and torque are measured and compared with modeling results. The model provides good estimation of thrust force but the torque is overestimated by 50%. This study shows that the FEM drilling model is able to predict changes in forces, temperatures, and stresses with respect to drilling process parameters.

1. Finite Element Model

The AdvantEdge™ 3D machining simulation software by Third Wave Systems with updated-Lagrangian finite element method, continuous remeshing, and adaptive meshing techniques [1] was used to model Ti machining process. The work-material model contains the power-law strain hardening, thermal softening and rate sensitivity [1]. Fig. 1 shows the 3D finite element mesh using a conventional twist drill. The 4-node tetrahedral finite element was used to model the workpiece and tool. The models of tool and workpiece include 4,600 and 5,500 initial nodes, respectively. The workpiece is modeled with a predrilled cone-shape blind hole to enable the early full-engagement of the whole drill point region to reduce the simulation time.

2. Experimental Setup

The model is validated by comparison with experimentally measured thrust force and torque. The drilling test was conducted on a Mori Seiki computer numerical control machining center using a M2 high speed steel twist drill with 3.97 mm diameter, 0.77 mm web thickness, 118° point angle, and 30° helix angle. Workpiece is a 6.35 mm thick Ti-6Al-4V plate. Drilling tests were conducted at three drill rotational speeds, 734, 1100, and 1468 rpm, which corresponds to 9.1, 13.7, and 18.3 m/min drill peripheral cutting speed, respectively. A constant feed of 0.051 mm/rev was used.

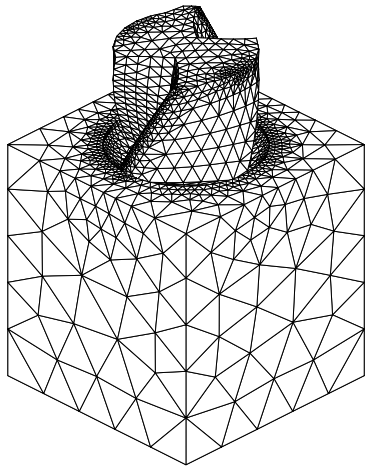

Fig. 1. Finite element mesh for 3D drilling model.

3. Model Validation

Fig. 2 shows the finite element modeling and averages of experimentally measured thrust forces and torques. The FEM model provides a reasonable estimation of thrust force. The thrust force is less than 20% underestimation, but the torque can be overestimated by 50%. In experiments, a large amount of heat is generated from the initial contact of the drill and workpiece to the full engagement of drill point region with workpiece. It results in high temperature and softens the workpiece. In comparison, the drill temperature is at room temperature when the cutting edge fully engages the workpiece in FEM. As a result, the workpiece is harder and results in higher torque. Another possible reason for the discrepancy is the inaccuracy of material and friction modeling. A constant coefficient of friction was used. The lack of accurate friction modeling is, as usual, a limitation in FEM modeling of machining processes [2].

4. Chip Formation and Temperature and Stress Distributions

In drilling, the chip formation has a significant influence on the thrust force and torque as well as the temperature and tool performance. As a convenient tool, finite element modeling provides an excellent insight to the material deformation during drilling. An example of the chip formation process is shown in Fig. 3. The cutting speed for the selected example is 13.7 m/min. The chip and the engagement of the drill and workpiece are shown in Fig. 3(a).

Fig. 3(b) shows the temperature distribution of the chip and workpiece. The temperature of Ti chip is higher than the cut surface on the workpiece. The highest temperature, about 453°C, is concentrated in regions contacting the drill cutting edge near the drill margin, where the cutting speed is the highest along the cutting edge. The distribution of von Mises stress of the chip and workpiece is shown in Fig. 3(c). The region of high stress coincides with the region with high temperature.

5. Tool Performance

Tool temperature is a key factor that accelerates the tool wear and limits the cutting speed and productivity in Ti machining. Experimental measurement of tool temperature is difficult. On the contrary, the finite element simulation can predict the tool temperature under various cutting

conditions. Fig. 4(a) shows the temperature distribution on the drill flank face. The high temperature of this twist drill is concentrated at the cutting edge near the margin. The peak temperature reaches 405°C which is slightly lower than the peak chip temperature, after drilling about 0.008 s. The tool temperature is increasing with the drilling time [3]. Such high temperature is detrimental to the tool life. The distribution of von Mises stress of the tool is shown in Fig. 4(b). Similar to the chip, the region of high stress almost coincides with the region of high temperature. The peak stress of tool is 4651 MPa which is higher than that of chips.

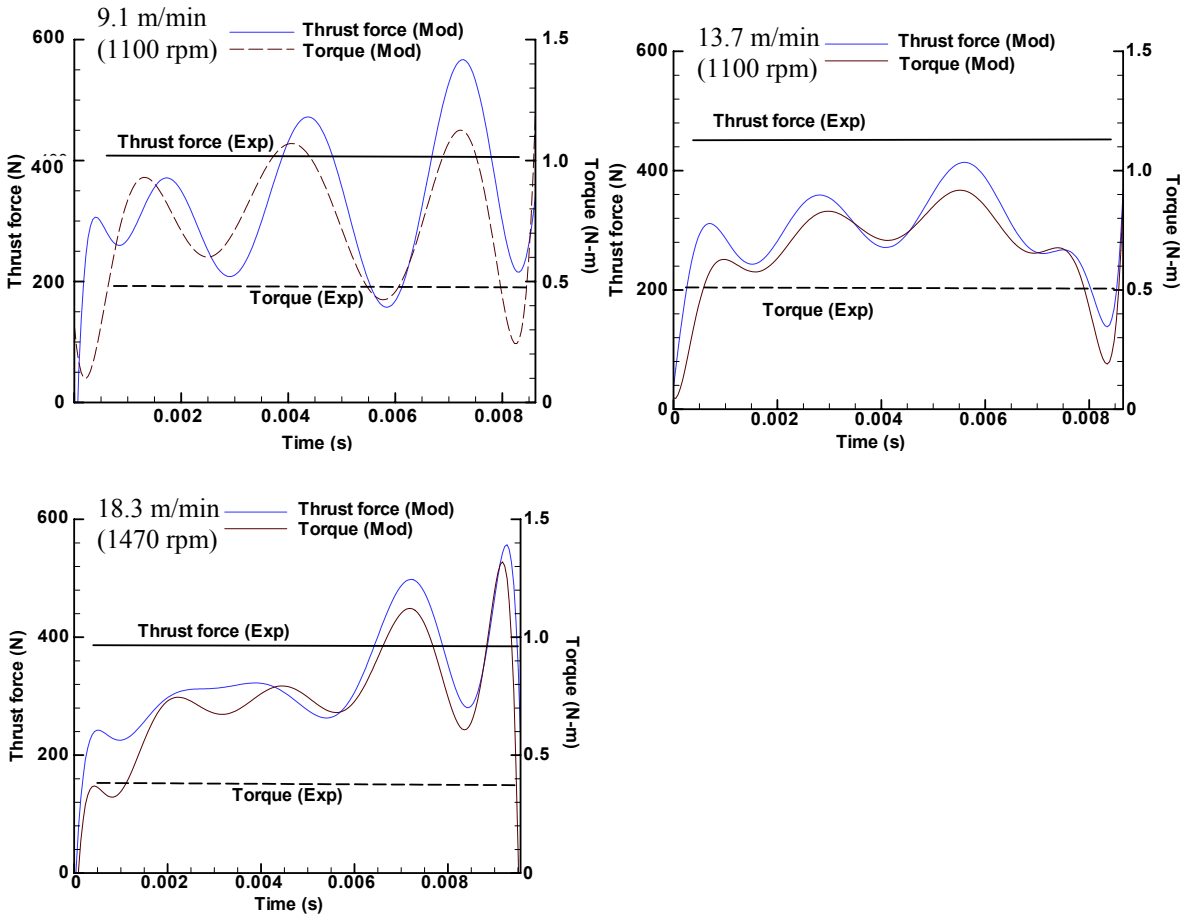

Fig. 2. Comparison of modeling and experimental thrust forces and torques

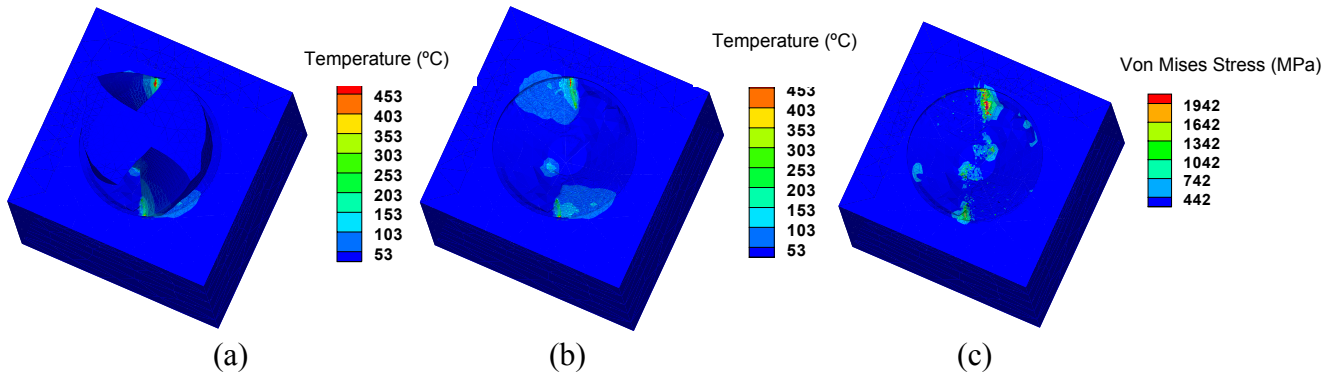

Fig. 3. FEM results: (a) drill, chip, and workpiece temperature, (b) chip and workpiece temperature, and (c) chip and workpiece von Mises stress (13.7 m/min peripheral cutting speed).

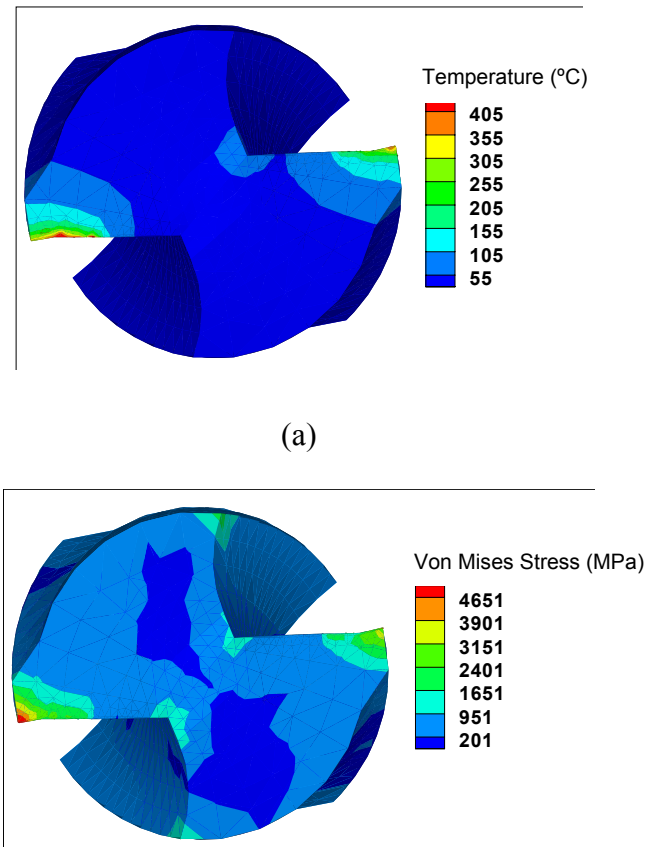

Fig. 4. FEM results of drill: (a) temperature and (b) Mises stress distributions (13.7 m/min peripheral cutting speed).

6. Effect of Cutting Speed

Fig. 5 shows the effect of cutting speed on the peak temperature and von Mises stress on chip and tool. The peak chip temperature increases from 294ºC at 9.1 m/min cutting speed to 589ºC at 18.3 m/min cutting speed. The peak tool temperature increases from 241°C at 9.1 m/min cutting speed to 532°C at 18.3 m/min cutting speed. This demonstrates the effect of high speed on tool temperature quantitatively. The peak tool stress also increases from 3176 MPa at 9.1 m/min cutting speed to 5861 MPa at 18.3 m/min cutting speed. The peak chip stress does not linearly increase with the cutting speed. The maximum chip stress occurs at 13.7 m/min cutting speed. Further increase of cutting speed results in decreased stress because the thermal softening effect outweighs the strain rate hardening effect.

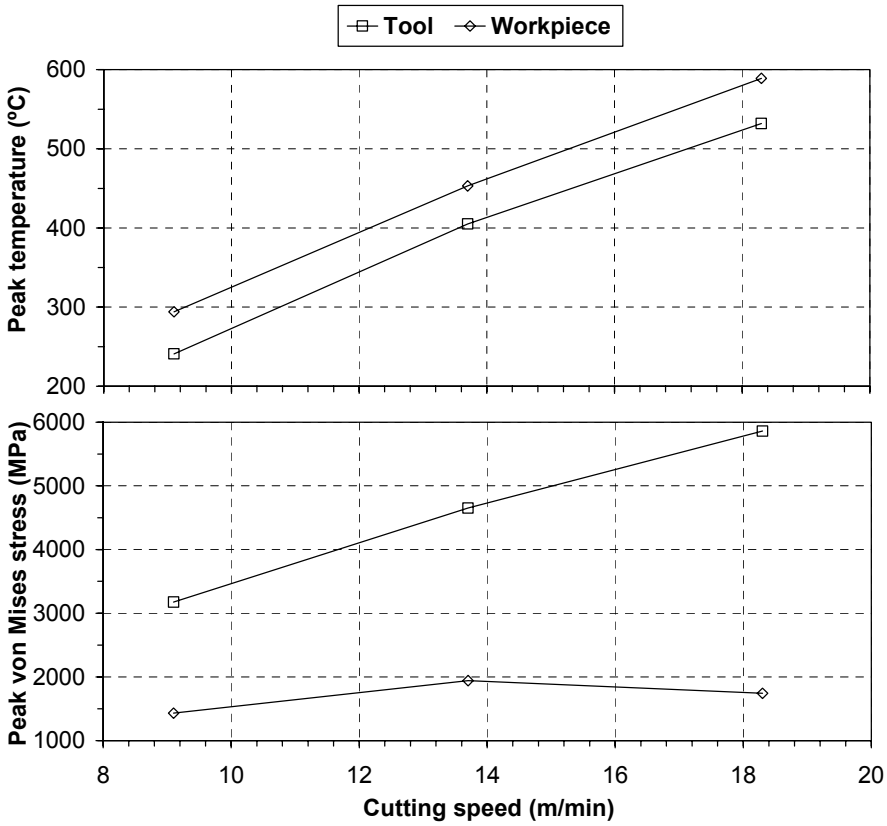

Fig. 5. Peak temperature and von Mises stress vs. drill peripheral cutting speed.

<u>Future Work</u>

On Ti drilling, the research will continue to improve the modeling accuracy and is expected to complete by the end of the year. Research effort will be devoted to advance the knowledge in mechanics of the chip formation process in drilling of Ti. Distributions of cutting forces, stress, strain, and temperature across the chisel and cutting edges will be evaluated to gain better understanding of the material deformation in drilling. The research is expected to gradually transition to HCCI fuel system materials and manufacturing.

Status of Milestones

Milestone 1: Experimental study of Ti drilling.

Status: Extensive tests of Ti drilling have been conducted and reported. The 183 m/min cutting speed and 156 mm^3/s material removal rate have been achieved in drilling Ti-6Al-4V using 4 mm diameter WC-Co spiral point drill. The high throughput drilling of Ti alloy is proved technically feasible.

Milestone 2: 3D finite element modeling of titanium drilling process.

Status: FEM drilling modeling has been conducted and validated with experimental results. Further improvement of the FEM drilling model is currently ongoing.

Milestone 3: Investigation of TiC-based cutting tool material.

Status: Exploratory tests of two TiC-Ni_3Al cermets with 5% and 9% matrix material have both failed. The performance of the tool inserts with surface and cutting edge professionally prepared has been tested without obvious advantages over the current WC-Co tools. The brittleness of the TiC-Ni_3Al is identified as the main direction to improve for its future application as tool material.

Milestone 4: Measure of Ti drilling temperature.

Status: The inverse heat transfer method was developed to analyze the tool temperature in Ti drilling. High drill temperature was observed in drilling Ti, particularly at high cutting speed.

Milestone 5: Metallurgical analysis of machined surface and chips

Status: SEM, XRD, electron microprobe, and nanoindentation tests were conducted on the machined Ti-6Al-4V surface and chips after the high throughput drillling.

Publications

R. Li and A. J. Shih, 2006, "Finite Element Modeling of 3D Turning of Titanium," *International Journal of Advanced Manufacturing Technology*, 29(3-4), 253-261.

R. Li, P. Hegde, A.J. Shih, 2006, "High Throughput Drilling of Titanium Alloys," *International Journal of Machine Tools and Manufacture* (in print).

R. Li and A.J. Shih, "Inverse Heat Transfer Solution of Tool Temperature in Titanium Drilling," Journal of Manufacturing Science and Engineering, submitted.

R. Li, A.J. Shih, 2004, "Finite Element Modeling of 3D Turning of Titanium," 2004 ASME International Mechanical Engineering Congress & Exposition, November 13-19, 2004, Anaheim CA.

R. Li, A.J. Shih, 2006, "High Throughput Drilling of Titanium Alloys," 2006 International Conference on Frontiers of Design and Manufacturing, Guangzhou, China, June 19-22, 2006.

T.D. Marusich, S. Usui, R. Aphale, N. Saini, R. Li, and A.J. Shih, 2006, "Three-Dimensional Finite Element Modeling of Drilling Processes," 2006 ASME International Conference on Manufacturing Science and Engineering, October 8-11, 2006, Ypsilanti, Michigan (submitted in 2006).

References

[1] T.D. Marusich, M. Ortiz, 1995, “Modeling and Simulation of High-Speed Machining,” International Journal for Numerical Methods in Engineering, 38(21), 3675-3694.

[2] van Luttervelt, C.A., Childs, T.H.C., Jawahir, I.S., Klocke, F., Venuvinod, P.K., 1998, “Present Situation and Future Trends in Modelling of Machining Operations -- Progress Report of the CIRP Working Group `Modelling of Machining Operations',” CIRP Annals - Manufacturing Technology, 47, 587-626.

[3] R. Li and A.J. Shih, “Inverse Heat Transfer Solution of Tool Temperature in Titanium Drilling,” Journal of Manufacturing Science and Engineering, submitted.

Synergistic Process-Enhanced Grinding of Advanced Engine Materials

R. H. Chand
Oak Ridge National Laboratory

Objective/Scope

Brief description of the objective and the three tasks associated with SPEG are as follows:

The objective of this effort is to understand, develop, and apply synergistic process-enhanced grinding (SPEG) to improve the efficiency of grinding advanced materials while ensuring surface quality.

Task 1: Conduct a comprehensive investigation of the current state of the art in SPEG methods. This study will include identification of both U.S. and non-U.S. developments, including where the leading research efforts and applications of technology are being implemented.

Task 2: Modify one or more existing machine tools at ORNL to conduct instrumented, SPEG experiments on ceramics, cermets, and/or metal matrix composites that are candidates for diesel engine components.

Task 3: Develop and use a high-speed, instrumented scratch testing system to study the microstructural response of advanced materials like ceramics and composites to the high deformation rates they experience during grinding. The completion of the instrument and an initial series of experiments are planned for the end of FY 2006.

Progress to date

Task 1: Based on the extensive search and evaluation conducted during the past eight months, we have identified as a ***breakthrough technology*** the water jet guided laser cutting and dicing system by Synova from Switzerland. The system is best described in Synova's web site and is quoted as follows and illustrated in Figure 1.

"The conventional focused laser beam has a limited working distance of just a few millimeters due to beam divergence. As a result, the conventional laser generates a heat-affected zone in the material causing damage. Contamination is also an issue as the molten material is not expelled. Laser MicroJet® technology employs a laser beam which is completely reflected at the air-water interface, where the beam can be guided over a distance up to 10 cm. The water jet cools the substrate while removing the molten material from the cut and avoiding contamination."

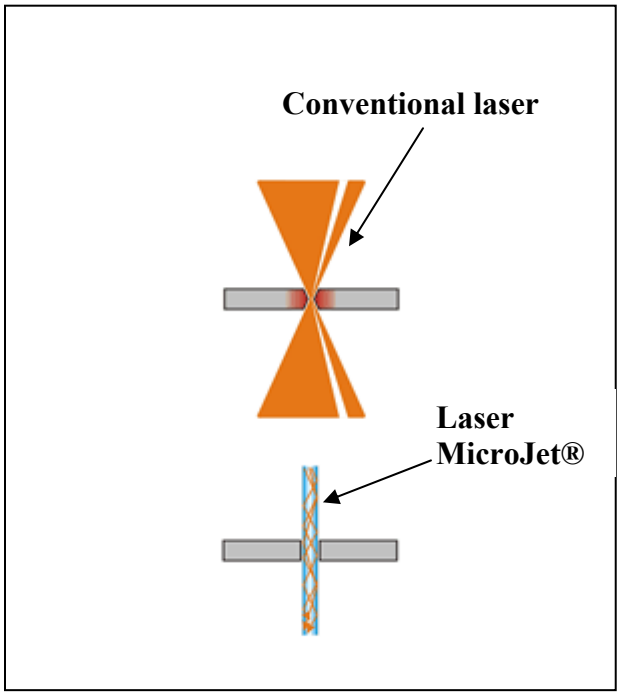

Figure 1. Illustration of Conventional & Water Jet Guided Laser

Task 2:

2.1. Work on Laser healing of surface cracks in silicon nitride roller-follower for diesel engine application, as reported in the last report, has not begun. Legal department is evaluating the non-disclosure agreement between Ceradyne and ORNL.

2.2. As a first step to synergistic process enhanced ID grinding of a diesel engine roller follower a new system incorporating a constant controlled force hone is being designed and a vertical milling machine is being instrumented for the test. Figure 2 below illustrates the hone design.

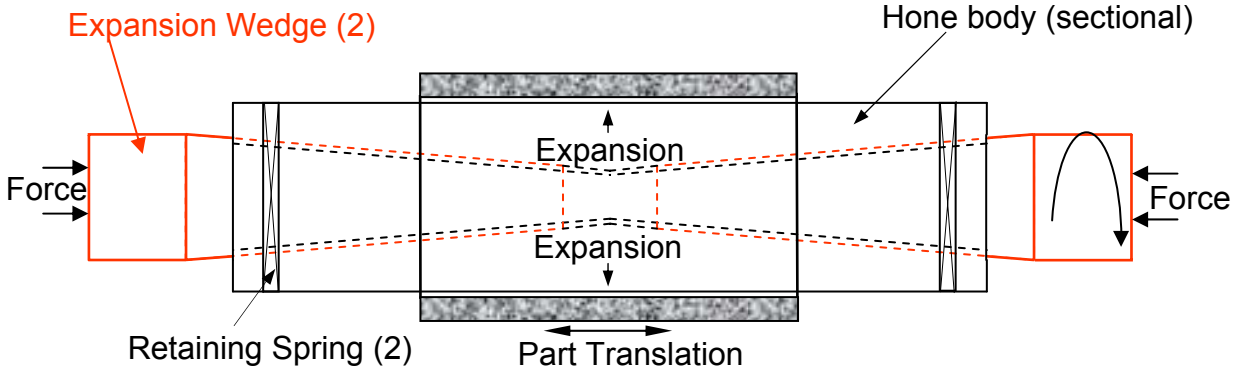

Figure 2. Illustration of a Constant Controlled Force Hone

2.3. A patentable, state of the art invention ensued from the efforts to design a honing system which would enable in situ cooling for the superabrasive grains on the hone surface. Figure 3 illustrates the Internally Cooled Hone.

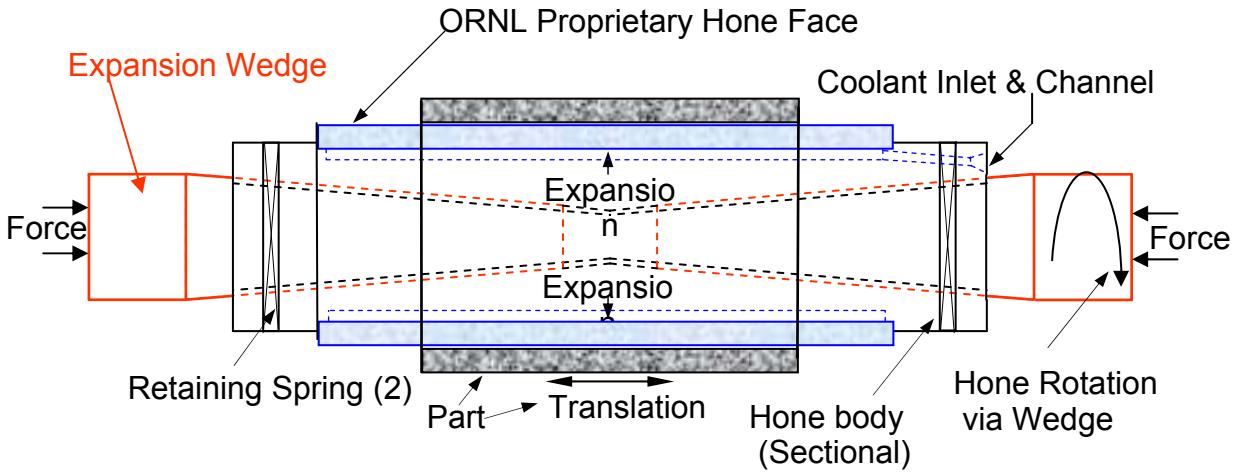

Figure 3. Illustration of a Proprietary Internally Cooled Hone

2.4. Wheels are being prepared to test the feasibility of laser truing and dressing of resin and metal bonded superabrasive wheels. The feasibility study is expected to be completed by the end of FY 06.

Task 3:

3.1. Jun Qu's mathematical model, reported as follows in the last report, has been put on hold for lack of funds. It is hoped that the experimental verification of the model can be conducted in FY07.

$$MRR = C\left(\frac{\alpha \cdot l^{1/2} \cdot E}{K_c^{1/2} \cdot H^{19/12-\lambda/3}}\right) \cdot \left(\frac{\gamma^{1/12+2\lambda/3} \cdot l_s^{1/4+2\lambda}}{d_s^{1/24+\lambda/3} \cdot f_v^{1/18+4\lambda/9}}\right) \cdot \left(\frac{v_s}{w^{1/12+2\lambda/3} \cdot a^{1/24+\lambda/3}}\right) \cdot P_n^{13/12+2\lambda/3}$$

Work material properties — Wheel specs and dressing condition — Grinding parameters

Where MRR (mm^3/s): Material removal rate

P_n: Normal grinding force

C: Material-independent constant

α, λ: Material-dependent constants

l: Grain size of work material

E: Elastic modulus of work material

K_c: Fracture toughness of work material

H: Hardness of work material
γ: dressing factor
l_s: Particle size of grinding wheel abrasive grits
d_s: Grinding wheel diameter
f_v: Volume fraction of the abrasive of grinding wheel (diamond concentration)
v_s: Surface speed of grinding wheel
w: Grinding width
a: Depth of cut

3.2. A diamond wheel consisting of in-line diamond grits, as reported in the last report, has been designed. A search for a vendor capable of building this wheel is underway.

Future Plans

Task 1: Continue with the exploration and evaluation of Laser MicroJet® technology.

Task 2: Further evaluate the advanced honing system and file for disclosure.

Task 3: Build the test wheel.

Travel

None this quarter.

FY 2006 Milestones

1) Survey of non-traditional machining processes that combine synergistic effects to enhance materials removal completed.

2) Complete construction of a high strain-rate scratch testing system to enable basic grinding studies under environmentally-controlled conditions. (**09/06**)

Presentations and Publications

None this quarter.

NDE Development for Ceramic Valves for Diesel Engines

J. G. Sun and J. S. Trethewey*

Argonne National Laboratory
***Caterpillar, Inc.**

Objective/Scope

Emission reduction in diesel engines designated to burn fuels from several sources has lead to the need to assess ceramic valves to reduce corrosion and emission. The objective of this work is to evaluate several nondestructive evaluation (NDE) methods to detect defect/damage in structural ceramic valves for diesel engines. One primary NDE method to be addressed is elastic optical scattering. The end target is to demonstrate that NDE data can be correlated to material damage as well as used to predict material microstructural and mechanical properties. There are two tasks to be carried out: (1) Characterize subsurface defects and machining damage in flexure-bar specimens of NT551 and SN235 silicon nitrides (Si_3N_4) to be used as valve materials. Laser-scattering studies will be conducted at various wavelengths using a He-Ne laser and a tunable-wavelength solid-state laser to optimize detection sensitivity. NDE studies will be coupled with examination of surface/subsurface microstructure and fracture surface to determine defect/damage depth and fracture origin. NDE data will also be correlated with mechanical properties. (2) Assess and evaluate surface and subsurface damage in Si_3N_4 and TiAl valves to be tested in a bench rig and in an engine. All valves will be examined at ANL prior to test, during periodic scheduled shut downs, and at the end of the planned test runs.

Technical Highlights

Work during this period (April-June 2006) focused on acquisition and analysis of laser-scattering NDE data for 14 silicon-nitride and titanium-aluminide valves that were tested in a Caterpillar natural-gas G3406 generator set for 100 hours at NTRC in ORNL.

1. Laser-Scatter NDE Evaluation of Engine-Tested Valves

During this period we acquired and analyzed laser-scattering NDE data for 10 Si_3N_4 and 4 TiAl valves that were run successfully for 100 hours in a Caterpillar natural-gas G3406 generator set at the National Transportation Research Center (NTRC). Table 1 lists and Fig. 1 shows a photograph of these valves. It is seen that all valve-head surfaces were covered by a coat of combustion soot. The coating is generally thicker on exhaust valves, especially for valves positioned at E3 and E15. However, the impact area of the valve surface with the seat insert is clean without any deposit. The impact area is not entirely within the conical contact surface; it lies around the edge between the contact surface and the fillet surface, as illustrated in Fig. 2.

The coating on the valve surface affects the laser NDE scan in two ways. First, because the scan starts from the top edge of the conical contact surface, the extra thickness of the coating makes the initial focusing difficult. Second, the coating causes optical attenuation and scattering, so a thick coat will reduce the sensitivity of laser-scatter detection of the valve surface. However, detection of surface/subsurface degradation is possible under thinner coating (e.g., along the fillet radius towards the stem surface). Despite of the difficulties, laser-scatter scan images were successfully acquired that are suitable to evaluate valve conditions. Further, because the impact area was not coated, the NDE data for this area is accurate and contains detailed information about surface/subsurface degradation.

Table 1. List of 100 h engine-tested Si_3N_4 and TiAl valves.

No.	Valve type	Valve #	Position in engine	NDE scan
1	Si_3N_4 intake	20	I2	Head
2	Si_3N_4 intake	21	I4	Head
3	Si_3N_4 intake	25	I6	Head
4	Si_3N_4 intake	28	I8	Head
5	Si_3N_4 intake	33	I10	Head
6	Si_3N_4 intake	41	I12	Head
7	Si_3N_4 exhaust	11	E1	Head
8	Si_3N_4 exhaust	17	E3	Head
9	Si_3N_4 exhaust	9	E5	Head
10	Si_3N_4 exhaust	32	E7	Head
11	TiAl exhaust	5	E9	Head
12	TiAl exhaust	6	E11	Head
13	TiAl exhaust	7	E13	Head
14	TiAl exhaust	8	E15	Head

Fig. 1. Photograph of 100 h engine-tested Si_3N_4 and TiAl valves.

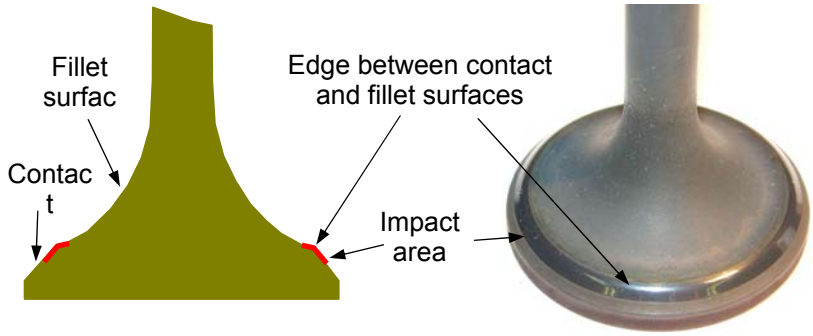

Fig. 2. Location of impact area on valve surface that was impacted with the seat insert.

NDE results representing typical valves of Si_3N_4 intake, Si_3N_4 exhaust, and TiAl exhaust are presented and discussed below. Figure 3 shows the laser-scatter image of the valve-head surface of Si_3N_4 intake valve #20 that was positioned as I2 in the engine for the 100-h test. The combustion coating has some effect on scatter intensity in the contact and fillet surfaces. Within the impact area, shown in the enlarged NDE image, the scatter intensity in the conical contact surface is higher that that in the fillet surface (see the location of the edge), which could indicate a difference of wear on the two surfaces. Nevertheless, no apparent damage was detected within the entire impact region.

Figure 4 shows the laser-scatter image of the valve-head surface of Si_3N_4 exhaust valve #11 positioned as E1 in the engine for the 100-h test. The combustion coating on this valve is thin, so the valve surface underneath the coating is clearly imaged. The impact region for this valve shows relatively higher scatter intensity than the surrounding surface. From the enlarged NDE image, many individual spots of <50μm in size with higher scatter intensity are detected; these spots are likely the distributed porosities in the ceramic material. The NDE data within the impact region also exhibit multiple bands of scatter-intensity variation; which could be an artifact due to slight laser-incident-angle variation that will be investigate in the next period. Despite these NDE indications of general wear from engine test, no significant damage such as crack or void was detected for all Si_3N_4 exhaust valves.

Figure 5 shows the laser-scatter image of the valve-head surface of TiAl exhaust valve #8 positioned as E15 in the engine for the 100-h test. The combustion coating on this and other TiAl valves induces very high scatter than that from the bare TiAl surface. In order to show scatter image for both coated and uncoated surfaces, the scatter intensity is scaled logarithmically in this image (this is a common practice in presenting optical data). For this and other TiAl valves, two types of damage indications were observed. First, several high scatter-intensity spots with sizes up to ~1 mm were detected within the impact region (see enlarged image in Fig. 5). Second, the impact region exhibits considerable wear damage represented by distributed scatter-intensity variations over the entire impact region. These results indicate that the impact damage in TiAl valves appears to be progressing at a faster rate than those observed in the Si_3N_4 valves.

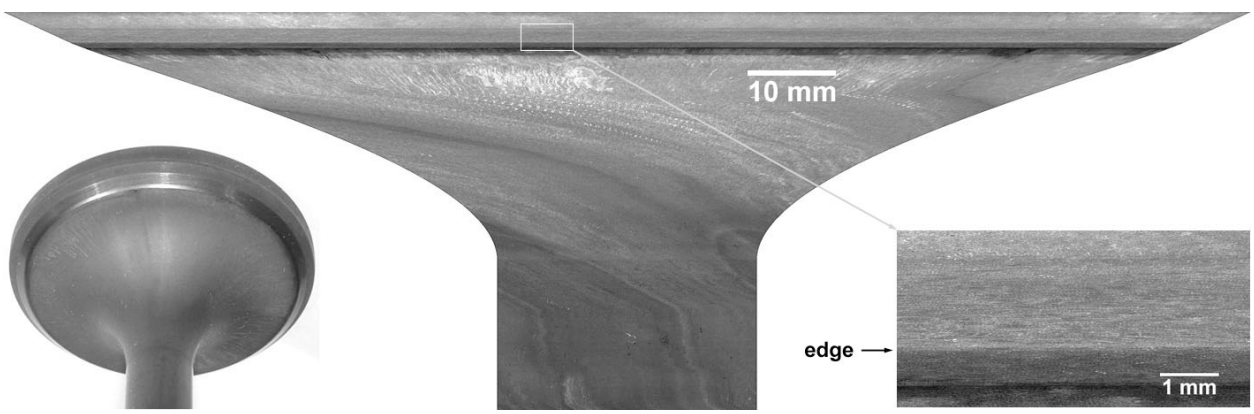

Fig. 3. Laser-scatter scan image of head surface of Si_3N_4 intake valve #20 (at I2 in engine) after 100-h engine test.

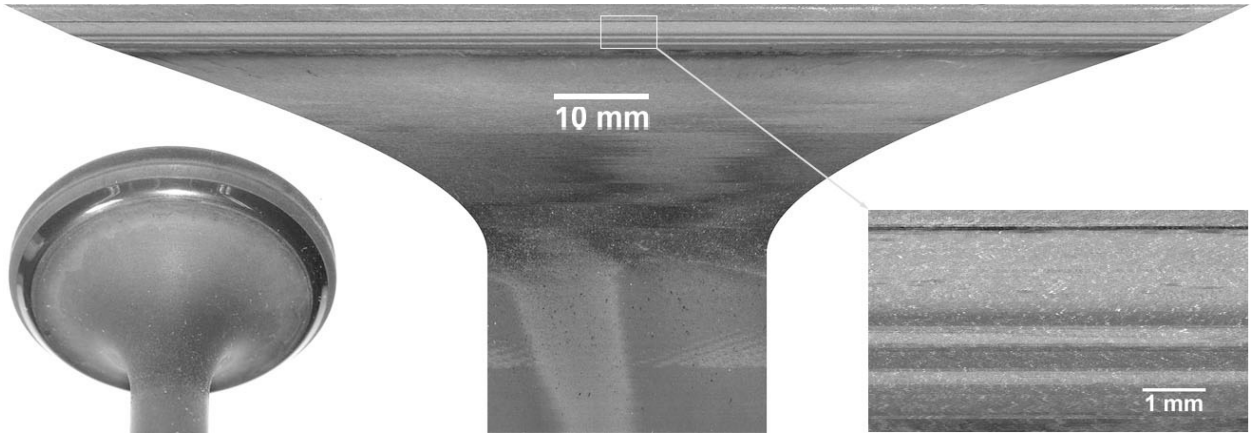

Fig. 4. Laser-scatter scan image of head surface of Si_3N_4 exhaust valve #11 (at E1 in engine) after 100-h engine test.

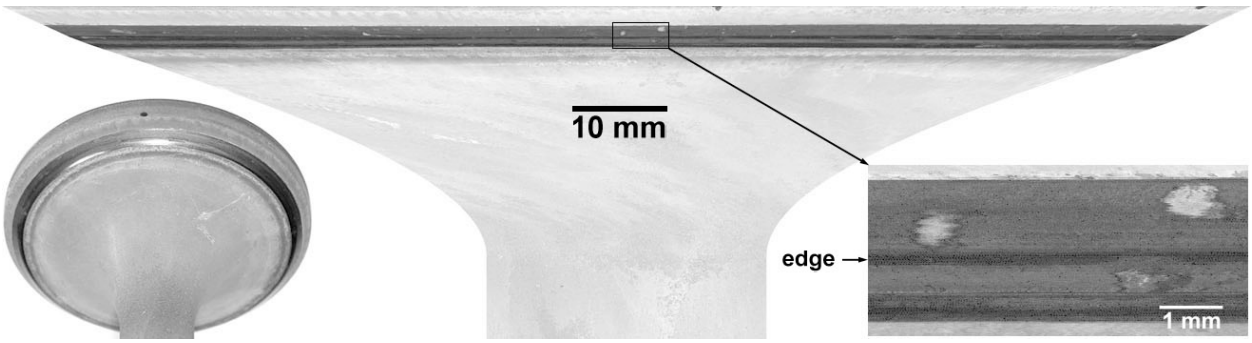

Fig. 5. Laser-scatter scan image (in log-intensity scale) of head surface of TiAl valve #8 (at E15 in engine) after 100-h engine test.

Figure 6 shows photomicrographs of impact surfaces in Si_3N_4 intake valve #20, Si_3N_4 exhaust valve #11, and TiAl exhaust valve #8. For Si_3N_4 intake valve #20, the original machining roughness is still present, with little or no wear is observed. For Si_3N_4 exhaust valve #11, the machining roughness has been worn off, only little remaining along the fillet surface. The worn surface appears smooth, with distributed porosity spots and few subsurface damage marks (bright line) that are probably remnants of the original machining damage. For the TiAl exhaust valve #8, however, a large spot with clear boundary is observed. Material corrosion is suspected within this area, which shows higher scattering as detected in the NDE data (this spot is seen in the enlarged image in Fig. 5). In addition, the impact surface of the TiAl valve becomes very rough, with significant surface wear/damages. In general, the micrographic observations of these valves are consistent with those detected by the laser scatter NDE.

The 14 Si_3N_4 and TiAl valves have been reinstalled in the natural gas G3406 generator set at the NTRC for the second phase (500 hours) testing. NDE inspection of these valves will be conducted after this phase is completed and results will be presented in the next period.

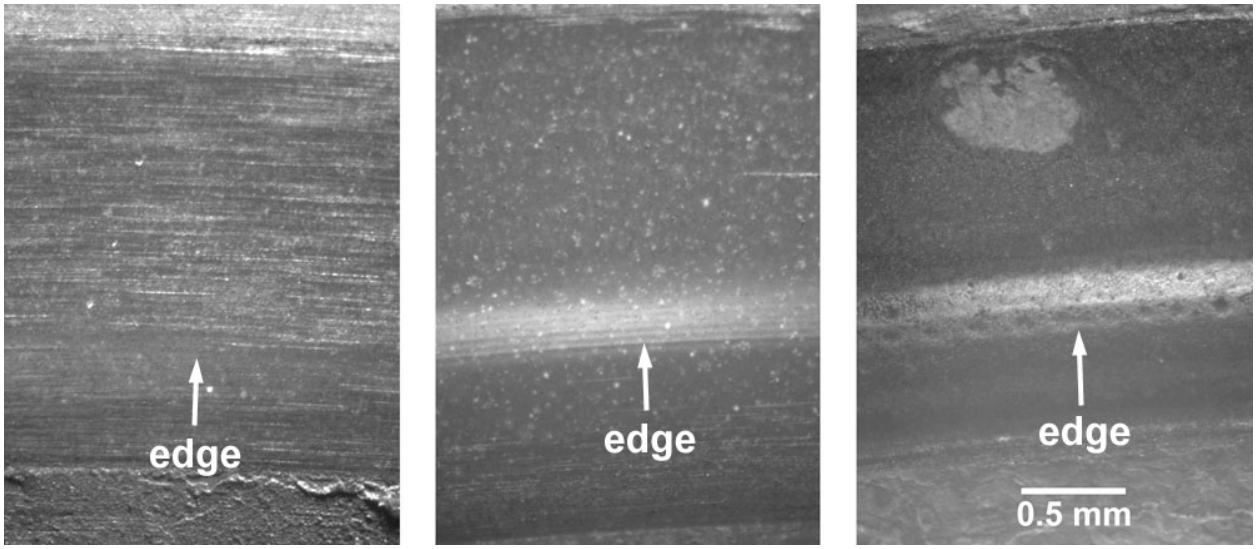

Si_3N_4 intake #20 Si_3N_4 exhaust #11 TiAl exhaust #8

Fig. 6. Photomicrographs of impact surfaces of Si_3N_4 and TiAl valves after 100-h engine test.

2. Development of a Cross-Polarization Confocal System for Measurement of 3D Subsurface Microstructure in Silicon Nitride Ceramics

A US patent for this technology was granted in this period (see publication). Work is continued on measurement and analysis detailed subsurface crack parameters (e.g., crack angle, depth, etc) by this technology. Results will be presented in the next period.

Status of Milestones

Current ANL milestones are on schedule.

Communications/Visits/Travel

None this period.

Problems Encountered

None this period.

Publications

J. G. Sun, "Device and Nondestructive Method to Determine Subsurface Micro-Structure in Dense Materials," U.S. Patent No. 7,042,556, issued May 9, 2006.

Life Prediction of Diesel Engine Components

H. T. Lin, T. P. Kirkland, Hong Wang, A. A. Wereszczak
Oak Ridge National Laboratory

Jeremy Trethewey and Nan Yang
Caterpillar Inc.

Objective/Scope

The valid prediction of mechanical reliability and service life is a prerequisite for the successful implementation of structural ceramics and advanced intermetallic alloys as internal combustion engine components. There are three primary goals of this research project which contribute toward that implementation: the generation of mechanical engineering data from ambient to high temperatures of candidate structural ceramics and intermetallic alloys; the microstructural characterization of failure phenomena in these ceramics and alloys and components fabricated from them; and the application and verification of probabilistic life prediction methods using diesel engine components as test cases. For all three stages, results are provided to both the material suppliers and component end-users.

The systematic study of candidate structural ceramics (primarily silicon nitride) for internal combustion engine components is undertaken as a function of temperature (< 1200°C), environment, time, and machining conditions. Properties such as strength and fatigue will be characterized via flexure and rotary bend testing.

The second goal of the program is to characterize the evolution and role of damage mechanisms, and changes in microstructure linked to the ceramic's mechanical performance, at representative engine component service conditions. These will be examined using several analytical techniques including optical and scanning electron microscopy. Specifically, several microstructural aspects of failure will be characterized:

(1) strength-limiting flaw-type identification;
(2) edge, surface, and volume effects on strength and fatigue size-scaling
(3) changes in failure mechanism as a function of temperature;
(4) the nature of slow crack growth; and
(5) what role residual stresses may have in these processes.

Lastly, numerical probabilistic models (i.e., life prediction codes) will be used in conjunction with the generated strength and fatigue data to predict the failure probability and reliability of complex-shaped components subjected to mechanical loading, such as a silicon nitride diesel engine valve. The predicted results will then be compared to actual component performance measured experimentally or from field service data. As a consequence of these efforts, the data generated in this program will not only provide a critically needed base for component utilization in internal combustion engines, but will also facilitate the maturation of candidate ceramic materials and a design algorithm for ceramic components subjected to mechanical loading in general.

Technical Highlights

Silicon nitride and TiAl exhaust valves

The 100-h field test, using Caterpillar G3406 (in-line 6 cylinders) nature gas engine, for both silicon nitride and TiAl exhaust valve has been successfully accomplished during this reporting period. The metallic valves currently employed in the engine were also included for reference. Following engine testing visual and optical examinations were carried out to inspect the tested valves for any apparent surface damages (chipping and cracking). Figure 1 shows the typical surface features for silicon nitride and TiAl exhaust valve after engine test. Similar features were also observed for the silicon nitride intake valves as well. A Taylor-Hobson surface profiling system (Model # Form Talysurf 120) was then employed to measurement the surface roughness (and thus degree of wear) of these tested valves. Three sections; i.e., upper valve guide, lower valve guide, and valve seat insert contact region, were evaluated, and three scans at each location were taken at 0, 120, and 240°, respectively. Results showed that there was a significant increase (1.5-5 folds) in roughness (Ra values) in the valve seat region for both silicon nitride and TiAl valves. As for the valve guide region, the silicon nitride exhaust valves showed a decrease in Ra values (roughness) due to the polishing effect, while the intake valves exhibited a minimum increase in Ra value. On the other hand, the TiAl exhaust valves showed a much more increase in Ra value (2-10 folds) as compared to the silicon nitride valves. The effect of the surface roughness introduced on the mechanical performance will be evaluated via destructive test after the 500h engine test.

TiAl intermetallic alloys

Studies of long-term creep behavior of TiAl alloys manufactured by Daido and Howmet were continued during this reporting period. Two types of TiAl cylindrical creep specimens different in final densification process (i.e., one is HIP and the other one is Non-HIP) manufactured by Daido, Tokyo, Japan were received from end user. Also, TiAl tensile specimens manufactured by Howmet, Michigan, USA were also received for evaluation. The test conditions specified are relevant to the temperature and stress profile encountered by TiAl turbo wheel under the application environments based on the FEA modeling. The database generated will then be used for verification of probabilistic life prediction of turbo wheel under engine operation conditions by the end users, and also could provide feedback to material suppliers for process modification to further improve mechanical properties. Figure 2-4 show the creep strain versus time curves of Daido HIP TiAl material tested at 650, 700, and 750°C under selected applied stress levels, while Figure 5 shows the preliminary creep curve for Howmet TiAl specimen tested at 750°C/240MPa. Preliminary creep results showed that the Daido HIP TiAl material exhibited low creep rates at 650°C, but exhibited much higher creep rates (at least one-order of magnitude increase) at temperatures ≥ 700°C, indicative a change in creep controlling mechanisms. Also, results at 750°C showed that the Daido HIP TiAl exhibited better creep resistance (about 4-fold) than Howmet TiAl under the same stress level. More creep tests will be carried out under various defined test condition to confirm the observation. In addition, creep tests as a function of applied stress level and test temperature would be performed, which would allow one to understand the creep controlling mechanisms as well as the activation energy for the process.

Studies of dynamic scratch test using a single-grit pendulum (rotational) scratch technique were carried out during this reporting period. The objective of this study was to provide insight into the dynamic abrasion of TiAl alloys in sliding contact. TiAl alloys evaluated include Daido HIP

and non-HIP TiAl, and Howmet TiAl material, which exhibit differences in grain domain and lamellar size, and thus could lead to difference in mechanical and wear response. Figure 6 shows the typical scratch surface feature of Daido HIP and Howmet TiAl alloy. The groove surfaces of scratches of two TiAls appeared to have maintained a certain degree of integrity with clear surface contours, which is distinctly different from scratches on brittle materials (where the side ridges were not preserved due to the lateral cracks). The side ridges are developed on banks with appreciable pile-up, especially over the wide middle region of the scratch that corresponds to the suppressed wear rate (as discussed in the following). Frequent fractures take place in the transverse direction over the middle region of the scratch, some of which are sizable and run into the bottom of the groove. For the Daido TiAl, no shallow lateral fractures were developed that are observed to occur in pure titanium. However, the lateral fractures were developed for the Howmet TiAl on the sides of the scratch as a result of cleavage; thus the material removal has been enhanced with a predicted high wear rate. Analysis of the tribological properties characterized by instantaneous specific energy and scratch hardness as related to the depth of the groove is currently in progress. Results will be discussed in the next quarterly report.

Status of Milestones

Milestone: "Complete mechanical testing and analysis of prototype silicon nitride and TiAl valves after natural gas engine field test." On schedule.

Communications / Visitors / Travel

Teleconferences with Jeremy Trethewey at Caterpillar, and Michael Kass and Tim Theiss at NTRC on the updated status of surface measurement for the 100-h tested Si_3N_4 and TiAl exhaust valves.

Communications with Jeremy Trethewey and Nan Yang at Caterpillar on the update of tensile creep tests for TiAl materials, and also discussions of the mechanical testing plans for FY2007.

Communications with Jeremy Trethewey and Nan Yang at Caterpillar on the update of dynamic scratch tests on both Daido HIP and Howmet TiAl alloy.

Problems Encountered

None

Publications

None

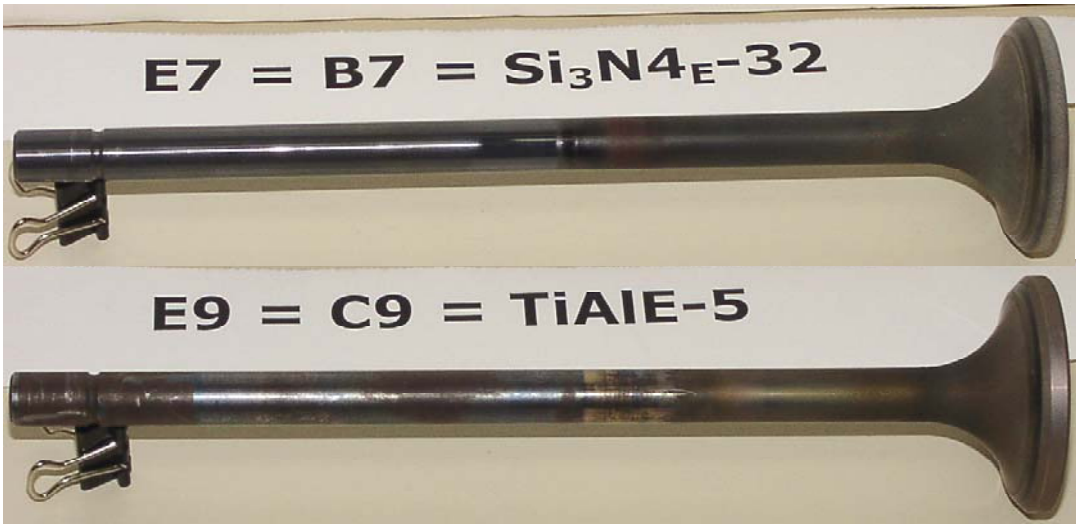

Figure 1. Photo showing the silicon nitride and TiAl exhaust valve after 100-h engine test.

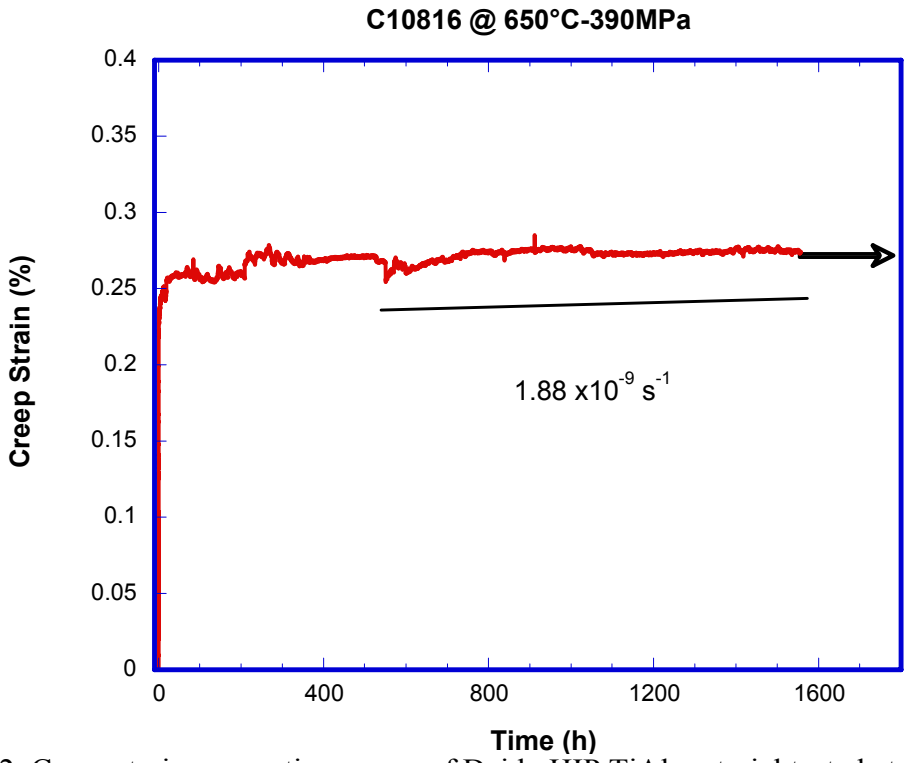

Figure 2. Creep strain versus time curve of Daido HIP TiAl material tested at 650°C and 390 MPa in air.

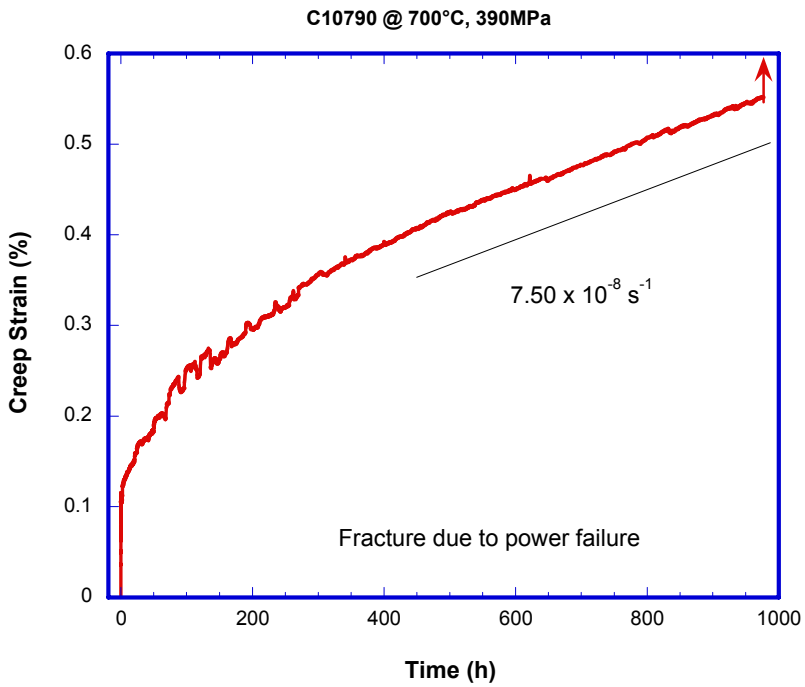

Figure 3. Creep strain versus time curve of Daido HIP TiAl material tested at 700°C and 390 MPa in air.

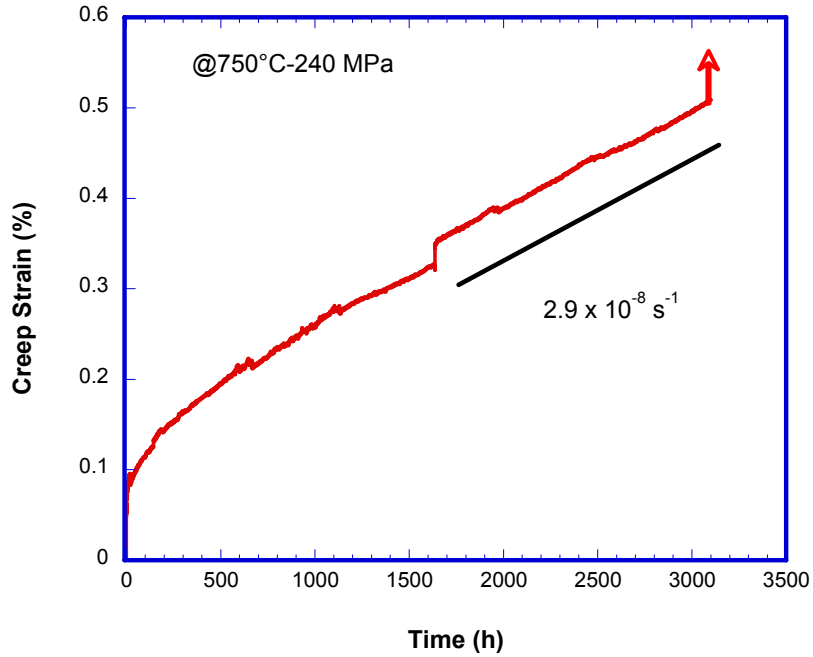

Figure 4. Creep strain versus time curve of Daido HIP TiAl material tested at 750°C and 390 MPa in air. The specimen fractured after ~ 3100-h test.

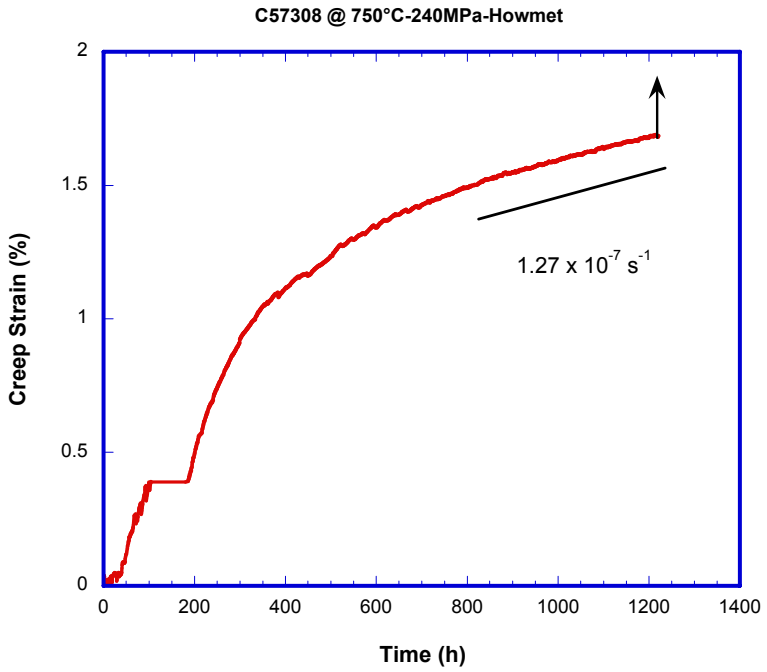

Figure 5. Creep strain versus time curve of Howmet TiAl material tested at 750°C and 240 MPa in air.

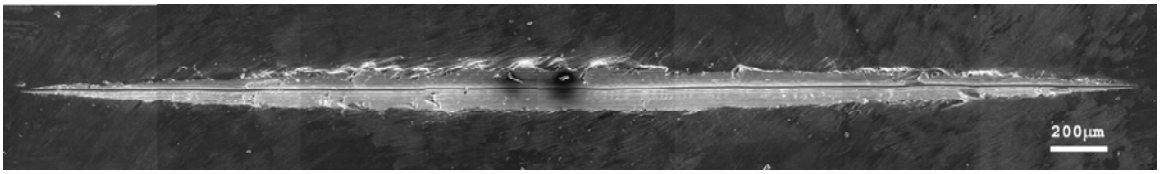

(a)

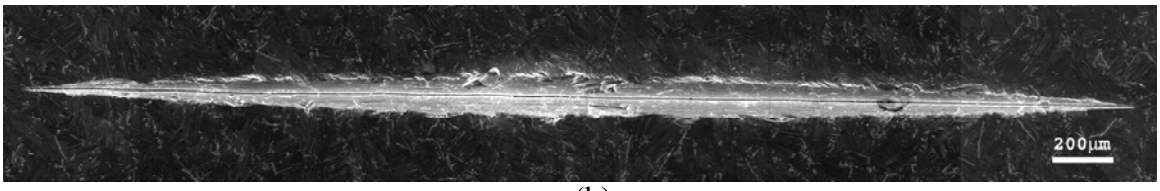

(b)

Fig. 6. SEM micrographs show typical scratch feature on: (a) Daido TiAl HIP and (b) Howmet TiAl. Scratch ran from left to right. The micrographs were taken after chemical etching

Lightweight Valve Train Materials

Jeremy S. Trethewey
Caterpillar Inc.

Introduction

Valve train components in heavy-duty engines operate under high stresses and temperatures, and in severe corrosive environments. In contrast, the valve train components in the light-duty engine market require cost-effective reliable materials that are wear resistant and lightweight in order to achieve high power density. For both engine classes, better valve train materials need to be identified to meet market demand for high reliability and improved performance, while providing the consumer lower operating costs.

Advanced ceramics and emerging intermetallic materials are highly corrosion and oxidation resistant, and possess high strength and hardness at elevated temperatures. These properties are expected to allow higher engine operating temperatures, lower wear, and enhanced reliability. In addition, the lighter weight of these materials (about 1/3 of production alloys) will lead to lower reciprocating valve train mass that could improve fuel efficiency. This research and development program is an in-depth investigation of the potential for use of these materials in heavy-duty engine environments.

The overall valve train effort will provide the materials, design, manufacturing, and economic information necessary to bring these new materials and technologies to commercial realization. With this information, component designs will be optimized using computer-based lifetime prediction models, and validated in rig bench tests and short-and long-term engine tests.

Program Overview

Information presented in this report is based on previous proprietary research conducted under Cooperative Agreement DE-FC05-97OR22579.

Ceramic Materials

Silicon nitride (Si_3N_4) materials have been targeted for valve train materials in automotive and diesel industries since the early 1980's. Some silicon nitride material grades have reached a mature level of materials processing, capable of being implemented into production. Commercial realizations have been reported in both automotive and diesel valve trains, with large-scale production underway. The silicon nitride valve train components in production are used in high rolling contact stress applications and have exhibited superior wear resistance and longevity.

Intermetallic Materials

Titanium aluminide (TiAl) based intermetallics retain their strength at elevated temperatures and are highly corrosion-resistant. They are lightweight and possess high fracture toughness. These alloys are actively being investigated for several aerospace and automotive applications.

Summary
The primary focus of this quarter is the execution of a valve durability test on a Caterpillar natural gas G3406 genset. During the last quarter (Jan-Mar 2006), Caterpillar and NTRC (National Transportation Research Center) representatives oversaw the installation of 10 Si_3N_4 and 4 TiAl valves at the regional Caterpillar dealer. In the current quarter, the first 500 hours of engine exposure has been achieved. The table below (Table 1) outlines the progress of this engine durability test.

Table 1: Engine durability test progress

Phase	Action	Status
Initial Installation	Valve Installation	Completed in March
Phase #1 (0 h – 100 h)	Engine Exposure	Completed in May
	Post-test Analysis	Completed in June
Phase #2 (100 h – 500 h)	Engine Exposure	Completed in July
	Post-test Analysis	Pending engine tear-down
Phase #3 (500 h – 1000 h)	Engine Exposure	Not yet started
	Post-test Analysis	Not yet started

This quarterly report will document the preliminary observations noted during Phase #1 and will discuss the expected results from the remainder of the test.

Engine operating conditions
The valves were installed in the following arrangement (Table 2) to ensure that the performance of the Si_3N_4 and TiAl valves could be isolated during post-test analysis.

Table 2: Valve installation arrangement

Cylinder	Intake	Exhaust
1	Silicon Nitride	Silicon Nitride
2	Silicon Nitride	Silicon Nitride
3	Silicon Nitride	Titanium Aluminide
4	Production Steel	Titanium Aluminide
5	Production Steel	Production Steel
6	Production Steel	Production Steel

Within the first few hours of engine operation, cylinder 1, outfitted exclusively with Si_3N_4 valves, began to exhibit the signs of knocking. This pre-ignition condition is a symptom of altered combustion dynamics and is most likely caused by the protrusion of the seated valve ~1.5 mm farther into the combustion chamber than originally designed. This protrusion may cause pre-ignition because it changes the compression ratio and provokes autoignition prior to spark-controlled ignition. It is also possible that local hotspots are generated on the valve face due to the increased thermal mass in the hottest region of the combustion chamber. This hotspot formation, a potential cause of pre-ignition, is exacerbated by the protruding portion of the valve head. Because this portion of the valve head does not contact the valve seat, there is no direct path for thermal conductivity and the local material temperature increases. It is important to note that this protrusion is an artifact of the valve geometry re-design and is correctable in future

valve design iterations. To circumvent knocking, an exceedingly harsh operating environment, the genset has been derated from 235 kW to 125 kW for the remainder of the test.

Valve Inspection – Visual & Profilometry

In a heavy duty engine, the first 100 hours of service time is considered the "break-in" period. During this initial phase the valve and seat insert conform to each other by a scuffing wear mechanism. Valve/guide contact may also cause wear on the stem while valve/bridge contact may cause wear on the stem tip. After 100 hours, the Si_3N_4 and TiAl valves showed minimal stem tip wear, acceptable valve/guide wear, and significant seat/insert wear. Figures 1a-1c show a representative Si_3N_4 exhaust valve (Si3N4E-32) after the first 100 hours of testing. As expected, there is an even coating of combustion byproduct on the valve's head face, fillet and lower valve stem regions. The stem wear is evident in the discoloration ending halfway up the valve. Figure 1d shows the wear profile of the valve seat region. Figures 2a-2d show the same results for a representative TiAl valve (TiAl-5).

In addition to wear scar depth, surface roughness, or R_A, also allows direct comparison of worn contact regions. Table 3 displays the surface roughness of each Si_3N_4 and TiAl valve before and after the first 100 hours of engine exposure.

Table 3: Surface roughness measurement of Si_3N_4 and TiAl valves at 0 h and 100 h

	Valve ID #	Valve Location	Time (hrs)	Valve Guide (R_A)		Valve Seat (R_A)
Si3N4 Intake	Si3N4I-20	I2-SI3N4	0	0.067		0.152
			100	0.095		0.226
	Si3N4I-21	I4-SI3N4	0	0.061		0.15
			100	0.079		0.779
	Si3N4I-25	I6-SI3N4	0	0.069		0.143
			100	0.069		0.199
	Si3N4I-28	I8-SI3N4	0	0.063		0.178
			100	0.093		0.435
	Si3N4I-33	I10-SI3N4	0	0.067		0.174
			100	0.089		0.185
	Si3N4I-41	I12-SI3N4	0	0.069		0.174
			100	0.096		0.394
Si3N4 Exhaust	Si3N4E-11	E1-SI3N4	0	0.063		0.232
			100	0.059		0.436
	Si3N4E-17	E3-SI3N4	0	0.06		0.211
			100	0.027		0.888
	Si3N4E-9	E5-SI3N4	0	0.063		0.222
			100	0.037		0.382
	Si3N4E-32	E7-SI3N4	0	0.066		0.206
			100	0.034		0.389
				Ti	TiAl	
TiAl Exhaust	TiAl-5	E9-TiAl	0	0.121	0.121	0.187
			100	0.239	0.316	0.970
	TiAl-6	E11-TiAl	0	0.102	0.102	0.221
			100	0.316	1.054	1.157
	TiAl-7	E13-TiAl	0	0.121	0.121	0.211
			100	0.269	0.661	0.762
	TiAl-8	E15-TiAl	0	0.12	0.12	0.226
			100	0.318	1.097	1.143

Several preliminary conclusions may be drawn from these photographs, profilometry scans and surface roughness measurements.

- **Valve/seat wear:** The 2x increase in valve/seat surface roughness for Si3N4E-32 is evidence of break-in scuffing wear on the Si_3N_4 valve. Figure 1d shows a relatively constant wear scar depth of ~2µm. However, the 5x increase in valve/seat surface roughness for TiAl-5 is an indication that wear has exceeded standard break-in levels. This is confirmed by Figure 2d which shows that the valve/seat wear scar depth is

~15 μm, a significant magnitude for 100 hours of engine exposure. This accelerated wear in the valve/seat region of the TiAl valve suggests that an optimized wear-resistant surface treatment may be necessary to ensure acceptable wear behavior. When the 500 hour and 1000 hour wear data has been captured firm conclusions will be drawn from these observations.

- **Valve/guide wear:** The surface roughness data suggests that minor scuffing wear moderately increases the R_A of the Si_3N_4 intake valves. In contrast, the R_A of the Si_3N_4 exhaust valves decreases because the higher stem temperature enables the stem/guide to undergo a polishing wear mode. The TiAl valves exhibit inferior wear performance compared to the Si_3N_4 valves in the valve/guide region. However, the 2x-3x R_A increase in the Ti-6-4 segment of the stem indicates that the thermal oxidation heat treatment was more effective on the Ti-6-4 than on the TiAl, which showed a 3x-10x R_A increase.
- **Valve integrity:** Although the wear mechanisms and rates must be better understood before Si_3N_4 and TiAl can be successfully implemented into production, the fact that these valves have survived 500 hours of service is an indication that these valve materials may be capable of withstanding a heavy duty engine environment.

Valve Inspection – Laser Scatter NDE

At the end of the first 100 hour "break-in" test phase each valve was scanned with the laser-based NDE (Non-Destructive Evaluation) instrument outlined in the project titled "NDE of Diesel Engine Components." Figure 3 shows the NDE scans for exhaust valves Si3N4E-32 and TiAl-5 (the same valves in Figures 1 and 2). In general, these valves scans are similar to the pre-test scans with a couple of exceptions. The region of interest in these images is the valve seat band, the location of highest accumulated damage. The white stripes above and below the valve seat band are most likely caused by the combustion byproduct and are not significant flaws. The continuous grayscale transition in the Si_3N_4 valve seat band (Figure 3a insert) confirms that there is no notable surface damage in its valve/seat wear region. However, the valve seat band in the TiAl valve (Figure 3b insert) shows a significant level of surface damage. More detail may be found regarding NDE data interpretation in Dr. JG Sun's Apr-Jun 2006 quarterly report.

Next Steps

Since Phase #2 (to 500 total engine hours) has recently been completed, the next immediate task is to extract the valves from the engine and subject each valve to the same post-test analysis as reported above. The condition of the valves after 500 hours of engine exposure will provide valuable material durability data. When the Phase #2 post-test analysis is complete, 2/3 of the valves will be re-installed in the engine while the remaining 1/3 will be replaced by fresh valves and reserved for destructive testing. After the engine has run for another 500 hours, all valves will be removed, inspected, and prepared for destructive testing. By performing fast fracture tests on valves that have accumulated 0, 500, and 1000 hours of engine time, the effect of engine aging on the materials' retained strength will be examined. Along with combustion dynamics and fuel consumption measurements, this data will enable the team to quantify performance gains and establish useful life estimates of Si_3N_4 and TiAl valves in a heavy duty engine environment.

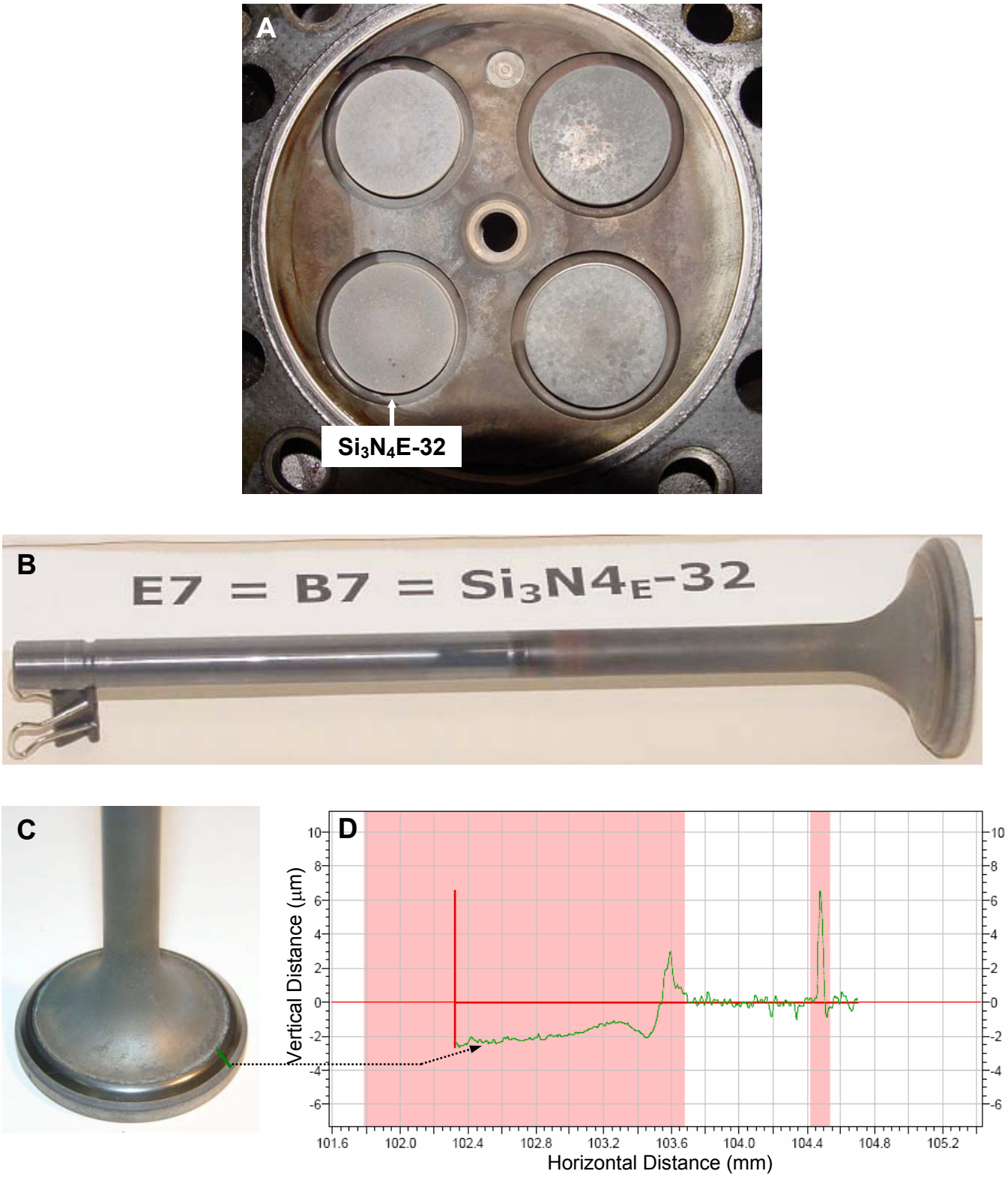

Figure 1: (A) An image of Cylinder 'B' immediately after the completion of the first 100 hour break-in phase. (B,C) Valve Si3N4E-32, a representative Si_3N_4 exhaust valve. (D) Profilometry scan of the valve/seat wear scar showing a wear scar depth of ~2 µm.

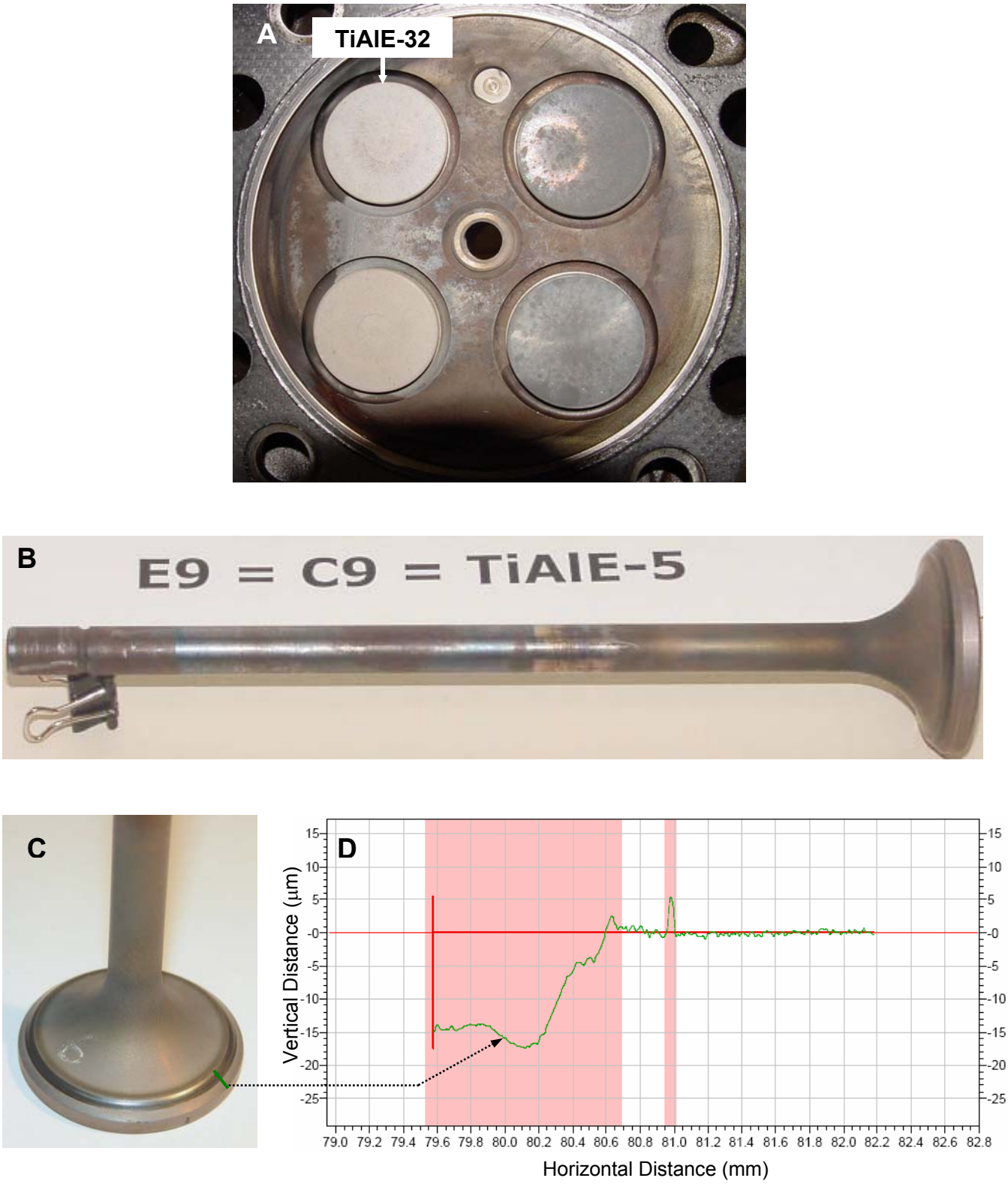

Figure 2: (A) An image of Cylinder 'C' immediately after the completion of the first 100 hour break-in phase. (B,C) Valve TiAl-5, a representative TiAl exhaust valve. (D) Profilometry scan of the valve/seat wear scar showing a wear scar depth of ~15 µm.

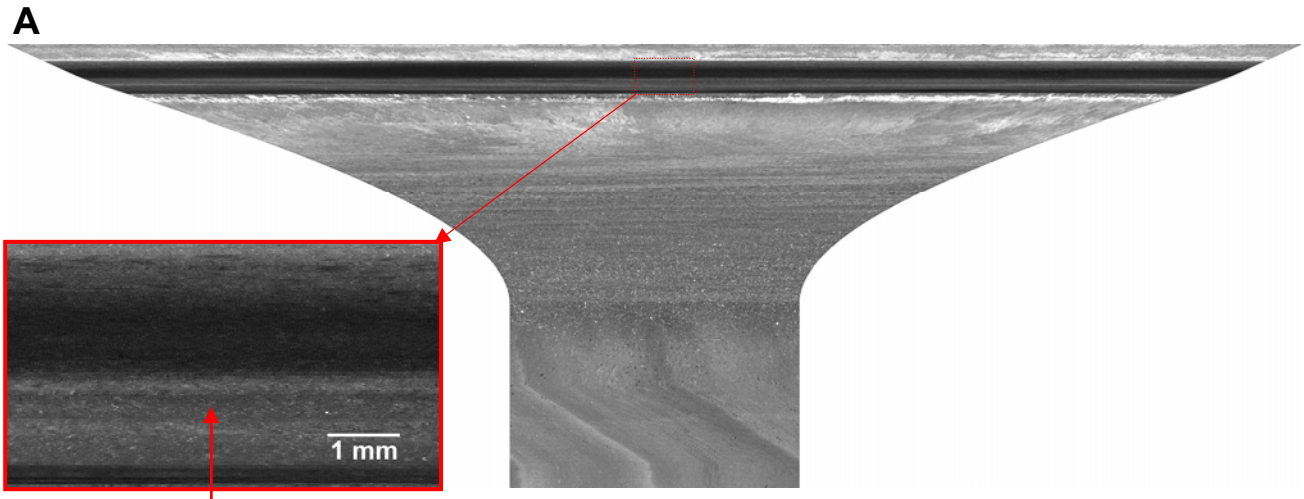

No discontinuities = No significant damage

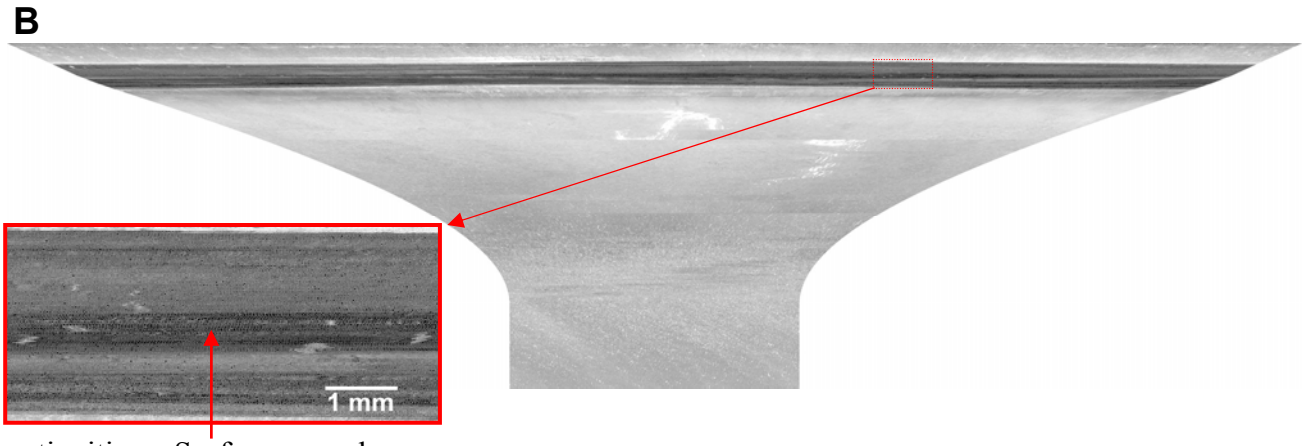

Discontinuities = Surface wear damage

Figure 3: Laser-based NDE scans of (A) Si3N4E-32 and (B) TiAl-5 indicating that the Si_3N_4 valve has not sustained major wear damage, but the TiAl valve is showing signs of significant valve/seat wear.

An Integrated Surface Modification of Engineering Materials for Heavy Vehicle Applications

Stephen Hsu, Huan Zhang, Yanan Liang, Jing Yang, and Wei Li
National Institute of Standards and Technology

Objectives

- Develop design guidelines for surface texturing features that can reduce friction and enhanced durability for heavy duty diesel engine components.
- Develop theory and models to understand the friction reduction mechanism to provide next generation of surface texture design principles.
- Develop cost-effective fabrication techniques for textural features
- Develop appropriate thin films and coatings to achieve synergistic and complementary relationship with texturing to enhance performance.
- Discover and develop surface chemistry for texture protection and improve friction reduction

Approach

- Determine the effect of size, shape, pitch, and patterns of surface textural features on friction under 1) high speed, low load regime; 2) high load, high speed regime; 3) high load, low speed regime.
- Develop cost effective fabrication technologies for creating surface textural features on various metal surfaces.
- Develop test methodology to measure the effects of the textures on friction
- Develop an integrated system approach to combine thin films, surface textures, and lubricant chemistry for synergistic friction reduction.
- Organize and conduct international cooperative research activities under the auspice of the International Energy Agency (IEA) to leverage the research capabilities worldwide.

Accomplishments in this quarter

- We continue our approach of simultaneous theoretical modeling and experimental research in the high load, low speed contact conditions. We are trying to determine the friction reduction mechanisms in this regime.
- The IEA IA-AMT Executive Committee was successfully held in Calgary, Canada on May 7, 2006 with delegates from Canada, US, and Germany. China, UK, and Australia were unable to attend due to last minute logistic issues and visa requirements.
- I attended the IEA CERT meeting on June 15-16, 2006 to present the detailed strategic plans of the IEA Implementing Agreement on Advanced Materials for Transportation. CERT approved a three year extension for the implementing agreement.

Introduction

Frictional losses are inherent in most practical mechanical systems. The ability to control friction offers many opportunities to achieve energy conservation. Over the years, materials, lubricants, and surface modifications have been used to reduce friction in automotive and diesel engines. However, in recent years, progress in friction reduction technology has slowed because many of the inefficiency have been eliminated. A new avenue is needed.

Designing surfaces specifically for friction reduction with concomitant enhanced durability for various engine components has emerged recently as a viable opportunity due to advances in fabrication and surface finishing techniques. Recently, laser ablated dimples on surfaces have shown friction reduction properties and have been demonstrated successfully in conformal contacts such as seals where the speed is high and the load is low. The friction reduction mechanism in this regime appears to depend on the size, patterns, and density of dimples in the contact.

The objective of this project is to develop an application specific engineered surface (combining surface textures, thin films, surface chemistry) tailored for the optimum friction reduction and enhanced durability.

This friction reduction technology is aimed at various energy transmission components in an engine, particularly in a heavy duty diesel engine. Components such as cylinder liner ring contacts, cam and lifters, and overhead bearing components are being targeted. To meet the durability criteria, the texture patterns have to be protected by thin films/coatings and appropriate lubricating chemistry over a broad range of operating conditions. The final outcome of the project will be a general design principle and guidelines for various engine components under a wide range of operating conditions. To achieve the maximum energy conservation, the technology is being shared through an international cooperative research under the International Energy Agency Implementing Agreement on Advanced Materials for Transportation (IEA IA-AMT). The organization effort under the IEA activities involves getting new countries to join, and UK, China, Australia, Finland, Sweden, Israel, and Japan have agreed to participate under the IEA Annex IV on surface technology.

Approach

From energy conservation point of view, most parasitic losses in engines take place under high load and medium to low speed conditions. Therefore, we need to extend the surface texturing designs from high speed low load conditions to low speed high load conditions. However, when we ran the same surface texture patterns under boundary lubrication conditions, friction actually increased. A collaborative effort with Northwestern University using a sophisticated elastohydrodynamic friction model confirmed our experimental observations. Basically, under boundary lubricated conditions (high load low speed), the edge stresses around the dimple increase frictional losses as if the surface is much rougher. So there is a trade-off in this regime.

We are the first group in the world succeeded in achieving significant friction reduction under high load low speed conditions. Since this is an explored area and there is no existing literature, we have to develop the fundamental theory and practice from scratch. Therefore the approach we are taking is to engage in simultaneous theoretically modeling and experimentations to advance our understanding and subsequently use the understanding to further our development of new texture patterns and features to achieve friction reductions.

Technical Highlight

Previously, we have succeeded in achieving significant friction reduction (40%) under high load (2-3 GPa asperity contact pressures), low speed conditions (0.2 m/s-1.3 m/s) in a bearing steel on bearing steel system. We have examined the issue of the bearing L/D ratio in terms of orientation

and various depth-to-length ratios. We found that the converging geometry in the direction of sliding provided the best friction reduction.

L/D ratio and size effects

One of the critical issues in fabricating the new surface features was the effect of the slope at the bottom of the feature. In bearing applications, this typically was called the L/D ratio (bearing length over radius of the bearing) to estimate the hydrodynamic lift force. We used this concept to apply to our surface texture design. Another important factor was the size of the surface feature over the contact area. In boundary lubrication conditions, since the edges of the surface features served as rough spots increasing the friction, therefore, the optimum number of the features might be much smaller than the high speed low load regime. We fabricate several surface features by varying the L/D ratio and the size of the surface features. Results showed that the classical wedge orientation has the highest friction reduction capacity, reducing the average friction coefficient of the untextured from 0.09 to about 0.05, a 44% decrease in a 52100 bearing steel on 52100 bearing steel contact. We varied the size of dimple, area coverage, and depth to seek the optimum combination of parameters to effect friction reduction under increasingly severe contact conditions. A series of samples were prepared to using the high-load tribotester to precisely fabricate these surface dimple features for testing. Based on the theoretical analysis results, we decided to determine the relationship between depth of the feature and load, and the effect of area density under high load conditions.

Under high load contact, plastic deformation and wear will occur. As the load begins to increase, edge stresses and deformation induced frictional resistance become more significant and our analysis last quarter confirmed this hypothesis. In order to consistently design surface features effective at increasingly higher contact pressures, it is important to understand the friction reduction mechanisms under such conditions.

We designed our experiments by fabricating dimples with approximately the same L/D ratios and systematically decreased the size of the dimples, thereby increased the area density. The dimpled surfaces were then subjected to friction testing in a modified ball on three plates contact geometry in a four ball wear tester. Loads of 5 kg, 10, 20, 30 kg were used (corresponding to apparent contact pressures of 86MPa, 168MPa, 337MPa, and 470MPa respectively). Each experiment was conducted using a speed-step change from high speed to low speed (1.34 m/s to 0.19 m/s). Table 1 shows the details of the designed surface features.

Table 1. Surface feature dimensions and area densities

	Dimple length µm	L/d		Area ratio %		Dimple # / contact area	Shape
		Target	Actual	Target	Actual		
C1-200	10	8	10	7	6.4	430	
C2-400	15	8	10	7	6.8	206	
C4-800	22	8	9	7	7.1	106	
C2-400-2	15	8	10	3.5	3.4	106	

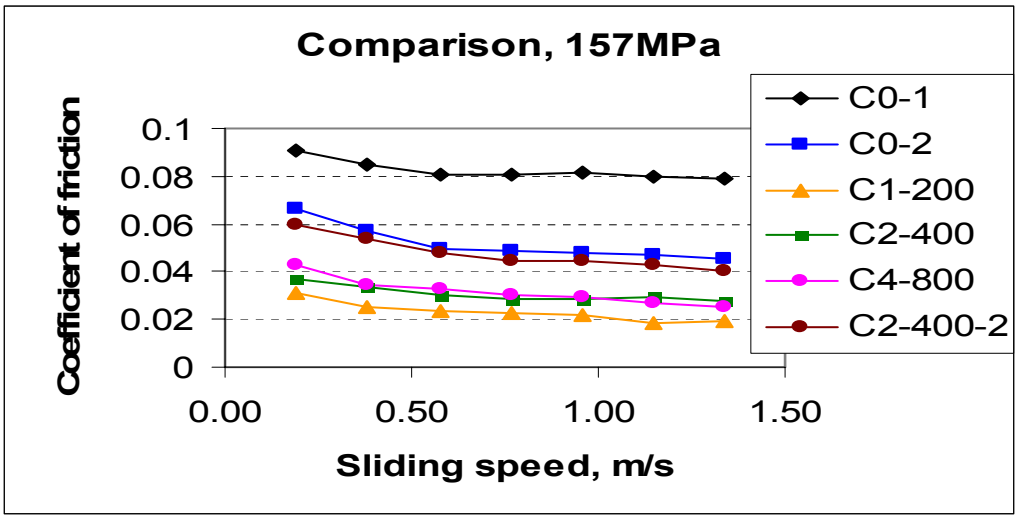

Figure 1. Frictional reduction achieved under 10kg load

Results are shown in Fig. 1. As can be seen, at 10 kg load (apparent contact pressure of 157 MPa, asperity contact stresses at 1-2 GPa, C2-400-2 has the lowest friction coefficient, about 75% reduction from the untextured surface, C0-1. The untextured surface has a coefficient of friction from 0.11 to 0.09 which are typical boundary lubrication frictional values. Yet as we introduce the dimples, the friction values decrease to 0.02 which is typical of hydrodynamic lubrication. Worn surface topography shows wear and deformation as a result of the contact severity under this condition. As the contact severity increases, the number of dimples required for friction control decreases, as predicted by our model analysis last quarter for increasing the edges stresses (the surface effectively becomes rougher). In this experimental design, larger sizes appear to be beneficial under high loading condition. This needs to be confirmed next quarter.

Figure 2 shows the surface damage for the untextured surface as compared to the C2-400-2 textured case. As it can be seen, the untextured surface under identical conditions suffers severe damage while the textured surface shows very little wear and deformation.

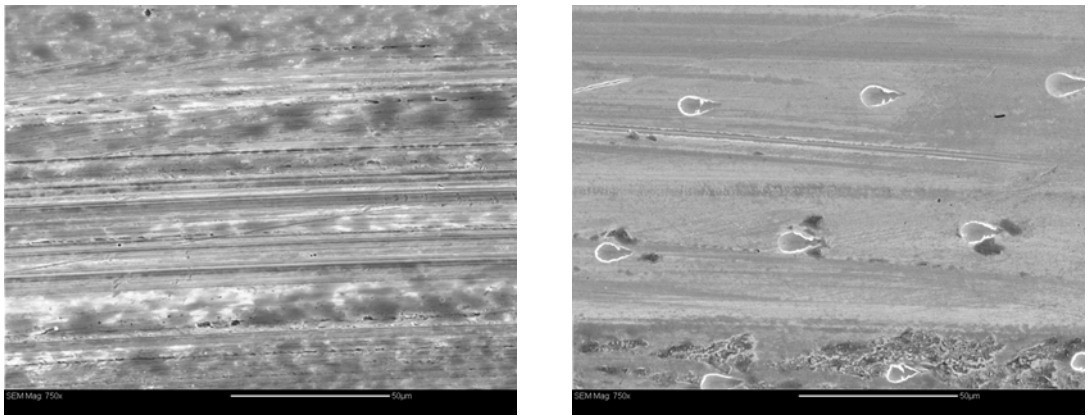

Fig. 2. Comparison of surface damage between untextured surface vs. textured surface for C2-400-2 case

Theoretical Modeling -
Contact Simulation for the Estimation of Sealing Pressure

For a dimple fabricated on a surface, the edge sealing pressure can be used to characterize its load carrying capacity during lubricated sliding contact. Contact simulation is conducted for a typical surface cell with a single dimple to estimate the sealing pressure. The results are obtained for different texture patterns under different load, and are further correlated to the friction measurement.

Consider rectangular surface cells, each of which contains a dimple at the center. From a normal perspective, a dimple can be assumed to be composed of two half ellipses. The size of dimple and surface cells are determined for four texture patterns described in previous sections. For this case, the nominal ball-disc contact pressure and radius can be calculated from the following Hertzian solution:

$$\overline{p} = \frac{2}{3}\left(\frac{6W_e E^{*2}}{\pi^3 R_e^2}\right)^{1/3} \qquad (1a)$$

$$a = \left(\frac{3W_e R_e}{4E^*}\right)^{1/3} \qquad (1b)$$

The effective radius is then given by

$$\frac{1}{R_e} = \frac{1}{R_b} - \frac{1}{R_c} \qquad (2)$$

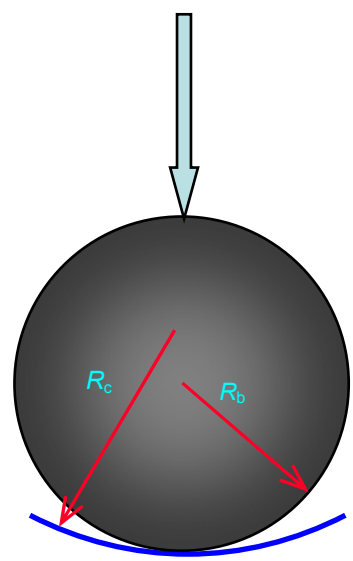

Figure 3. Illustration of the contact between the standard ball and the disc with a worn scar.

where W_e is the load applied to each disc, E^* is the reduced elastic modulus, and R_e is the effective sphere radius. As illustrated by Fig. 3, the contact takes place at the worn scar on the disc.

where R_c is the radius of curvature of the worn scar, which is estimated so that the radius of contact under the highest load calculated from Eq. (1b) is almost the same as that measured from the worn scar after test. The estimation leads to the following relation: $R_c = 1.25R_b$, based on which the nominal contact solution is obtained for each level of load.

With the nominal contact radius determined, the dimple size and that of a surface cell can be calculated for each texture pattern. In addition, the average and maximum load carried by individual surface cells are determined accordingly.

The contact solution is obtained with the material properties specified below. In the tests, 1/2" AISI E-52100 steel balls were used and its hardness is Rockwell C 64-66. The disc is made of hardened 52100 steel with a hardness of Rockwell C60. Their elastic modulus is taken to be $E = 2.10\times10^{11}$Pa and the corresponding reduced elastic modulus is $E^* = 1.1538\times10^{11}$Pa. A more detailed description of the dimple geometry is needed to fully define the topography of the surface cell. By assuming that each cross-section consists of two cosine or sine curves, the following equations are obtained to determine the surface height at a location along the centerline cross sections of the dimple:

$$z = d[\cos(\pi x_1/l_1) - 1]/2 \text{ for } 0 < x_1 < l_1 \text{ and } y = 0 \quad (3a)$$

$$z = d[\cos(\pi + \pi x_2/l_2) - 1]/2 \text{ for } 0 < x_2 < l_2 \text{ and } y = 0 \quad (3b)$$

$$z = d[\cos(2\pi y/w) - 1]/2 \text{ for } 0 < y < w \text{ and } x_2 = 0 \quad (3c)$$

The surface equations for points along any other cross-section within the dimple are given by

$$z = d'[\cos(\pi x'_1/l'_1) - 1]/2 \text{ for } 0 < x'_1 < l'_1 \quad (4a)$$

$$z = d'[\cos(\pi + \pi x'_2/l'_2) - 1]/2 \text{ for } 0 < x'_2 < l'_2 \quad (4b)$$

where $l'_1 = l_1[1 - (2y'/w)^2]^{1/2}$, $l'_2 = l_2[1 - (2y'/w)^2]^{1/2}$, and $d' = d[1 - \cos(\pi - 2\pi y'/w)]/2$. Figures 4 and 5 illustrate the geometry of the two different types of cross-sections.

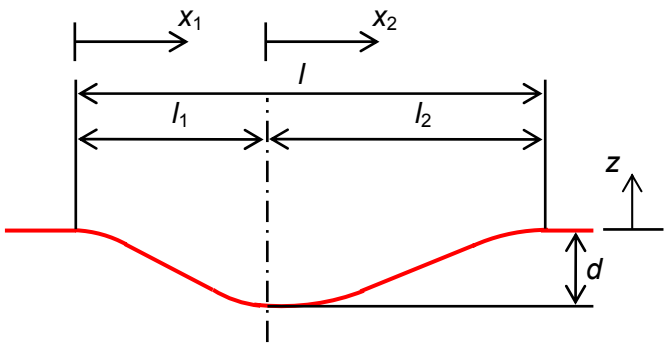

Figure 4 (a): front view

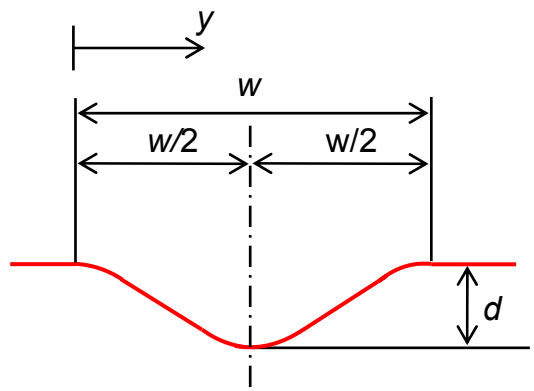

Figure 4 (b): side view

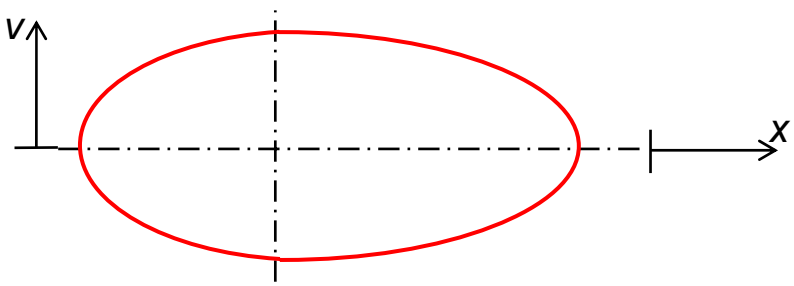

Figure 4 (c): top view

Figure 4. Centerline cross sections of the dimple.

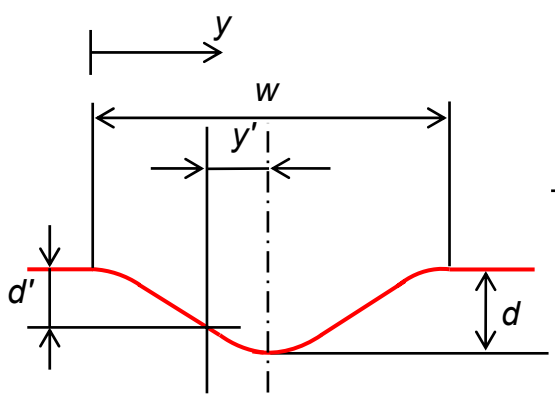

Figure 5 (b): side view

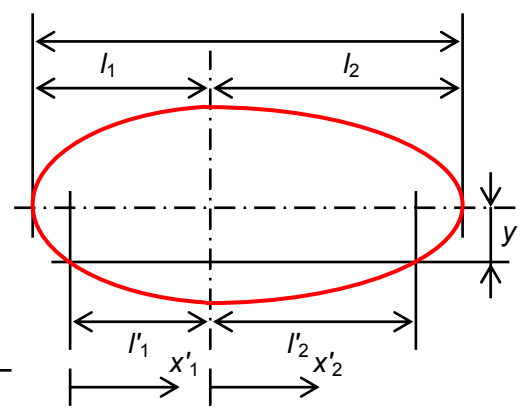

Figure 5 (a): top view

Figure 5. A cross section away from the centerline of the dimple.

With the geometry, load and material properties defined for the contact involving a surface cell with a single dimple, numerical contact models can now be used to determine the pressure distribution arising from contact by solving the following equations:

$$g_{ij} = h_{ij} + u_{ij} - u_0 \qquad \text{or} \qquad \mathbf{g} = \mathbf{h} + \mathbf{u} - u_0 \tag{5}$$

$$u_{ij} = \sum_l \sum_k K_{k'+i-k,\, l'+j-l} p_{kl} \qquad \text{or} \qquad \mathbf{u} = \mathbf{A}\mathbf{p} \tag{6}$$

$$\sum_i \sum_j p_{ij} = P_0 \qquad \text{or} \qquad \mathbf{q}^t\mathbf{p} = P_0 \tag{7}$$

where **h** is the gap between the surfaces just prior to any deformation, **u** is the composite surface displacement under the applied force F_0, **g** is the gap after the deformation, **p** is the interfacial pressure, u_0 is the rigid normal approach of one body to the other, P_0 is defined by $F_0 = \Delta x \Delta y P_0$, **q** is a vector of ones, and **A** is the influence coefficient matrix. The influence coefficient $K_{k'+i-k,\, l'+j-l}$ describes the relationship between the normal displacement at the center of an element and constant pressure over another element.

A computer program was written to solve the contact stresses around the dimple to estimate the sealing pressure containing the lubricant within the dimple. The solution is obtained on a regular grid with different grid sizes of 0.1, 0.2 and 0.4μm, respectively. Figure 6 shows a typical pressure distribution over a single dimple under high pressure contact. Due to the edge effects, the stress concentration is found around the dimple with a minimum at the leading edge, which may be used to estimate the minimum sealing pressure and correlated to the friction measurement.

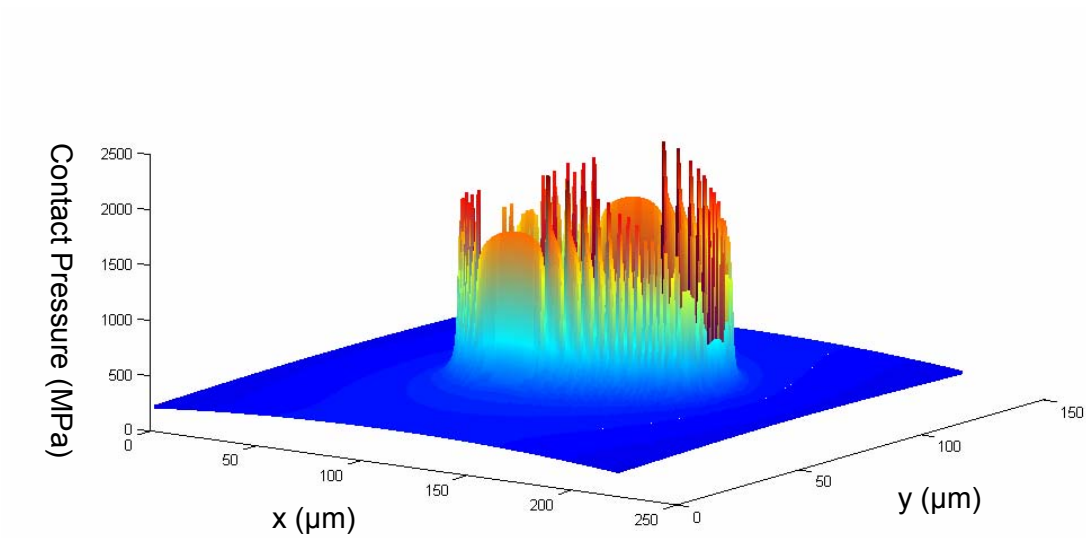

Figure 6. Typical contact pressure distribution of a surface dimple.

We thus estimated the sealing edge stresses for various cases and the results were correlated with the friction reduction under low load and high load range we studied. The rationale was if leakage and sealing pressure were an important factor for friction reduction under high load, low speed conditions, then the sealing pressure thus calculated would correlate with the friction reduction. Preliminary results from two cases, C2-400 and C4-800 appeared to correlate. Work

is continuing to calculate the sealing pressures for all four cases and will report the results next quarter.

Summary

Substantial progress has been made to understand the friction reduction mechanisms of surface textures under high load, low speed conditions. A theoretical model in determining the hydrostatic sealing pressure has been developed and initial correlation between friction reduction and sealing pressures appears to be promising.

Publications/Presentations

Presentations:

S. M. Hsu, "Integrated Surface Modification Technology: a progress report," COST 532 symposium on surface textures, Porto, Portugal, Oct. 12, 2005.

S. M. Hsu, "Design of surface textures for high load, low speed contact conditions," STLE annual meeting, Calgary, Canada, May 8-11, 2006.

S. M. Hsu, "Recent progress in IA-AMT and future plans," CERT meeting, IEA HQ, June 16, 2006, Paris, France.

Publications:

"Surface Texturing: Comparison of Various Geometric Shapes on Friction under High Speed Low Load Conditions," Wang, X., Hsu, S.M., published in the proceeding of the International Tribology Conference, Kobe, Japan, May 29-June 2, 2005

"Surface Texturing: A New Design Principle for Friction Reduction Under Boundary Lubrication Conditions," Wang, X., Hsu, S.M., published in the Proceedings of the International Tribology Conference, Kobe, Japan, May 29-June 2, 2005.

Collaborations:

A team from UK visited us to discuss collaborations on surface texturing

Coating Evaluation and Performance

M. J. Lance, A. A. Wereszczak, K. E. Johanns, and D. P. Ryan
Ceramic Science and Technology (CerSAT)
Oak Ridge National Laboratory

Objective/Scope

Next generation thermal barrier, tribological, and environmental barrier coatings will enable enhanced diesel engine performance, higher operating efficiency, longer engine lifetimes, and lower emission of NO_x and particulates. Unfortunately techniques for assessing properties, particularly with respect to coating interface, are unproven. The sought attributes (thermal protection, improved wear resistance, and environmental barrier) of any of these coating applications can only be realized if their architecture is appropriately designed to withstand operating or service stress states. This project explores new, innovative, and promising test and characterization techniques that crosscut all these coating systems and whose results and interpretations will expedite their development and exploitation in the heavy vehicle sector.

An attached section is provided at the end of this Quarterly Report of the Minutes from the Executive Committee (ExCo) meeting of International Energy Agency Implementing Agreement (IA-AMT) on Advanced Materials for Transportation (IA-AMT) that occurred during Quarter 3. One of this project's investigators (Wereszczak) has been responsible for maintaining the IA-AMT website (http://ia-amt.ornl.gov) and for fulfilling ExCo Secretarial responsibilities the last two quarters (including the recording of these Minutes).

Technical Highlights

Mechanical tests to measure adhesion or spallation resistance often revolve around a tensile test method where a pull rod is glued to the coating and loaded in tension until spallation is produced. The validity of the test is often dependent on the tester's ability to identify a suitable adhesive and to choose a specimen where end effects do not affect the results. Because polymeric adhesives are often used for room temperature tests, the ability to conduct tests at elevated temperatures is often inhibited.

Most thermal, environmental, and tribological coating materials have lower strains-to-failure (ε_f) than the substrate material they are bonded to. In recognition of this, a ball-on-ring biaxial flexure test method (Fig. 1) continued to be developed to quantify coating strain-to-failure. The technique also lends itself well to elevated temperature testing.

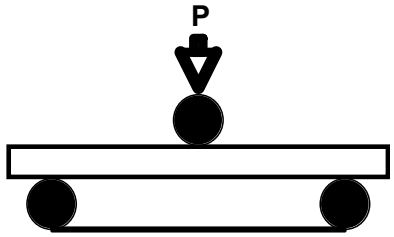

Figure 1. Side view and sectioned schematic of a ball-on-ring biaxial flexure configuration used to measure coating strain-to-failure.

A hard ball (e.g., WC or Si_3N_4) is contact-loaded on a specimen resting on a ring. Excessive deflection and induced plastic deformation of the specimen is actually sought. The specimen is deflected until spallation occurs, and the spall pattern or size is then linkable to a strain-to-failure. If the coating side is oriented on top in Fig. 1, then a gradually changing radius of curvature produces a tensile strain in the coating. Conversely, if the coating is oriented on the bottom in Fig. 1, then the coating is subjected to a tensile strain. Examples of tested coupons are shown in Fig. 2.

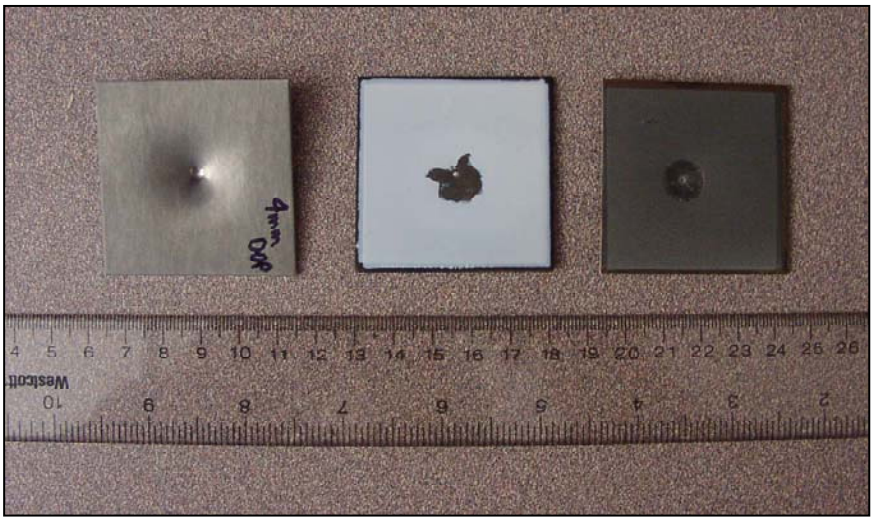

Figure 2. Ball-on-ring tested coupons. Uncoated 410SS (left) and coated specimens (middle and right).

The validity of the FEA of the produced ball-on-ring deflection continued during the present reporting period. Oxidized Aluchrome YHF alloy was initially chosen as the model substrate material; however, the oxidation treatment embrittled it and it consequentially fractured at too low strains-to-failure. Thin disks of PM2000 were instead prepared because its oxidation treatment requires lower temperatures and times at temperature, so it is believed that embrittlement effects will be lessened or eliminated. Their ball-on-ring testing will be performed during the fourth quarter. As described in the last quarterly report, the stress fields of the ball-on-ring deflected coated coupons will be quantified using optical fluorescence.

Status of FY 2006 Milestones

Survey innovative test techniques that facilitate the coating performance and evaluation of thermal and tribological coatings. [09/06] *On schedule.*

Communications/Visits/Travel

The traveler traveled to Calgary, Alberta, Canada to attend an Executive Committee of the International Energy Agency Implementing Agreement on Advanced Materials for Transportation. The meeting was held on 07 May 2006 at the TELUS Convention Center.

Publications
None.

References
None.

Minutes of the Executive Committee (ExCo) of the International Energy Agency (IEA) Implementing Agreement on Advanced Materials for Transportation (IA-AMT)

Meeting Date: Sunday, 07 May 2006
Time: 2:00 PM - 6:30 PM
Location: Room 101, TELUS Convention Centre, Calgary, Alberta, Canada

Attendees:

Name	**Organization**	**Email**
Oyelayo Ajayi	ANL, USA	ajayi@anl.gov
Stephen Hsu	NIST, USA	stephen.hsu@nist.gov
Tom Malis	NRCan-CANMET, CANADA	malis@nrcan.gc.ca
Rogelio Sullivan	USDOE, USA	rogelio.sullivan@ee.doe.gov
Rolf Wäsche	BAM, GERMANY	rolf.wasche@bam.de
Andy Wereszczak	ORNL, USA	wereszczakaa@ornl.gov
Wenyue Zheng	NRCan-CANMET, CANADA	wenyue@nrcan.gc.ca

The Chairman, Mr. Rogelio Sullivan, opened the meeting and welcomed the delegates. After a round of introduction, he gave a presentation outlining a brief history of the Implementing Agreement on Advanced Materials for Transportation (IA-AMT) and clarified the membership status of various countries. Current member countries to the IA-AMT are Belgium, Canada, Germany, Sweden, and the United States. Japan formally withdrew from the IA-AMT on January 31st, 2006. The Executive Committee last time (Oct. 2005 in Porto) unanimously decided to invite the following countries to join the IA-AMT: China, Australia, Finland, Portugal, and UK. He then went on to introduce the United States Department of Energy (USDOE) interests in transportation materials such as lightweight materials, fuel cell, hydrogen storage materials, and advanced materials used in heavy vehicle materials research.

Dr. Stephen Hsu discussed the meeting's agenda. The following items would be discussed: current IA-AMT membership, update of the Annex III on Rolling Contact Fatigue, and an update of the Annex IV on Surface Texture Technology. This would be followed by discussions on the proposed new Annexes: Coating Performance and Evaluation (Wereszczak), Nanomaterials (Malis and Hsu), and Lightweight Materials (Zheng). Resolutions to address the changes in the implementing agreements and proper languages to be used in inviting new countries would be voted upon.

Dr. Hsu discussed current IA-AMT membership in detail and the current status of the countries in getting government approval to join the IA-AMT. The present membership of the five countries and Japan's recent departure were reiterated. Dr. Hsu stated that he had been in dialog with technical delegates from China, the United Kingdom, Australia, Japan, Finland, Portugal, Korea, and Israel. China and the UK should be joining soon, Australia is waiting for the response from CSIRO, and that Finland has showed strong interest in joining the IA-AMT. In the case of Japan, NEDO has been the participating agency and has been heavily involved in advanced ceramics used in turbines and other energy generating technologies. NEDO decided to

withdraw from IA-AMT due to its conclusion of the ceramics program. AIST, Agency for Industrial Science and Technology, in Japan has been participating in Annex IV activity and is now exploring the possibility of joining IA-AMT on its own.

Dr. Andrew Wereszczak gave an overview of Annex III on Rolling Contact Fatigue (RCF). The attendees were informed that US involvement in this Annex beyond US Fiscal Year 2006 (30 September 2006) was uncertain due to sponsorship changes. The C-sphere flexure strength specimen was overviewed. It was described as a new test specimen to measure strength of ceramic spheres and effective at exploiting flaws in ceramic balls. BAM's Rolf Wäsche expressed interest in participating in a C-sphere flexure specimen round robin study should one ever be pursued.

Dr. Hsu presented an overview of Annex IV on Surface Texturing Technology. He described a variety of surface modification techniques that are being used by various participants to fabricate surface textures. He outlined specific tasks to be performed by the international participants on textured surface characterization, test methods to evaluate textured surfaces for friction reduction, and cooperative studies on how to predict textured surfaces. He also outlined some of the advances in texturing in friction reduction under high load, low speed conditions.

Dr. Wereszczak gave a presentation on a proposed new Annex entitled Coating Evaluation and Performance. He described some of the techniques being developed at ORNL including laser shock spall adherence testing, excessive bending via ball-on-ring testing, scratch adhesion testing, and piezoRaman and optical fluorescence to measure residual stresses in nonmetallic coatings.

Dr. Hsu presented a possible technical agenda on the proposed new Annex on nanostructured materials outlining the needs for characterizing nanoscale properties and comparing them to the global (macro- or micro-scale) properties. Nanometer scale chemical analysis to identify the nanoparticles or grains was also needed. Dr. Tom Malis presented Canada's research agenda on nanostructured materials and expressed interest in participating in such a new Annex. The focus of the activity would be on the development of uniform standards for testing and measurement of nanomaterials.

Lastly, Dr. Wenyue Zheng gave a presentation on his current work on corrosion protection of magnesium alloys under the lightweight materials. Corrosion of magnesium alloys is of prime concern in transportation applications since road salt in cold climates accelerates corrosion when such alloys are in contact with dissimilar metals (i.e., galvanic corrosion). Dr. Zheng proposed that corrosion protection be a new project under the lightweight materials Annex. Mr. Sullivan suggested that a colleague at the USDOE could be interested in participating in this area.

The Executive Committee voted unanimously to start preliminary planning for the new proposed annexes and assigned Dr. Andy Wereszczak as the interim leader for the Coating Evaluation and Performance Annex; Drs. Stephen Hsu and Tom Malis for the Nanostructured Materials for Transportation Applications Annex; and Dr. Wenyue Zheng for the Corrosion Protection of Magnesium Annex.

Mr. Sullivan then conducted the following actions as requested by the IEA legal office:

Mr. Sullivan put forth a resolution that the following countries to be invited to join the IA-AMT: China, UK, Australia, Japan, and Finland.

The Executive Committee unanimously resolves to invite the Governments of China, UK, Australia, Japan, Finland, or any entity designated by them, to join the Implementing Agreement for a Programme of Research and Development on Advanced Materials for Transportation Applications as a Contracting Party.

The resolution was passed unanimously.

Mr. Sullivan put forth another resolution that delegates from Korea, Austria, Norway, and Israel be invited to the next IA-AMT ExCo Meeting as Observers.

The resolution was passed unanimously.

The following resolutions were offered for vote:

The Executive Committee RESOLVED by unanimity to delete in its entirety Article 9(c) of the Implementing Agreement and to replace it with the following article:

Notwithstanding Article 7 of the IEA Framework for International Energy Technology Co-operation, adopted by the IEA Governing Board on 3 April 2003, the Framework shall apply to, and be an integral part of, this Agreement from 07 May 2006.

The resolution was adopted unanimously.

The Executive Committee FURTHER RESOLVED by unanimity to incorporate all amendments proposed by IEA Legal Office, except for the amendment relating to Article 9(c).

1. Admission and Withdrawal of Contracting Parties

   The Executive Committee RESOLVED by unanimity that Article 10(b) of the Implementing Agreement be deleted and that Articles 10(c)-(i) shall be amended to read as Articles 10(b)-(h) and that the reference in new Article 10(g) to 'paragraph (g) above' be amended to read 'paragraph (f) above'.

   The resolution was passed unanimously.

2. Decisions of the Governing Board

   "The Executive Committee RESOLVED by unanimity to delete in its entirety Article 9(c) of the Implementing Agreement and to replace it with the following article:

   '(c) The IEA Framework for International Energy Technology Co-operation, adopted by the IEA Governing Board on 03 April 2003, shall, together with any amendments thereto, be binding upon all Contracting Parties and Sponsors (as defined in the Framework) which have signed or acceded to, and not withdrawn from, this

Agreement. A copy of the Framework is attached as Exhibit A to this Implementing Agreement and shall be an integral part thereof.' "

The Executive Committee passed the resolution unanimously.

3. Quorum and Unanimity

Article 3(d) (6) provides that the quorum for an ExCo meeting shall be one half of the total number of ExCo members plus one. Article 3(e) in turn provides that, with respect to any decisions required to be taken by the Executive Committee with unanimity, unanimity shall be the vote of all ExCo members "present and voting".

The Executive Committee voted by unanimity to retain these provisions without changes.

Article 3(e) (3) replaces that "decisions to be taken outside a meeting by mail, telex, or cable". The ExCo resolved by unanimity to delete these words and replace them with "mail, fax, email or other electronic transmission".

The Executive Committee voted by unanimity to change the wording.

4. Term of Agreement

"The Executive Committee RESOLVED by unanimity to delete Article 11(a) of the Implementing Agreement in its entirety and replace it with the following article:

'*Term of Agreement*. This Agreement shall remain in force for an initial period of three years and, thereafter, may be extended for such additional periods not greater than five years as may be determined by the Executive Committee, acting by unanimity and subject to the approval of the Committee for Energy Research and Technology of the Agency. The Executive Committee, acting by unanimity, may terminate this Agreement at any time.' "

The resolution passed unanimously.

The next IA-AMT ExCo Meeting was proposed for the week of 6-10 November 2006 tentatively to be held at the National Physical Laboratory in London. The ExCo meeting would be held coincident with a technical workshop on current and proposed annex activities. Invited speakers and current participants are envisioned. Nominations and suggestions for speakers will be solicited by June 30, 2006.

Mechanical Reliability of Thermoelectrics

A. A. Wereszczak, O. M. Jadaan, H. -T. Lin, and K. E. Johanns
Ceramic Science and Technology (CerSAT)
Oak Ridge National Laboratory

Objective/Scope

Potential next generation thermoelectric (TE) devices comprised of p- and n-type oxide ceramics enjoy strong interest for implementation in high temperature and oxidizing environments because their waste heat could be used to generate electricity. However, the intended TE function of these devices will only be enabled if the device is designed to overcome the thermomechanical limitations (i.e., brittleness) inherent to these oxides. Thermoelectric devices become more efficient with larger thermal gradients across them, and this is accomplished by large temperature differences (e.g., greater spatial size) across the TE's hot and cold junctions or the use of low thermal conductivity TE materials or both. A TE oxide with a combination of poor strength and low thermal conductivity can readily fail mechanically in the presence of a thermal gradient thereby preventing the desired thermoelectrical function.

This seemingly insurmountable problem can be overcome through the combined use of established probabilistic design methods developed for brittle structural components, good thermoelastic and thermomechanical databases of the candidate oxide material comprising the TE device, and iteratively applied component design sensitivity analysis. This project executes this process by interrogating prototypical TE devices (e.g., thin-film-based) and oxides.

There will be several outcomes from this work that will benefit TE oxide and device developers and end-users of these potentially high temperature TE devices:

- mechanical reliability of prototypical TE devices will be evaluated from a structural ceramic perspective and suggested redesigns will be identified,
- thermomechanical reliability of developmental TE oxides will be assessed, and
- minimum required thermomechanical properties of hypothetical TE oxides would be identified that produce desired reliability in a TE device.

Additionally, innovative and cost-effective methods to process high temperature capable TEs will be a part of this project's research portfolio.

Technical Highlights

Bismuth telluride TE devices were received from a commercial source and one (Fig. 1) was sectioned, polished, and imaged. A cross-sectional view is shown in Fig. 2. The observed architecture was used to develop a general FEA model during the third quarter that can be used to assess and predict thermoelastic stress states in a TE device.

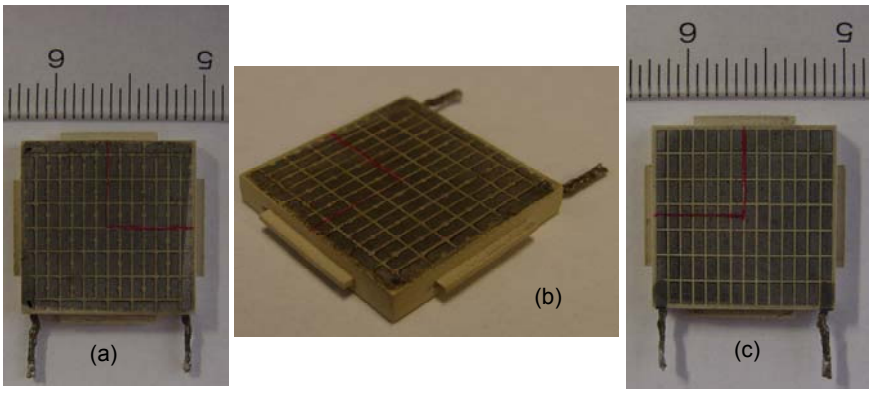

Figure 1. Thermoelectric device modeled in this study. (a) shows what will be referred to as the top surface, while (c) represents the bottom surface. The two drawn red lines represent the planes of symmetry in the FEA model. The location where the two red lines intersect (center of plate) will represent the origin of the axes.

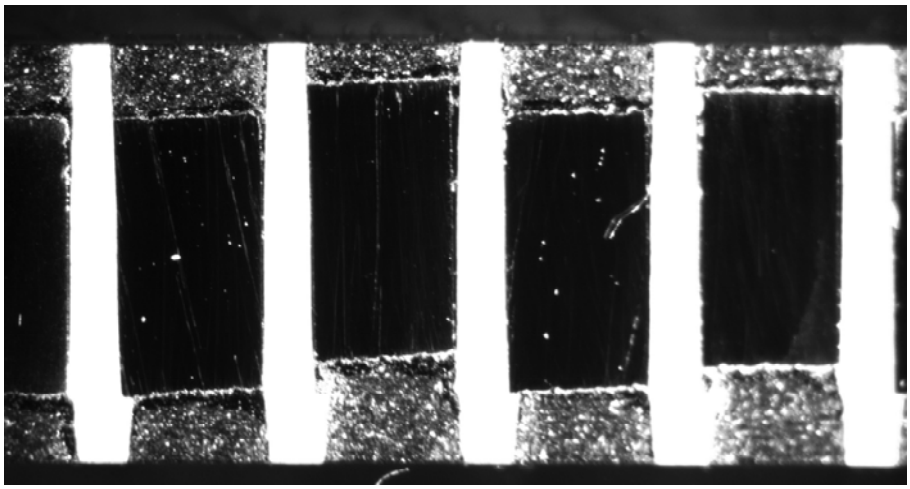

Figure 2. Micrograph of cross section through the thickness of the thermoelectric device.

The constructed ¼-model is shown in Fig. 3. A top temperature of 250°C and a bottom temperature of 100°C were applied to it. The resulting thermal gradient within the device is shown in Fig. 4 with the resulting z-displacement distribution shown in Fig. 5 and First Principal stress profile shown in Fig. 6. As expected, the higher temperature at the top surface causes the device to curl in a concave manner as shown in Fig. 5. Figure 6 shows the maximum tensile stress reaches is located within the ceramic insulator material while the Bi_2Te_3 is under compression.

Now that the model has been created, credible thermoelastic properties of all the constituents will be sought and used in repeated analysis. This work will enable future design sensitivity analysis and probabilistic life design modeling.

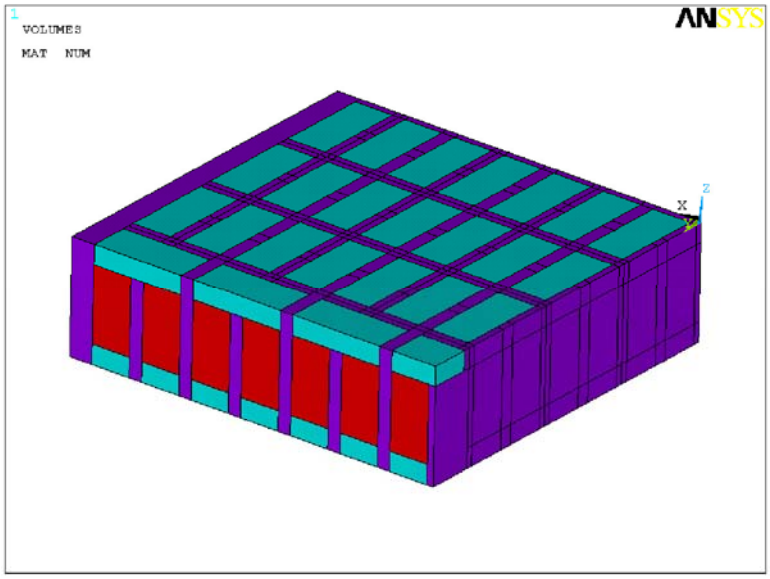

Figure 3. FEA solid 1/4 symmetry model for the thermoelectric device. The Bi_2Te_3 is red here.

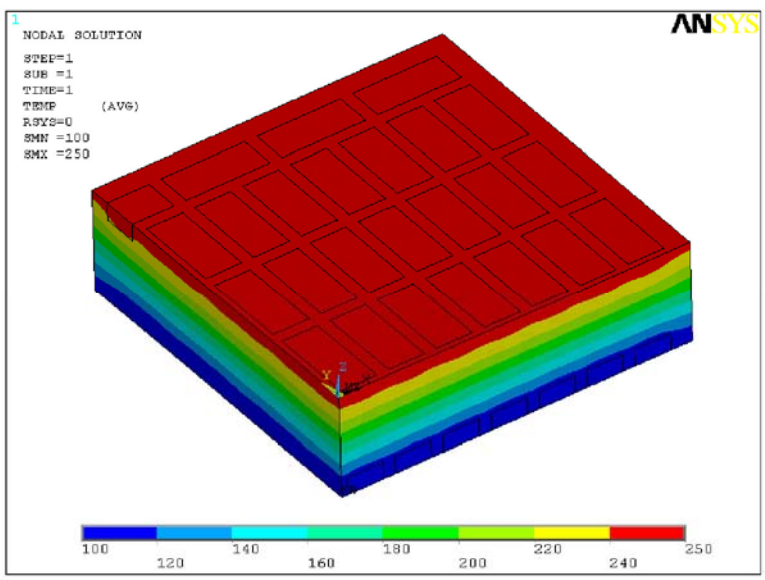

Figure 4. FEA thermal distribution within the device due to temperatures of 250ºC and 100ºC applied to the top and bottom surfaces, respectively.

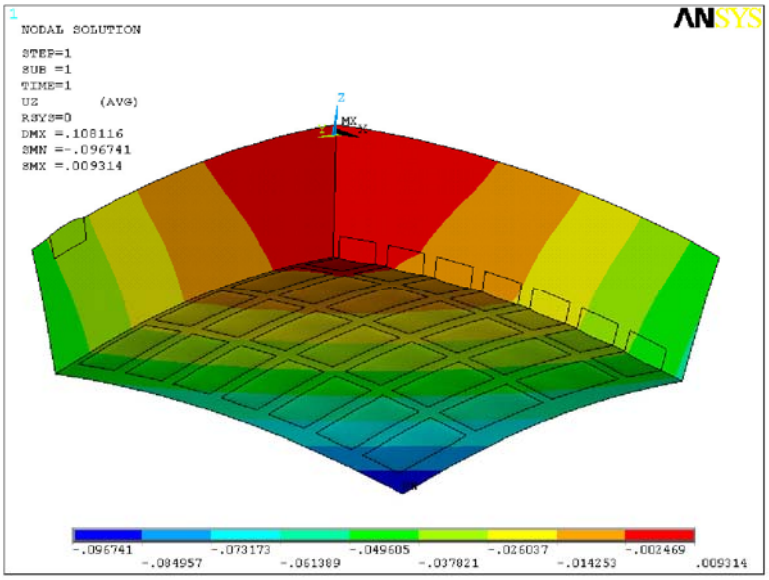

Figure 5. z-displacement distribution (with magnification amplified 50 times).

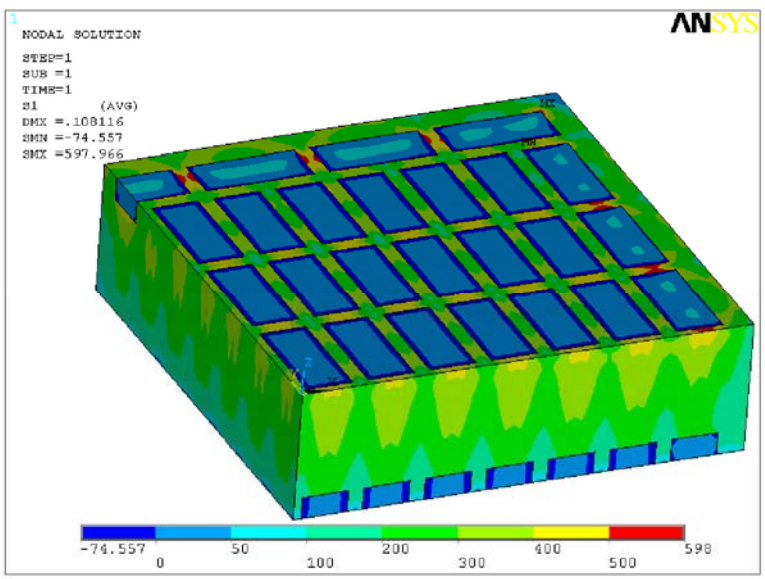

Figure 6. First principal stress distribution (S1) in the thermoelectric device due to the applied thermal loading shown in Figure 4.

Status of FY 2006 Milestones

Develop a general FEA model that can be used to assess and predict thermoelastic stress states in TE devices. **(09/06)** *Completed.*

Communications/Visits/Travel

Discussions were held with Profs. D. Edwards and W. Carty of Alfred University for potential interactions on high temperature oxide thermoelectrics.

Publications

None.

References

None.

Processing and Characterization of Structural and Functional Materials for Heavy Vehicle Applications

J. Sankar, Z. Xu, G. Rajaram and S. Yarmolenko
North Carolina A & T State University

Objective/Scope

To perform the characterization studies on the solid oxide fuel cell (SOFC) anode material.

Task

Fabricate the anode material with different sintering temperatures. The obtained anode material will be used for porosity, permeability and conductivity studies.

Technical Highlights

A solid oxide fuel cell is an energy conversion device that produces electricity by electrochemically combining fuel (from anode) and oxidant (from cathode). The two most common designs of SOFCs are the tubular and the planar [1]. Planar cells are capable of generating high power densities in comparison with the tubular cells. Anode supported planar cells provide very high cycle efficiency and pollution free energy. However, the microstructure of the cell degrades with respect to time due to the high temperature operating conditions. This leads to the deterioration of the fuel cell [2] and subsequent decomposition. This problem causes the major concern towards the commercialization of the fuel cells. The current study was to improve the life and performance of the anode cell for the SOFCs in a long run. In the earlier studies, Muller *et al*. [3] and Lee *et al*. [4] did extensive studies on the porosity and the electrical measurements for anode material with varying proportions of size and mol. % of the raw materials and the sintering temperature. Takehisa *et al.* [5] have used varying sizes of NiO-YSZ composite particles to fabricate a porous anode structure. Clemmer *et al.* [6] have observed dramatic improvements in electrical conductivity with increase in Ni content. Lee *et al.* [7] have investigated the effect of microstructure on anode substrate on the unit cell performance. However, the earlier investigators did not show the relationship between the sintering temperature and the electrical conductivity. So, it was decided to study the effect of sintering temperatures on the porosity and the corresponding effect on the electrical conductivity values.

The anode material was prepared by mixing the different proportions of the raw materials (graphite, NiO and YSZ), compacting uniaxially, sintering in air and finally reducing it in H_2 atmosphere. The graphite powder ratio was 40 vol %, the NiO/YSZ ratio was 57.5/42.5 and the compaction pressure was 150 MPa. Four different sintering temperatures were used (1200, 1250, 1330, 1350°C). The sintered samples were reduced at 1000°C. The powder ratios, compaction pressure, the sintering temperatures and the reduction temperature were decided based on the literature and the previous experience. The different powders used were mixed together using ball milling technique. The die used for powder compaction was half-inch steel die. The permeability tests were carried out to compare the calculated porosity values. The electrical conductivity values were measured using four-probe technique.

Results and Discussion

The different powders (NiO, YSZ and graphite) were weighed based on the volume calculation and mixed together for homogeneity using the horizontal ball milling. The graphite was used to obtain the desired porosity. The ball milled mixture was weighed for individual samples and then poured into the half inch steel die for powder compaction. The green samples were sintered in air for one hour at the maximum temperature. Finally, in order to reduce NiO into Ni, the electrically conductive material in the anode cell, the sintered samples were placed in the reduction furnace under H_2 atmosphere at 1000°C for one hour. The reduced samples were used for the porosity calculations and conductivity measurements. The porosity calculations were based on the weigh and size measurements of the sample followed by the actual and the theoretical volume calculations. The porosity values were determined by permeability method also, to verify the calculated values. The four-point probe method was used for the conductivity measurements. The averaged results are shown in the Table 1.

Table 1. Porosity and the Conductivity results for the different processing conditions

Sintering Temp (°C)	Porosity Vol % (calculated)	Porosity Vol % (permeability test)	Conductivity (Ω^{-1} cm^{-1})
1200	56.5		63.5
1250	55.0	43.37	115.4
1330	41.3		570.2
1350	39.2	27.10	716.6

The porosity calculations indicated that the porosity of the samples sintered at 1350°C was 39.2% which included through pores and voids. However, the permeability test results show that the through pore volume for the sample was around 27 vol %. The results indicate that for solid oxide fuel cell applications, it is necessary to do the permeability measurements to obtain the true porosity volume.

The results show that the sintering temperature was the major variable that controls the porosity and the conductivity of the cell. The conductivity values for the different sintering temperatures shows an interesting result compared with the previous work by Dees *et al*. [8]. The previous work showed that the conductivity of the anode material depends on the Ni volume content percent only and not on the sintering temperature. The current study shows that the conductivity values are dependent on the sintering temperatures, too. For a fixed YSZ/NiO ratio, the conductivity studies (Fig. 1) show that above a critical sintering temperature value, the conductivity value rises significantly. At a lower sintering temperature (1200°C), though the microstructure shows some sintering effect, the structure did not show any grain growth. Due to this, the Ni particles did not have a continuous phase along the structure which resulted in reduced electrical conductivity values. The rise in the conductivity values may be due to the fact that increasing temperature induces the grain growth in the structure and thereby reducing the pore volume of the structure. The grain growth increases the active electrically conducting path along the structure. This improves the conductivity of the sample drastically. At lower sintering temperatures, the inter particle connectivity was poor and that leads to poor electrical charge carrying paths. The values and the plot show that the increase in the conductivity value follows a trend similar to the percolation theory. However, the results indicate that more measurements

should be taken in between the temperature limits (i.e., between 1200 and 1350°C) to confirm that the varying sintering temperature values generate an S-shaped curve. Also, the results will give an in-sight about the percolation threshold, if any.

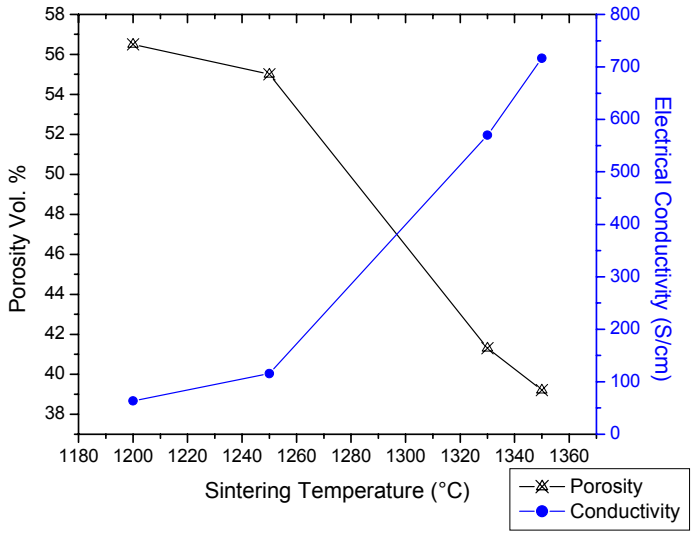

Figure 1. Comparison of porosity values with the electrical conductivity values for different sintering temperatures

Conclusions

In the present study, anode material sintered at different sintering temperatures was used for the electrical conductivity measurement. The results show that the conductivity values increase drastically beyond certain sintering temperature value. Though the results show a kick-off trend for the conductivity values, it is not a perfect S-shaped curve to conclude that the temperature values also is one of the variables that influences the percolation phenomena of the conductive anode material. More experiments with several intermediate temperatures values will be needed to draw further conclusions.

References

1. Singhal, S.C. (2002). Solid oxide fuel cells for stationary, mobile and military applications. Solid State Ionics, 152-153: 405-410.
2. Jorgensen, M.J., Holtappels, P. and Appel, C.C. (2000). Durability test of SOFC cathodes. Journal of Applied Electrochemistry, 30: 411-418.
3. Muller, A.C., Herbstritt, D. and Tiffee, E.I. (2002). Development of a multilayer anode for solid oxide fuel cells. Solid State Ionics. 152-153: 537-542.
4. Lee, J.-H., Moon, H., Lee, H.-W., Kim, J., Kim, J.-D., and Yoon, K.-H (2002). Quantitative analysis of microstructure and its related electrical property of SOFC anode, Ni – YSZ cermet. Solid State Ionics, 148: 15-26.
5. Takehisa Fukui, Murata, K., Ohara, S., Abe, H., Naito, M., and Nogi, K. (2004). Morphology control of Ni-YSZ cermet anode for lower temperature operation of SOFCs. Journal of Power Sources, 125: 17-21.

6. Clemmer, R. M. C, Corbin S. F, (2004). Influence of porous composite microstructure on the processing and properties of solid oxide fuel cell anodes. Solid State Ionics, 166: 251-259
7. Lee, J. H., Heo J. W., Lee, D. S., Kim, J. Kim, G. H., Lee, H. W., Song, H. S., and Moon, J. H. (2003) The impact of anode microstructure on the power generating characteristics of SOFC, Solid State Ionics, 158: 225-232.
8. Dees, D. W., Claar, T. D., Easler, T.E., Fee, D.C., and Mrazek, F.C., (1987) Conductivity of porous Ni/ZrO2-Y2O3 Cermets, Journal of the Electrochemical Society, 134: 2141 - 2145.

Communications/Visitors/Travel

None

Problems Encountered

None

Powder Processing of Nanostructured Alloys Produced by Machining

S. Chandrasekar, K. P. Trumble, and W. D. Compton
Purdue University

Objective/Scope

Work continued on low-temperature consolidation routes for ultrafine-grained alloy particulate produced by machining. This report focuses on the polymer bonding route using Al-6061-T6 machining chip-based particulate.

Technical Highlights

The goal of this approach is to produce bond the machining chip particulate with as fine a polymer bond layer as possible. Previous work has established that premixing the particulate and liquid thermoset and pressing in a steel die is preferred to pressing the powder alone followed by infiltration. Although the metal volume fraction that can be achieved is comparable, a significant fraction of the residual pores in the preform in the infiltration route are closed or otherwise inaccessible to the infiltrant leading to more residual porosity. Although less residual porosity occurs pressing a mixture of the liquid epoxy and alloy particulate, there still is residual porosity, mostly in large epoxy regions larger alloy particles exhibit did not pack well.

In an attempt to overcome the packing limitation, experiments were conducted using the equiaxed particles now being produced by the modulation-assisted machining method. Figure 1 shows the results of pressing the nominal 50-150 μm modulation-assisted machining powder with Buehler Epoxide resin at 800 MPa pressure in a steel die, followed by curing at 100°C for 1 hour. A thin "glue line" of epoxy is present at all the boundaries but the high strength of the particles seems to preclude any significant component of their densification due to particle plasticity. On the other hand, the fraction of epoxy + porosity is similar to composites produced by the same process, but using higher aspect ratio particulate produced by milling machining chips. A potential property advantage of the equiaxed particle composites may be less anisotropy compared to those made with anisometric particles, which has yet to be quantified.

A second study investigated the effect of removing the native surface oxide from the particles before bonding. The same procedure was followed except that the particles were stripped in a 10% NaOH solution for 10 minutes under ultrasonication and then rinsed in distilled water and dried in air. The resulting composite is shown in Fig. 2. Overall, more uniform packing was observed, but the overall packing density (and porosity) levels were comparable to the composites made without pre-cleaning the particles in this way. An intriguing observation is that the interparticle bond ("glue line") appears to be thicker with the pre-cleaned particles.

The overall constituent volume fractions in these composites are about 87% alloy, 9% epoxy, and 4% porosity. Work is continuing to eliminate the residual porosity and evaluate tensile properties.

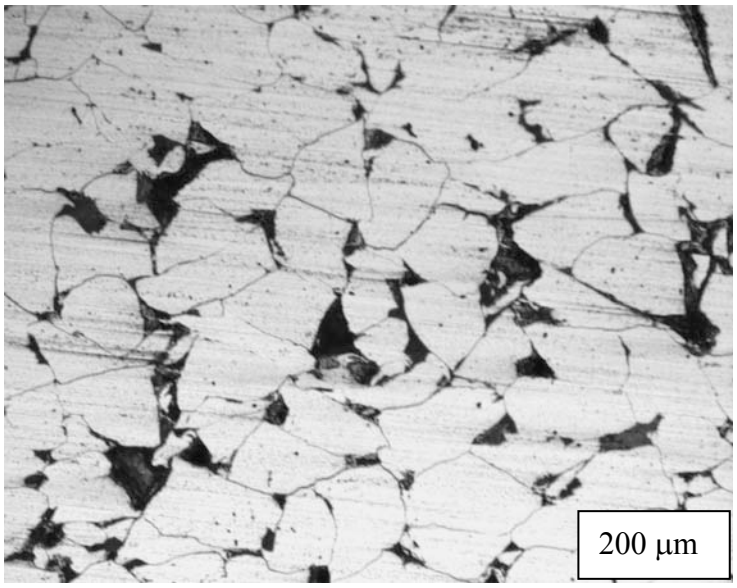

Fig. 1 - Equiaxed Al-6061-T6 powder/Epoxy composite produced at 800 MPa pressing pressure showing little or no local deformation of the (strong) particles leading to incomplete packing of the particles.

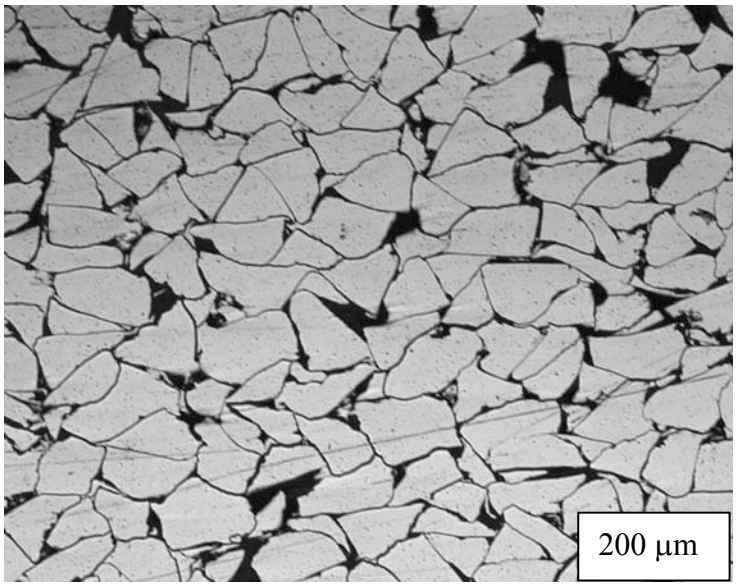

Fig. 2 - Composite made in identical process to that shown in Fig. 1 but with particles pre-cleaned in caustic solution to remove surface oxide. More uniform packing and apparently thicker interparticle bond layers, but the overall composite density was not significantly different.

Problems Encountered

None

Status of Milestones

"Evaluate a range of consolidation and densification routes that enable bulk monolithic and composite materials to be produced from nanostructured machining chip particulate without significant coarsening." On schedule.

Publications

1) P. Iglesis, M. D. Bermudez, F. J. Carrion, S. Chandrasekar, and W.D. Compton, A study of the wear behavior of polymer-matrix composite containing discontinuous nanocrystalline alloy reinforcements, *Tribology International*, in press.

2) M. Ravi Shankar, S. Chandrasekar, W.D. Compton and A.H. King, Characteristics of Aluminum 6061-T6 Deformed to Large Strains by Machining, *Materials Science and Engineering A*, **410-411**, 364-368, 2005.

Next Generation Ceramics for Heavy Vehicle Propulsion Applications

Paul F. Becher
Oak Ridge National Laboratory

Objective/Scope

In addition to lower specific weight, ceramics have a number of attractive properties for application as components in various heavy vehicle systems such as electrochemical properties needed to develop advanced sensors and wear resistance and low coefficients of friction to increase life in moving components. Significant new opportunities are beginning to evolve with the advent of nanocrystalline materials. Initial findings show that nanocrystalline ceramics have substantially improved electrochemical properties, which are being explored in sensors for combustion and emissions controls, and auxiliary power sources. Studies have also revealed that ceramics with grain sizes <100 nanometers can exhibit very high hardness, which may translate to greater wear resistance either in the form of coatings or components (e.g., for valve train components) or to create low friction surfaces to enhance engine performance.

The goal being to develop the technology to form "green" (unfired) bodies of nanocrystalline particles to allow one to devise pressureless sintering profiles to produce dense monolithic bodies with grain sizes <100 nm. This is aimed at finding approaches to produce sizeable monolithic bodies for subsequent evaluation. The second thrust focuses on the mechanical and wear behavior of nanocrystalline ceramics and the influence of external parameters (e.g., stressing rate, temperature, environment (e.g., air, vacuum), and electric fields (in collaboration with researchers at North Carolina State University) on the plastic deformation behavior.

Technical Highlight

Tensile tests are now underway on dense 400 nm grain size zirconia ceramics to complement earlier compression test results to assess if electric fields effects on deformation are a function of the sign of the applied stress (i.e., greater in tension than in compression). These studies seek to understand how superplastic behavior might be promoted at lower temperatures.

Status of Milestones

Characterize mechanical and wear behavior of nanocrystalline ceramics was delayed with the decision to not continue funding the processing studies at the Pennsylvania State University. Instead, nanocrystalline ceramics fabricated by MetaMateria were received and their fracture behavior examined. MetaMateria produces various nanocrystalline materials (powders, porous and dense bodies) including oxide ceramics and thermoelectric materials.

Communications/Visits/Travel

None

Publications

None